# EVALUATION OF PLASTIC HINGE MODELS AND INELASTIC ANALYSIS TOOLS FOR PERFORMANCE-BASED SEISMIC DESIGN OF RC BRIDGE COLUMNS

By

Lauren Kimberly Fedak

### A THESIS

Submitted to
Michigan State University
In partial fulfillment of the requirements
For the degree of

MASTER OF SCIENCE

Civil Engineering

2012

#### **ABSTRACT**

# EVALUATION OF PLASTIC HINGE MODELS AND INELASTIC ANALYSIS TOOLS FOR PERFORMANCE-BASED SEISMIC DESIGN OF RC BRIDGE COLUMNS

By

#### Lauren Kimberly Fedak

For over 50 years, the notion of an equivalent region under constant plastic curvature, i.e., the plastic hinge length (Lp), has been the main approach for evaluating the inelastic response of reinforced concrete (RC) columns for seismic bridge design. Most of the proposed Lp models have been calibrated on columns with modest slenderness to predict ultimate displacement. However, modern design approaches require predicting intermediate damage levels, or limit states, and urban congestion is leading to increasingly slender columns; thus bringing doubt on the reliability of plastic hinge models. The performance of Lp models in lumped plasticity elements was assessed by conducting analyses on 34 columns from the PEER Column Database. Results show that the Lp definition in lumped plasticity analyses produces drastic and random differences for varying limit states. Distributed plasticity elements can capture inelastic global and local response throughout the element without explicit definition of an inelastic zone. Lumped and distributed plasticity elements were thus assessed by comparing the global and local responses for five columns of increasing slenderness; the most slender of which was constructed and tested as part of this research to expand the current database for slender columns. Performance was found to be sensitive to aspect ratio; indicating behavior controlled by P-delta effects. The study has highlighted the need for a unified definition of limit states, as well as improved methods to accurately and efficiently predict inelastic behavior at each limit state. Inaccuracy in current numerical tools was found not only at intermediate limit states but also when predicting the global behavior of slender columns.

#### ACKNOWLEDGMENTS

First and foremost, I offer my sincerest gratitude to my advisor, Dr. Rigoberto Burgueño, whose guidance and encouragement has made my graduate career truly rewarding. His passion and continuous push for excellence has helped me grow not only as an engineer but as an individual. My success in completing my research and writing this thesis would not have been possible without him.

I also thank Dr. Venkatesh Kodur and Dr. Parviz Soroushian for serving on my thesis defense committee and offering their insight and guidance.

I would like to express my appreciation to Mr. Siavosh Ravanbakhsh for his great help and patience in completing my work at the Civil Infrastructure Laboratory. His knowledge and support, along with that of Mr. Chuck Meddaugh was invaluable in completing my work at the lab. My gratitude also goes to the students who graciously offered their time and assistance during construction and testing: Ata Babazadeh, David Stringer, Caroline Williams and Yi Sun.

I also acknowledge the support from Michigan State University, the Civil and Environmental Engineering Department, and the National Science Foundation.

Finally, I offer my deepest thanks to my parents, family and friends who always believe in me even more than I do myself. Their support and encouragement has been the foundation on which I am able to overcome all obstacles.

# TABLE OF CONTENTS

List of Tables		vi
List of Figures		vii
List of Symbols		xi
CHAPTER 1		
1 Introduction	1	1
1.1 Motiva	tion	1
1.2 Researce	ch Objectives and Hypotheses	7
1.3 Thesis	Organization	8
CHAPTER 2		
2 Literature R	Review	11
2.1 Perform	nance-Based Seismic Design	11
2.2 Spread	of Plasticity in Reinforced Concrete Bridge Columns	14
2.2.1 Fac	ctors Affecting the Spread of Plasticity	17
2.3 The Pla	astic Hinge Concept	20
2.3.1 Pla	astic Hinge Length Design Models	22
2.3.2 Par	rameters Affecting Lp	29
	ical Analysis Methods	
	mped Plasticity Models	
2.4.2 Dis	stributed Plasticity Models	35
2.5 P-Delta	a Effects	37
CHAPTER 3		
3 Methods		39
3.1 Analys	is Methods	39
3.1.1 Op	penSees	39
3.1.1.1	Lumped Plasticity Element	40
3.1.1.2		
3.1.1.3	Material Models	
_	mental Methods	
	st Unit Design Parameters	
	aterial Properties	
	strumentation	
3.2.3.1	Strain Measurement	
3.2.3.2	Curvature Calculation	
3.2.3.3	Shear Measurement	
3.2.3.4	Lateral Displacement Measurement	
324 Io	ading	61

3.2.5	Test Setup	67
3.2.6	Observations	69
3.2.6	5.1 Cracking	69
3.2.6	5.2 Spalling and Overall Damage	72
CHAPTER -	4	
4 Evaluat	ion of Plastic Hinge Design Models	75
4.1 The	e PEER Structural Performance Database	75
4.2 Sel	ected Columns	76
4.3 Op	enSees Model	
4.3.1	Analytical Target Displacements	
	alysis Results	
4.4.1	Limit State Analysis	
4.4.1		
4.4.1	$\mathcal{E}$	
4.4.1	$\epsilon$	
4.4.1	$\mathcal{E}$	
4.4.1	1	
4.4.1	1	
4.4.2	Conclusions of Plastic Hinge Design Models	98
CHAPTER :	5	
5 Evaluat	ion of Numerical Analysis Methods and Slenderness Effects	101
	ected Columns	
5.2 Spe	ecific Modeling Approaches	103
5.3 Glo	obal Response	104
5.3.1	Second Order Effects	111
5.3.1	.1 Effect of Column Test Setup	111
5.3.1	.2 P-Delta Effects	115
	cal Response	
5.4.1	Curvature	
5.4.2	Lateral Displacement	
	read of Plasticity	
	formance of Predicted Limit States	
	levant Conclusions	
5.7.1	Effect of Element Type	
5.7.2	Effect of Aspect Ratio	149
CHAPTER		
6 Conclus	sions and Recommendations	151
References		

# LIST OF TABLES

Table 1-1: General Example of Performance-Based Design	2
Table 2-1: Example of PBD Definitions in Reinforced Concrete Bridge Columns	12
Table 2-2: Symbol Definitions for Implementation of Hines et al. Plastic Hinge Model	28
Table 3-1: Assumed Reinforcing Steel Material Properties in OpenSees Modeling	43
Table 3-2: Assumed Unconfined Concrete Material Properties in OpenSees Modeling	47
Table 3-3: Definition of Terms for Confined Concrete Material Model	50
Table 3-4: Material Properties Day of Testing	55
Table 3-5: Target Load and Displacement Levels	67
Table 4-1: PEER SPD Columns Used for Limit State Analysis (PEER 2011)	79
Table 4-2: Plastic Hinge Expressions Used in OpenSees Analysis	81
Table 4-3: Limit State Results from Experimental Data (PEER 2011)	84
Table 4-4: Mean Percent Limit State Error and COV per Plastic Hinge Model	. 100
Table 5-1: Column Properties for Evaluation of Numerical Analysis and Slenderness	. 103
Table 5-2: Cyclic Load Levels of Analyzed Columns	. 104
Table 5-3: Comparison of Predicted Ultimate Displacement (in.)	. 137
Table 5-4: Mean Percent Limit State Error for Case Study Columns	. 140
Table 5-5: Error in Limit State Prediction for Cyclic Analyses	. 147
Table 5-6: Total Mean Error per Element Type and Aspect Ratio	. 148

# LIST OF FIGURES

Figure 1-1: Freeway Damage after Northridge, CA Earthquake, 1994 (Caltech 2011)
Figure 1-2: Distribution of Column Aspect Ratio in PEER Database
Figure 1-3: Column Flexibility
Figure 1-4: Meanings of the Plastic Hinge Length, L <sub>p</sub>
Figure 2-1: Example of Concrete Damage States (Lehman and Moehle 2000)
Figure 2-2: Example of Reinforcing Steel Damage States (Lehman and Moehle 2000)
Figure 2-3: Schematic of Simplified Bridge Column and Bending Forces
Figure 2-4: Moment-Curvature Response and Distribution of Curvatures
Figure 2-5: Schematic of Tension Shift Phenomenon
Figure 2-6: Effect of Tension Shift on Bending Moment and Curvature
Figure 2-7: Schematic of Strain Penetration Phenomenon
Figure 2-8: Schematic of the Plastic Hinge Concept
Figure 2-9: Displacement Profile and Plastic Rotation Based on Plastic Hinge Concept 22
Figure 2-10: Discretized Fiber Section
Figure 2-11: Schematic of Defining Inelasticity in a Lumped Plasticity Element
Figure 2-12: Integration Methods for Lumped Plasticity Elements
Figure 2-13: Assumed Curvature Distribution in Lumped Plasticity Models
Figure 2-14: Schematic of Element in a Distributed Plasticity Approach
Figure 2-15: P-Delta Effects on Bridge Columns (Adapted from Priestley et al. 1996, Abell 2012)
Figure 3-1: Elements used in OpenSees Analyses
Figure 3-2: Reinforcing Steel Model
Figure 3-3: Bar Slenderness Parameters for Gomes and Appleton Cyclic Steel Model

Figure 3-4: Buckling Parameters as Defined by the Gomes and Appleton Model for Cycli Behavior (Adapted from Gomes and Appleton 1997)	
Figure 3-5: Typical Reinforced Concrete Section for Circular Columns	46
Figure 3-6: Zero-Strength Concrete Material Model	47
Figure 3-7: Confined versus Unconfined Concrete (Adapted from Priestley et al. 1996)	50
Figure 3-8: Portion of Column in Elevation Defining Transverse Reinforcement Terms	51
Figure 3-9: Concrete Material Envelope and Variable Definitions (Adapted from Op 2011)	
Figure 3-10: Test Column 123007 Geometry and Reinforcement	54
Figure 3-11: Instrumentation Setup	56
Figure 3-12: Curvature Instrumentation	58
Figure 3-13: Schematic of Displacement due to Curvature	59
Figure 3-14: Shear Instrumentation	60
Figure 3-15: Shear Panel Configuration	61
Figure 3-16: Schematic of Displacement Due to Shear	62
Figure 3-17: Horizontal Measurement	63
Figure 3-18: Loading Setup	66
Figure 3-19: Target Force/Displacement History	66
Figure 3-20: Test Setup	68
Figure 3-21: Test Setup Components	69
Figure 3-22: Column Cracking Pattern at $\mu_{\Delta}$ =3	71
Figure 3-23: Column at 20-inch Displacement ( $\mu_{\Delta}$ =3)	73
Figure 3-24: Damage due to Spalling at end of $\mu_{\Delta}$ =3 (20-inch Displacement)	74
Figure 4-1: Example of Unstable Hysteresis, Resulting in Elimination from PEER A Program (PEER 2011)	
Figure 4-2: Typical Discretized Fiber Column Section	82

Figure 4-3: Experimental vs. Predicted Drift at Cover Spalling for Various L <sub>p</sub> Models	88
Figure 4-4: Experimental vs. Predicted Drift at Core Crushing for Various L <sub>p</sub> Models	90
Figure 4-5: Experimental vs. Predicted Drift at Bar Buckling for Various L <sub>p</sub> Models	93
Figure 4-6: Experimental vs. Predicted Drift at Bar Fracture for Various L <sub>p</sub> Models	95
Figure 4-7: Experimental vs. Predicted Drift at Ultimate Conditions for Various $L_p$ Models	98
Figure 5-1: Distribution of Column Aspect Ratio in Analyzed Columns from the SPD	. 102
Figure 5-2: 415 Experimental vs. Analytical Hysteretic Response	. 106
Figure 5-3: SRPH1 Experimental vs. Analytical Hysteretic Response	. 107
Figure 5-4: 815 Experimental vs. Analytical Hysteretic Response	. 108
Figure 5-5: 1015 Experimental vs. Analytical Hysteretic Response	. 109
Figure 5-6: 123007 Experimental vs. Analytical Hysteretic Response	. 110
Figure 5-7: Axial Load Correction Cases for Experimental Columns (Berry et al. 2004)	. 112
Figure 5-8: 415 Corrected Force Data	. 113
Figure 5-9: SRPH1 Corrected Force Data	. 113
Figure 5-10: 815 Corrected Force Data	. 114
Figure 5-11: 1015 Corrected Force Data	. 114
Figure 5-12: 123007 Corrected Force Data	. 115
Figure 5-13: 415 Corrected Hysteresis vs. P-Delta Analysis	. 116
Figure 5-14: SRPH1 Corrected Hysteresis vs. P-Delta Analysis	. 117
Figure 5-15: 815 Corrected Hysteresis vs. P-Delta Analysis	. 117
Figure 5-16: 1015 Corrected Hysteresis vs. P-Delta Analysis	. 118
Figure 5-17: 123007 Corrected Hysteresis vs. P-Delta Analysis	. 118
Figure 5-18: Distributed Plasticity Integration Schemes	. 119
Figure 5-19: 123007 Distributed Plasticity Integration Schemes with P-Delta	. 120

Figure 5-20: 415 Curvature Profiles (Dashed=Exp.; Solid=Dist. Plas.)	123
Figure 5-21: SRPH1 Curvature Profiles (Dashed=Exp.; Solid=Dist. Plas.)	123
Figure 5-22: 815 Curvature Profiles (Dashed=Exp.; Solid=Dist. Plas.)	124
Figure 5-23: 1015 Curvature Profiles (Dashed=Exp.; Solid=Dist. Plas.)	124
Figure 5-24: 123007 Curvature Profiles (Dashed=Exp.; Solid=Dist. Plas.)	125
Figure 5-25: 415 Displacement Profiles (Dashed=Exp.; Solid=Dist. Plas.)	127
Figure 5-26: SRPH1 Displacement Profiles (Dashed=Exp.; Solid=Dist. Plas.)	127
Figure 5-27: 815 Displacement Profiles (Dashed=Exp.; Solid=Dist. Plas.)	128
Figure 5-28: 1015 Displacement Profiles (Dashed=Exp.; Solid=Dist. Plas.)	128
Figure 5-29: 123007 Displacement Profiles (Dashed=Exp.; Solid=Dist. Plas.)	129
Figure 5-30: 415 Spread of Plastic Hinge Region, L <sub>pr</sub>	131
Figure 5-31: SRPH1 Spread of Plastic Hinge Region, L <sub>pr</sub>	132
Figure 5-32: 815 Spread of Plastic Hinge Region, L <sub>pr</sub>	133
Figure 5-33: 1015 Spread of Plastic Hinge Region, L <sub>pr</sub>	134
Figure 5-34: 123007 Spread of Plastic Hinge Region, L <sub>pr</sub>	135
Figure 5-35: Comparison of Constant vs. Variable L <sub>p</sub> Models (Column 815)	137
Figure 5-36: Limit State Prediction with Lumped Plasticity Monotonic Analyses	139
Figure 5-37: 415 Hysteretic Limit State Comparisons	142
Figure 5-38: SRPH1 Hysteretic Limit State Comparisons	143
Figure 5-39: 815 Hysteretic Limit State Comparisons	144
Figure 5-40: 1015 Hysteretic Limit State Comparisons	145
Figure 5-41: 123007 Hysteretic Limit State Comparisons	146

## LIST OF SYMBOLS

bar cross-sectional area  $A_b$ gross cross-sectional area  $A_g$ spiral cross-sectional area  $A_{s}$ ;  $A_{sp}$  $\boldsymbol{D}$ column diameter outer spiral diameter D'bar diameter  $d_b$  $\boldsymbol{E}$ elastic modulus effective stiffness EI<sub>eff</sub> ideal yield force  $F_{v}$ theoretical yield force  $F'_y$ specified (28 day) concrete compressive strength  $f_c$ compressive strength of confined concrete f'cctensile strength  $f_t$ ultimate steel stress  $f_u$ steel yield strength  $f_{\mathbf{y}}$ 

spiral yield strength

 $f_{ys}$ 

I moment of inertia L length gauge length  $L_g$ plastic hinge length  $L_p$ plastic hinge region length  $L_{pr}$ strain penetration length  $L_{sp}$ ideal yield moment  $M_{v}$ theoretical yield moment  $M'_y$ ultimate moment  $M_u$ P axial load spacing S shear/lateral force  $\boldsymbol{V}$ 1 displacement

 $\Delta_u$  ultimate displacement

 $\Delta_p$ 

plastic displacement

 $\Delta_y$  ideal yield displacement

 $\mathbf{\Delta'_y}$  theoretical yield displacement

 $\epsilon_c$  concrete strain

 $\mathcal{E}'_{cc}$  confined concrete strain

$\varepsilon_{cu}$	ultimate concrete strain	
$\mathcal{E}_{S}$	steel strain	
$\varepsilon_{sh}$	steel strain at hardening	
$\varepsilon_{su}$	ultimate steel strain	
$arepsilon_t$	tensile strain	
$\boldsymbol{\varphi}$	curvature	
$arphi_p$	plastic curvature	
$\varphi_u$	ultimate curvature	
$arphi_y$	ideal yield curvature	
$\varphi'_y$	theoretical yield curvature	
$\mu_{\Delta}$	displacement ductility	
$\mu_{oldsymbol{arphi}}$	curvature ductility	
$\mathcal{O}_p$	plastic rotation	
$ ho_{e\!f\!f}$	effective confinement ratio	
$ ho_l$	longitudinal reinforcement ratio	
$ ho_{\scriptscriptstyle S}$	spiral reinforcement ratio	

#### 1 INTRODUCTION

#### 1.1 Motivation

Seismic design, until recent years, has followed the conventional force-based approach. This method predicts a maximum credible earthquake and designs for life safety. However, damage to a structure designed with this method often shows signs of more extensive damage than expected (Ghobarah 2001). The reason for this is that smaller intensity earthquakes that occur at larger frequency impose damage to the structure that may not be apparent. There may be small cracks in the concrete or yielded reinforcing steel that are not seen, but accumulate large strains over time, causing catastrophic damage once a large intensity earthquake occurs. An example of structural failure is shown in Figure 1-1 following the 1994 earthquake in Northridge, California. Higher than expected damage in reinforced concrete structures, like those shown has given rise to the need for new design methods.

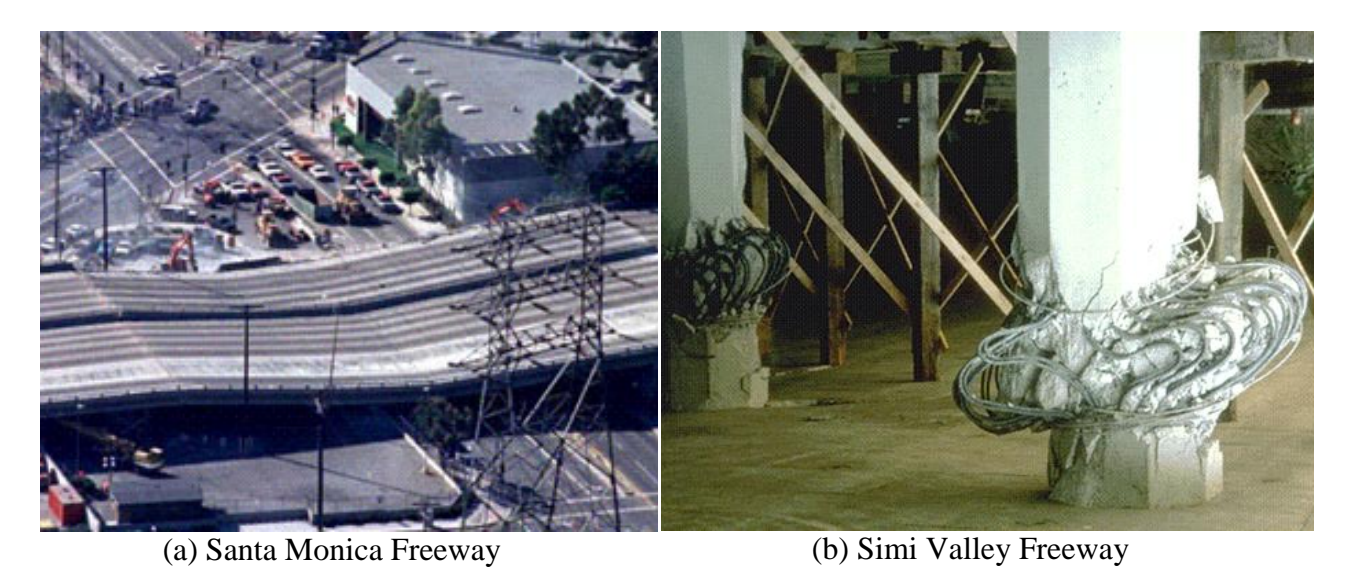


Figure 1-1: Freeway Damage after Northridge, CA Earthquake, 1994 (Caltech 2011)

(For the interpretation of the references to color in this and all other figures, the reader is referred to the electronic version of this thesis.)

Seismic design has therefore been moving towards a performance-based methodology. Performance-based design (PBD) is a method in which design criteria are expressed in terms of achieving a set of performance objectives when the structure is subjected to stated levels of seismic hazard (Ghobarah 2001). Implementation of this method requires defining limit states at which the structure experiences an important damage level. A limit state may be a load, displacement, stress, strain level, etc. not to be exceeded by the associated risk demand. Ghobarah gives a very basic example of this method, shown in Table 1-1 (Ghobarah 2001). Here, a damage state is defined by a specific drift limit. For each limit, there is an expected level of performance that the structure or a component of the structure should uphold. PBD takes multiple intermediate damage states (those prior to collapse) into account and explicitly defines repair methods for each. Limit states, however are currently ill-defined, and attempts to define limit states in seismic structures has posed much difficulty among researchers and designers alike.

**Table 1-1: General Example of Performance-Based Design** 

Damage State	Performance Level	Limit State
None	Fully operational, immediate occupancy	drift < 0.2%
Repairable	Repairable Operational, damage control, moderate	
Irreparable	Life safe, near collapse	drift < 1.5%
Severe	Hazard reduced	drift < 2.5%
Replacement	Collapse	drift > 2.5%

In order to design to the noted limit states, it is necessary to develop methods that can predict the onset of important damage levels. Several models exist for predicting structural seismic behavior; however most models are calibrated to estimate global behavior such as a maximum force or ultimate displacement. In order to implement PBD it is necessary to be able to predict local behavior as well, such as strain or curvature at intermediate lengths along a member.

Various methods are used to predict local behavior; however a single method or set of methods has not been proven to give accurate results for a wide range of design parameters. Even simple reinforced concrete structures, such as cantilever bridge columns show drastically different results for varying analysis methods.

While PBD may be implemented to any type of structure under extreme conditions, this research focuses specifically on reinforced concrete bridge columns that are typical in the majority of highway bridge columns in seismic zones. These types of structures commonly show higher than expected damage after high intensity earthquakes. The reason for this is the sheer simplicity of bridge structures. The simple column and deck layout of a bridge makes it a seemingly uncomplicated structure, yet its lack of redundancy, in contrast to building structures, make it an easy target for seismic damage (Priestley et al. 1996). Structures subjected to large seismic demands are expected to yield and plastify. Critical regions in a structure are therefore deliberately chosen and detailed to exhibit ductile behavior. Bridge code typically dictates that all inelastic action occurs in the bridge columns where damage is easily inspected and repaired while the bridge superstructure is to remain elastic (Caltrans 2010). This study therefore focuses on the column substructure, where damage levels need be predicted.

Factors that are well known to affect the behavior of reinforced concrete structures include reinforcement ratio, axial load ratio and aspect ratio. Aspect ratio is of particular interest since the effect of slenderness has not been extensively researched. This is shown in Figure 1-2, which gives the distribution of slenderness ratio (length/depth) for 416 columns documented in the PEER Structural Performance Database (PEER 2011). As construction in large cities continues

to grow, however, highway bridges tend to be built upward, resulting in very high aspect ratio columns (L/D>8) whose performance under large seismic demands is unknown. Although uncommon to design columns with aspect ratios of 10 and 12, such as those studied in this thesis, additional flexibility in a bridge system may cause a column to behave as such. For example, columns are commonly assumed to be in perfect double bending when rigidly connected to the superstructure, causing the point of contra-flexure to be at the center of the column height (see Figure 1-3a). However the bridge superstructure may not be fully fixed to the top of the column, due to rotational flexibility of the superstructure. Additionally, seismic action in the ground often causes additional rotation at the foundation. Both of these instances of flexibility are not typically accounted for and increase the effective length of the column, as shown in Figure 1-3. It is therefore necessary to evaluate current analysis models for predicting behavior needed for PBD implementation as well as to evaluate how design factors, such as aspect ratio, will affect how these models perform. By evaluating this data it may be possible to indicate which, if any, models are effective for PBD.

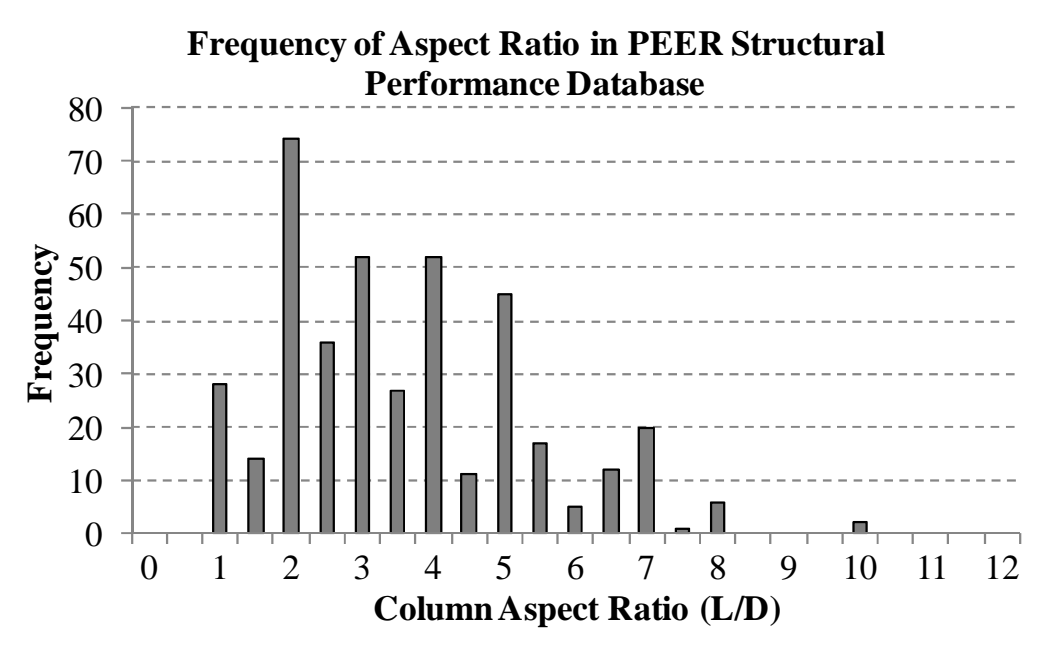


Figure 1-2: Distribution of Column Aspect Ratio in PEER Database

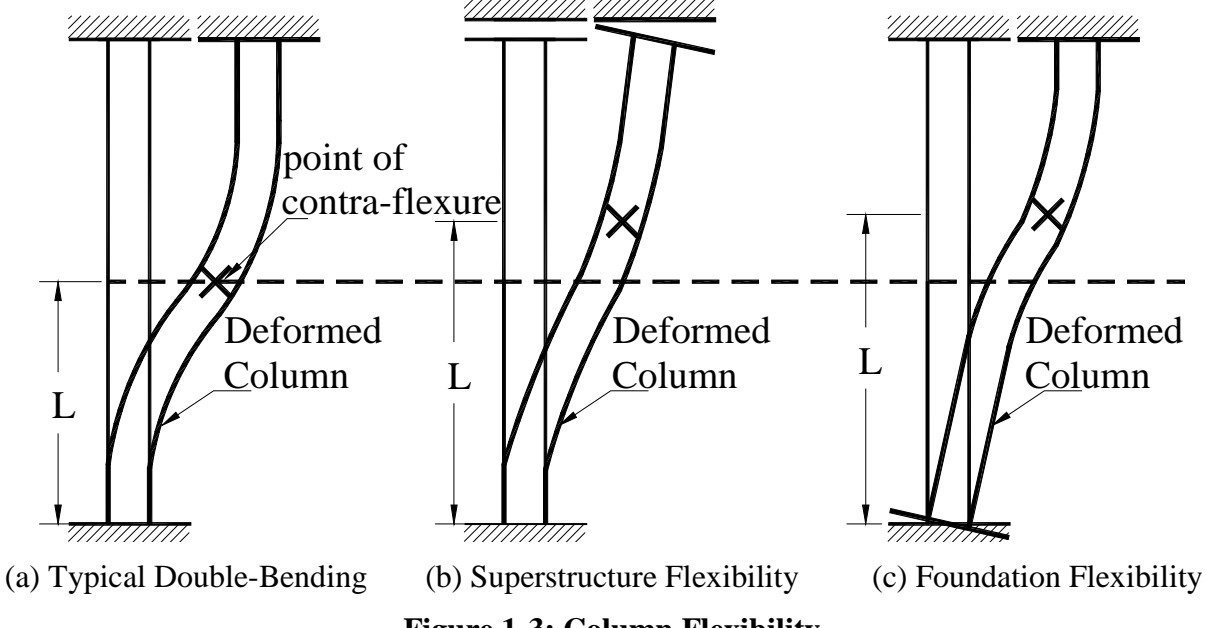


Figure 1-3: Column Flexibility

The most common numerical methods for predicting inelastic behavior in seismic structures, and those of interest in this thesis, are lumped plasticity and distributed plasticity models. The lumped plasticity concept is commonly used due to its simplicity, and has been adopted for current design practices (Caltrans 2010). The distributed plasticity formulation is of interest for its ability to capture inelastic behavior along the element length.

The lumped plasticity model, which is discussed frequently within this thesis, assumes that all inelastic action at concentrated in a single point or region, termed the plastic hinge length. The plastic hinge length, L<sub>p</sub>, is a design parameter to simplify the physical behavior in a reinforced concrete member. Its exact meaning however varies among researchers, as does its formulation, which is discussed extensively in Chapter 2. In a *physical* sense refers the length over which inelastic action extends is called the plastic hinge region, L<sub>pr</sub>. In a *design* sense, L<sub>p</sub> is a parameter used to simplify the plastic region into an equivalent constant region over which the

plastic curvatures are assumed constant. This parameter is typically used in analysis and design methods to easily estimate plastic rotations (Priestley et al. 1996, Caltrans 2010). In a *numerical modeling or analysis* sense, the plastic hinge length is used by lumped plasticity elements to efficiently compute inelastic actions by the finite element method, however depending on the integration scheme chosen, its application may not be synonymous to what the design parameter was formulated for. The definition of plastic hinge may therefore be described in three distinct categories: physical, design and modeling, as depicted in Figure 1-4.

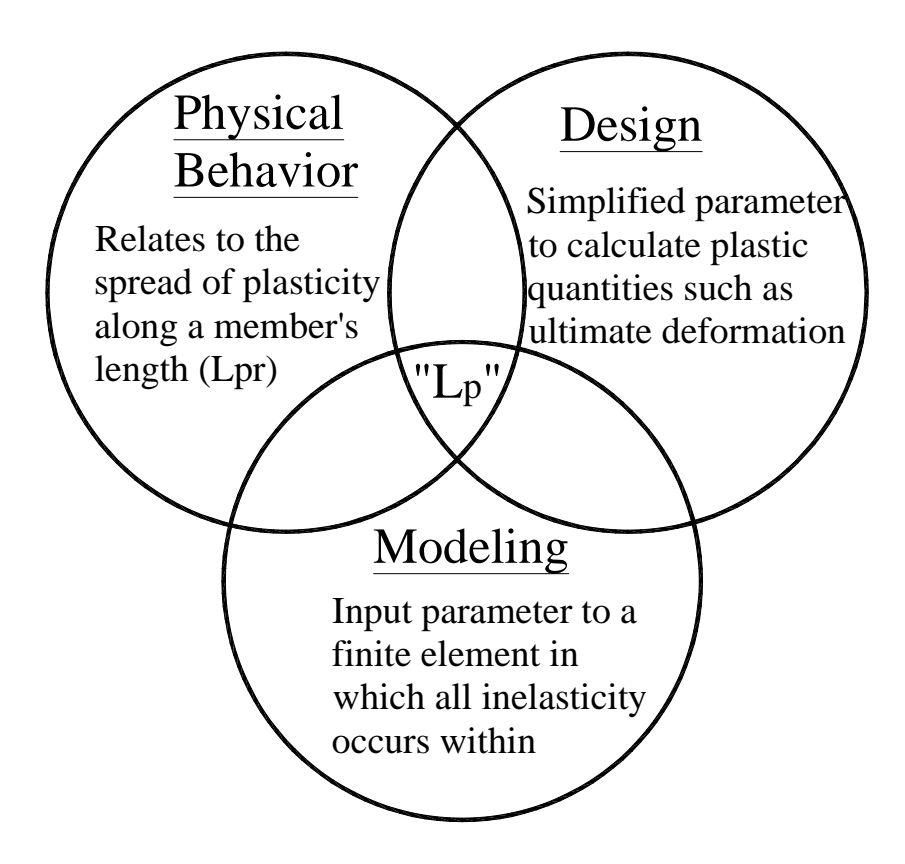


Figure 1-4: Meanings of the Plastic Hinge Length, Lp

The appropriateness of using different plastic hinge models as well as other numerical techniques for predicting intermediate limit states for use in PBD is the main motivation behind this research.

#### 1.2 Research Objectives and Hypotheses

The objective of this research is to evaluate current analysis methods for predicting local and global limit states in the interest of performance-based seismic design. Two common analysis tools are evaluated: lumped plasticity elements and distributed plasticity elements. Lumped plasticity elements are popular in practice due to their simplicity for hand calculations as well as computational efficiency in the finite element method. These elements are defined by their plastic hinge length, for which several models are proposed. Distributed plasticity elements are also of interest due their ability for extracting data at intermediate integration points. When evaluating these methods, aspect ratio is to be also considered to determine how it affects the spread of plasticity in reinforced concrete columns and the prediction of specified limit states. Evaluation of analysis tools and effecting factors was completed both analytically and experimentally.

Several hypotheses were formulated to guide the research approach of this thesis. Each hypothesis and the methods in which it was tested are described as follows:

- I. Current plastic hinge length design models are unable to predict limit states with enough accuracy and consistency to be implemented into performance-based design. This was tested through the analysis of thirty-four documented experimental reinforced concrete columns using lumped plasticity fiber-based finite elements with varying plastic hinge definitions. The error was found for each plastic hinge model's estimation of several important damage states.
- II. Modern nonlinear beam-column finite element models may not be appropriate for estimating limit states important to performance-based seismic design. A select number

of columns are analyzed for monotonic and cyclic loading with lumped plasticity elements and distributed plasticity elements. Global and local parameters were extracted from both approaches and compared to experimental data.

III. Error in global and local parameters increases with slenderness in reinforced concrete columns. This was tested by analyzing five columns of varying aspect ratio (L/D = 4, 6, 8, 10 and 12) and comparing the analytical results to experimental data. It is believed that as aspect ratio increases, error in limit state prediction increases as well. In order to complete the data set and to fully understand the spread of plasticity in very slender columns, an aspect ratio 12 column was constructed and tested under reverse cyclic loading as part of this research.

#### 1.3 Thesis Organization

The next chapter provides a review of literature pertaining to the methods and analytical tools used in this thesis. The underlying motivation behind the research, performance-based design, is described in detail first, followed by the definition of the several analysis tools used for limit state prediction, including the lumped plasticity and distributed plasticity approaches. A description of the lumped plasticity approach as well as the plastic hinge concept is given, as well as several proposed models that researchers have developed for the plastic hinge length. The distributed plasticity approach is also described along with an overview of different integration schemes and how they affect an analysis with using distributed plasticity finite elements.

The methods used to evaluate current analysis techniques for predicting limit state behavior are described after the literature review. Chapter 3 describes the methods used to complete the following evaluations of numerical methods. Included is the finite element platform and specific

modeling techniques used throughout the thesis. Also included in Chapter 3 are the experimental methods used to test a column of aspect ratio 12 which was used for numerical analyses in subsequent chapters. Details of the column design, construction and representative results are included as part of this chapter.

The first main research task consisted of evaluating several plastic hinge length models for use in predicting limit states. A statistical assessment was completed to determine the effectiveness with which common plastic hinge models predict the top displacement of experimental cantilever columns at several damage states. The full details of the analyzed columns and the results of the analysis are given in Chapter 4.

In order to evaluate numerical techniques such as the lumped plasticity approach compared to distributed plasticity elements, five experimental columns were analyzed using both monotonic and cyclic loading in Chapter 5. Several limit states are again predicted using each modeling technique and compared to experimental data. Data that was evaluated included both global response measures, such as the force-displacement hysteresis, and local responses, such as curvature profiles with increasing displacement ductility. The columns studied in this portion of the research were chosen as to cover a wide range of aspect ratios. Therefore, the results from their analyses may be used to study both the effect of slenderness on column behavior and the effectiveness of numerical techniques for predicting this behavior. Conclusions based on the numerical results are given at the end of Chapter 5 and are summarized in relevance to the thesis as a whole in Chapter 6.

The concluding chapter of this thesis describes the major results found in the precluding studies and conclusions drawn from these results. Conclusions are outlined in terms of the initial research hypotheses to determine their acceptance or rejection. Recommendations for future research as well practice within the scope of performance-based design are given as well.

#### 2 LITERATURE REVIEW

This chapter reviews current literature pertaining to the overall concepts behind this research as well as the numerical techniques used to evaluate the hypotheses made in the previous chapter. The purpose of the information within this review is to first describe the physical phenomena that affect the cumulative damage and eventual failure of reinforced concrete bridge columns, then to describe the design parameters used to simplify these phenomena into quantifiable limits. Finally, the numerical techniques used for predicting inelastic behavior are described. Exact formulations of these techniques are not given, but rather the underlying assumptions that accompany the techniques and their specific abilities are described.

#### 2.1 Performance-Based Seismic Design

Conventional seismic design methods follow a force-based approach where the objective is to provide for life safety under a maximum credible earthquake. Most codes therefore do not explicitly require consideration of performance other than life safety (Lehman et al. 2004). Although structures perform well from a life safety perspective, the level of damage, economic loss due to loss of use, and repair costs are very high (Ghobarah 2001). Thus, researchers have identified a need for change in current seismic codes. Performance-based design (PBD) has stemmed from studying the post-earthquake damage of highway bridges, which in many cases has been unexpectedly high. By determining the onset of important levels of damage prior to complete failure, repairs may be made to structures after small intensity seismic events to regain structural strength and avoid high economic loss or safety compromises in the future. Performance-based seismic design is therefore a developing method in which design criteria are expressed in terms of achieving a set of performance objectives, in terms of structural response

or damage, when a structure is subjected to stated levels of seismic hazard, then defining a repair method for each (Ghobarah 2001).

Implementation of PBD requires defining limit states at which the structure experiences an important damage level. Critical levels of damage for reinforced concrete elements have been identified by researchers to include the onset of nonlinear response in concrete as well as the reinforcing steel. Specifically, damage states for RC structures include concrete spalling, concrete crushing, reinforcement buckling and reinforcement fracture, all of which are discussed at length in Chapter 4 of this thesis. These damage states are listed in the Structural Performance Database created by the Pacific Earthquake Engineering Research Center (PEER 2011) as well as studied by other researchers in the context of PBD (Lehman et al. 2004, Berry et al. 2008). Implementing PBD requires defining a limit state for each damage level. For example, Table 2-1 shows limit states in terms of concrete strain ( $\varepsilon_c$ ) and steel strain ( $\varepsilon_s$ ) for each of the damage levels mentioned. Visualization of these damage states in experimental columns may be seen in Figure 2-1 and Figure 2-2. However, before PBD can be implemented into modern codes it is necessary to develop response models to simulate the nonlinear structural behavior and numerically predict the onset of important damage states according to well-accepted definitions.

Table 2-1: Example of PBD Definitions in Reinforced Concrete Bridge Columns

Damage State	Performance Level	Limit State
Concrete Spalling	Fully operational	$\epsilon_{\rm c} \ge 0.003$
Concrete Crushing	Operational, damage control	$\epsilon_{c} \ge$ Maximum Compressive Strain (as determined by selected concrete model)
Reinforcement Buckling Life safe		$\epsilon_s \ge$ Maximum Buckling Strain (as determined by selected steel model)
Reinforcement Fracture	Hazard reduced	$\epsilon_{\rm S} \ge 0.1$

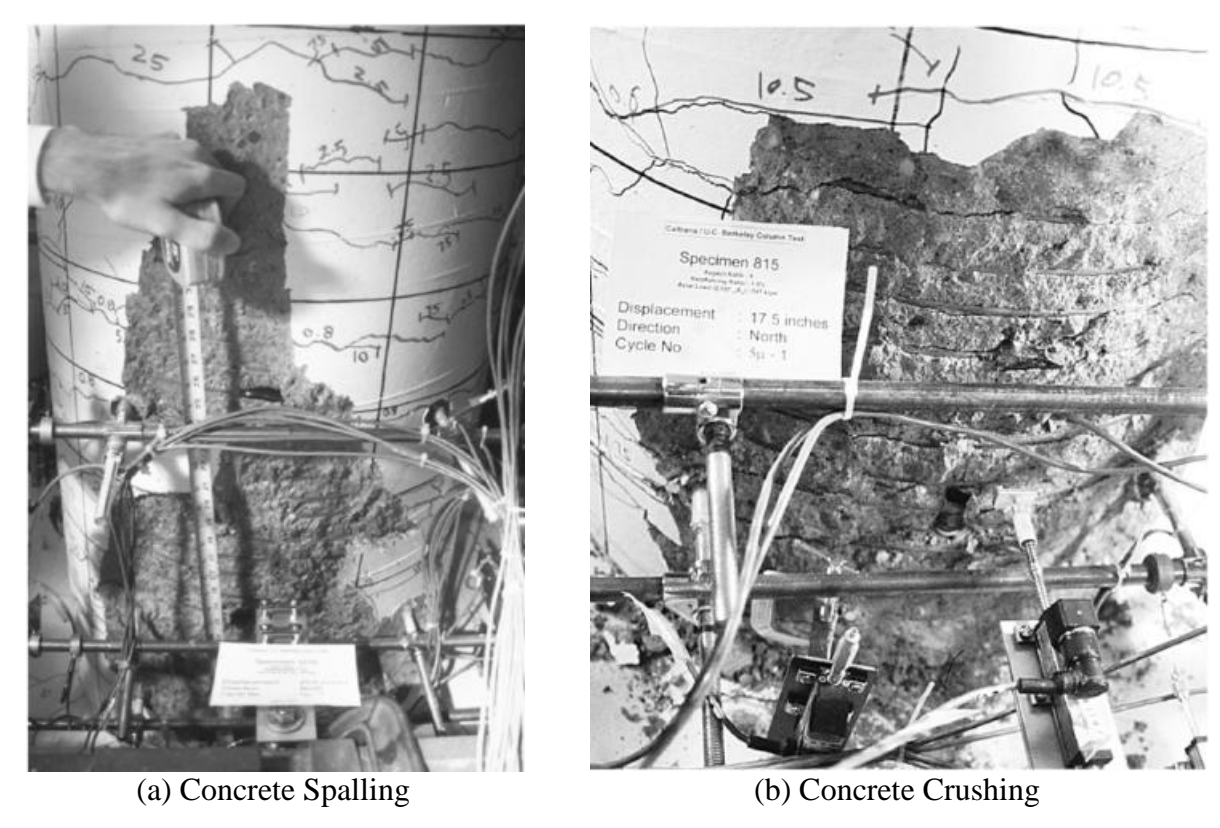


Figure 2-1: Example of Concrete Damage States (Lehman and Moehle 2000)

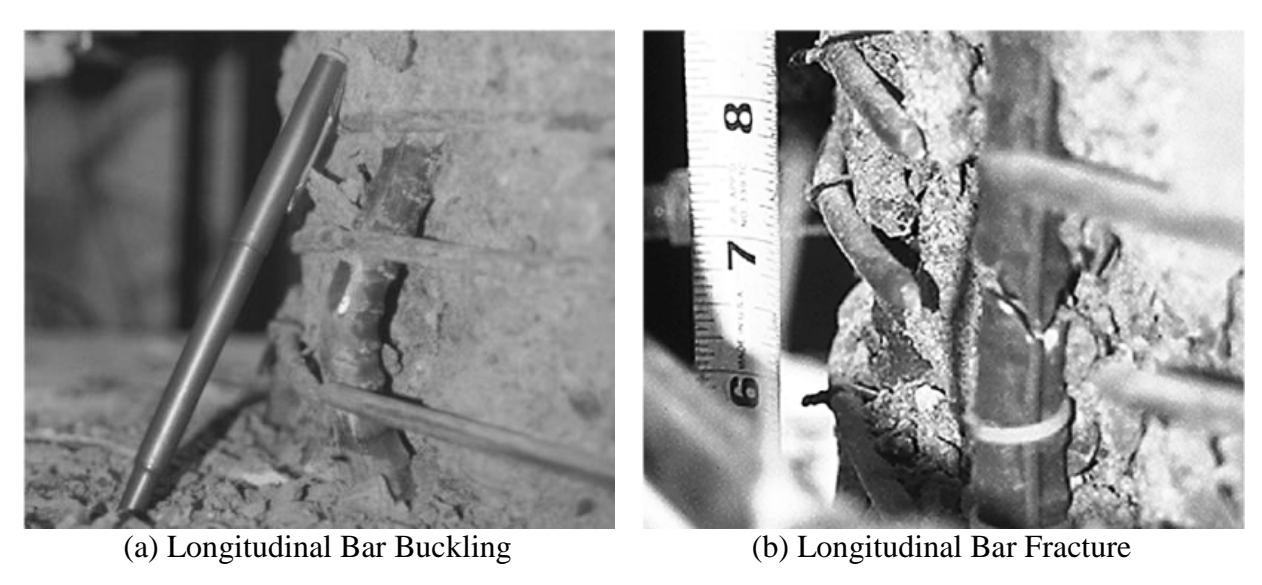


Figure 2-2: Example of Reinforcing Steel Damage States (Lehman and Moehle 2000)

#### 2.2 Spread of Plasticity in Reinforced Concrete Bridge Columns

Modern seismic design is centered around capacity design principles, where structural behavior is to be controlled by design through the predetermined development of acceptable collapse mechanisms with predefined inelastic zones that are to respond primarily in flexure in order to maximize energy dissipation under hysteretic response. Thus, damage in reinforced concrete columns is to occur predominately due to flexural response, with most cracking developing on the tension side of the column. Tension forces are mainly carried by the reinforcing steel; however concrete carries a portion of the tension due to bond stresses between steel and concrete. The moment gradient along the column will lead to shear stresses and lead to diagonal cracking. The combination of flexure and shear demands leads to larger tensile forces across inclined shear cracks spreading inelasticity to a larger extent than in a member subjected to pure flexure. Due to the cyclic nature of seismic loading, each side of a column switches between tensile and compressive flexure-induced demands and cracks in the concrete will continue to open and close along the column length. After the reinforcing steel yields in tension (at a given location), it is permanently elongated and closing of the tensile crack in the concrete upon load reversal requires restoring (by compressing it) the elongated bar back to its original length. Depending on the extent of yielding on tension prior to reloading on compression and on the lateral restraint available, reinforcement bars may buckle. Upon continued cycling, a buckled bar will have to be straightened (when loaded in tension) and then buckle again upon load reversal. Continued damage of this type may lead to permanent opening of cracks and eventual fracture of the steel reinforcement due to low cycle fatigue. The lateral deformation of buckled longitudinal bars also places large loads on the transverse reinforcement, which may kink and/or fracture

(Park and Paulay 1975). The behavior just described explains why a column becomes weaker from successive cyclic loading and how inelastic behavior spreads over the length of the column.

When estimating the inelastic response of bridge columns they are typically considered as fixedend cantilever members with an axial load to represent the bridge superstructure. This simplification is due to the representation of the column by its effective shear span, as shown in Figure 2-3a, where the free-end in the simplified model represents the point of contra-flexure in the actual column. The inelastic region of a cantilever column when subjected to horizontal loading is located near the confined base, where the largest bending moment demands occur, and it is detailed for ductile response according to capacity design principles (Priestley et al. 1996). This is shown in Figure 2-3b,c where L is the effective shear span of the column. Since the response of a well-design column is mainly due to flexure, the behavior of the column may be extrapolated from its section behavior at the base represented by a moment-curvature response, as shown in Figure 2-4a. For design purposes, the actual response is typically idealized with a bilinear (elasto-plastic) representation by defining the ideal yield curvature ( $\phi_v$ ), theoretical yield moment  $(M'_{y})$ , ideal moment  $(M_{y})$ , and ultimate curvature  $(\phi_{u})$ . The theoretical yield moment is defined as the first instance of material yielding, however is not typically used in design since it is very sensitive to material types, axial load and other design parameters. The ideal moment is therefore used for design purposes and is assumed to be the moment when concrete strains reach 0.004 or steel strains reach 0.015, whichever occurs first. The region between yield and ultimate conditions is the plastic curvature  $(\phi_p)$ , and the effective stiffness of the section is defined by the slope of the idealized bilinear response:

$$(EI)_{eff} = \frac{M_{y}}{\varphi_{y}}$$
 2-1

Under large lateral loads, the materials in the region near the column base typically yield and the structure experiences large inelastic curvatures (Park and Paulay 1975). Due to the cyclic nature of seismic loads, there is an accumulation of strains and a loss of strength in the column. Therefore, upon repeated cycles the curvatures progressively grow along the column height (refer to Figure 2-4b), consequently increasing the region along which steel reinforcement yields as well. This growth of the inelastic region is known as the spread of plasticity, and the extent along the column length to which plasticity grows is known as the plastic hinge region,  $L_{pr}$ .

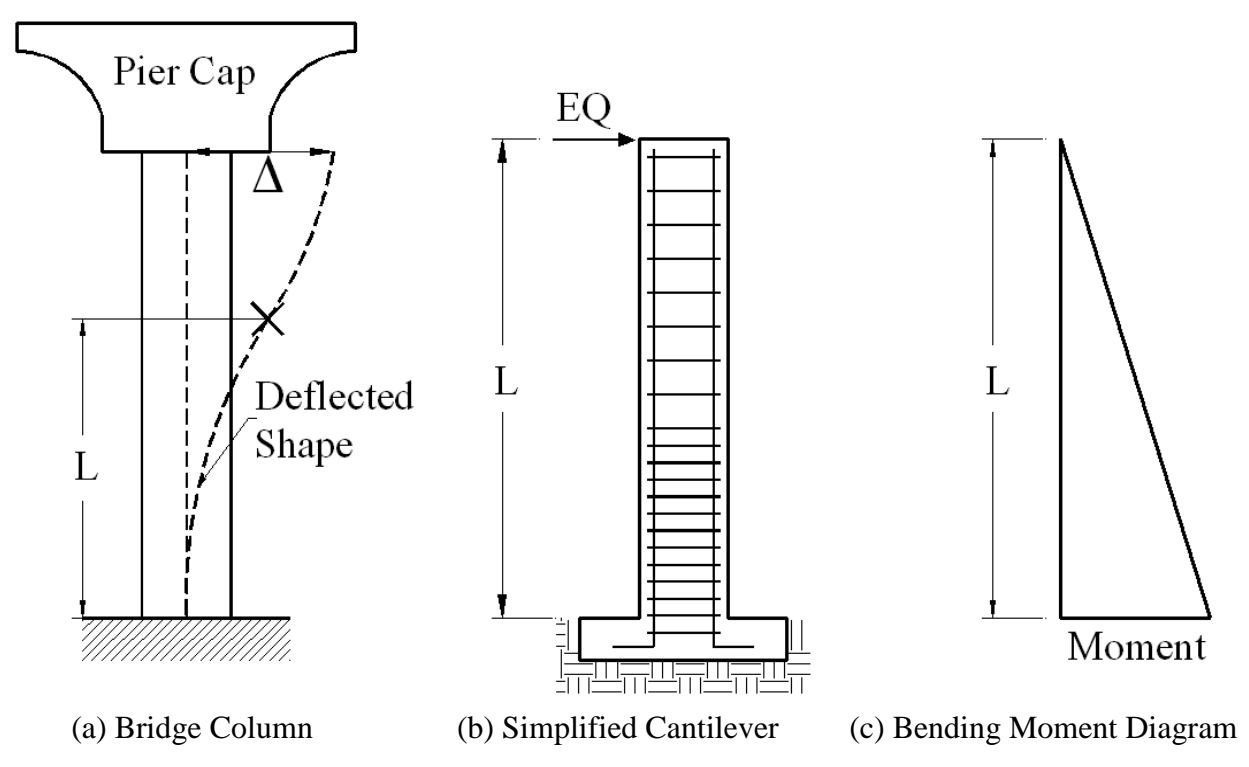


Figure 2-3: Schematic of Simplified Bridge Column and Bending Forces

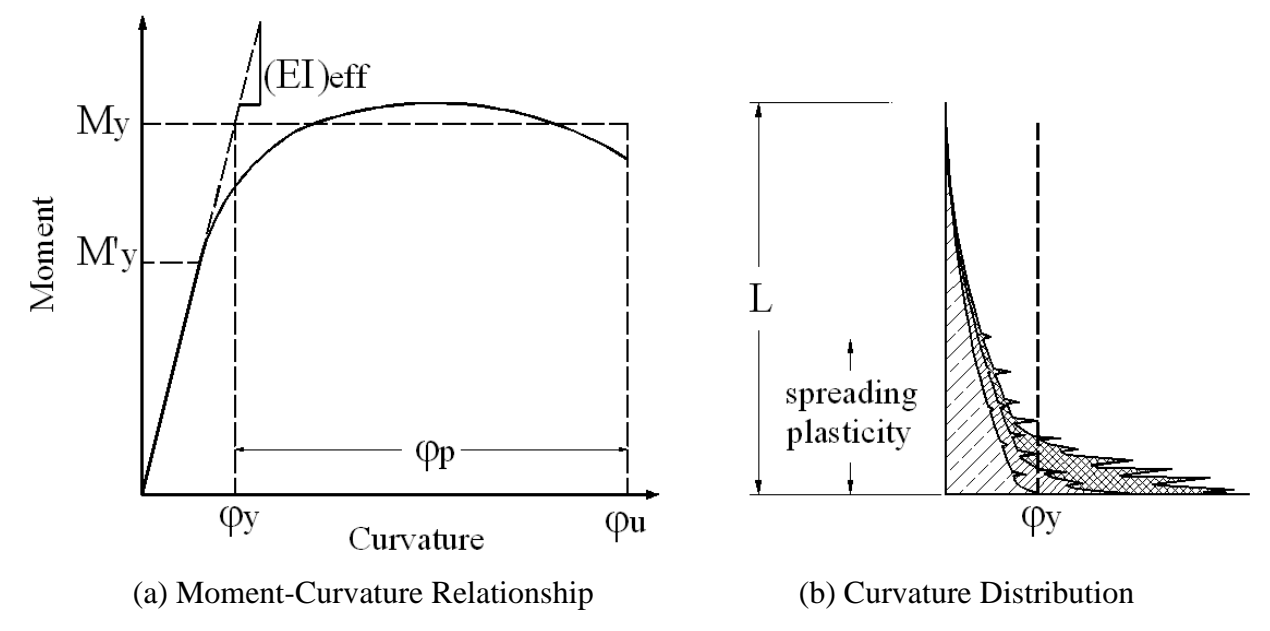


Figure 2-4: Moment-Curvature Response and Distribution of Curvatures

#### 2.2.1 Factors Affecting the Spread of Plasticity

It is well agreed upon among researchers that the spread of plasticity in reinforced concrete members is caused by three major phenomena: moment gradient, strain penetration and tension shift (Hines et al. 2004). The moment gradient effect relates the plastic moment of a column to the length of its shear span. A column with a longer span therefore will have a larger spread of plasticity along its length. Assuming plane sections remain plane under inelastic behavior, the moment gradient can be accounted for by simply assessing the moment-curvature relationship of a section and assuming inelastic action to occur over a fraction of the column's length.

The assumption that plane sections remain plane however is false. Diagonal cracks that form due to shear cause the tension in steel to occur over a more extensive region than assumed by a plane sections theory. As shown in Figure 2-5, in a plane section the tensile forces would be equal to the compression forces, C, at plane 1; however, due to shear stresses (v) in the diagonal crack the

tension force (T) in the reinforcing bar actually occurs at plane 2, which accumulates over the distance between the two planes. This second phenomenon is known as tension shift, and is dependent on the inclination of the diagonal cracks (Park and Paulay 1975). The spread of plasticity in a column is therefore greater than assumed by the moment gradient effect alone, as shown in Figure 2-6.

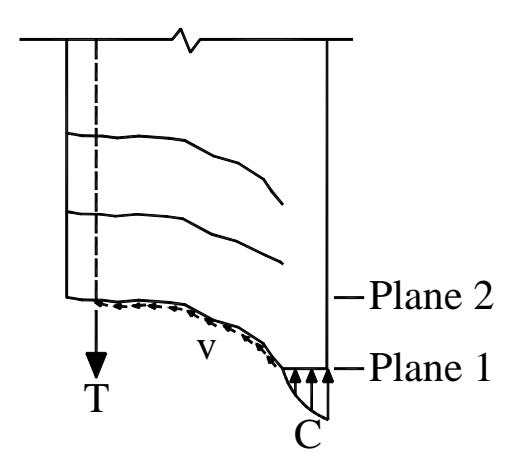


Figure 2-5: Schematic of Tension Shift Phenomenon

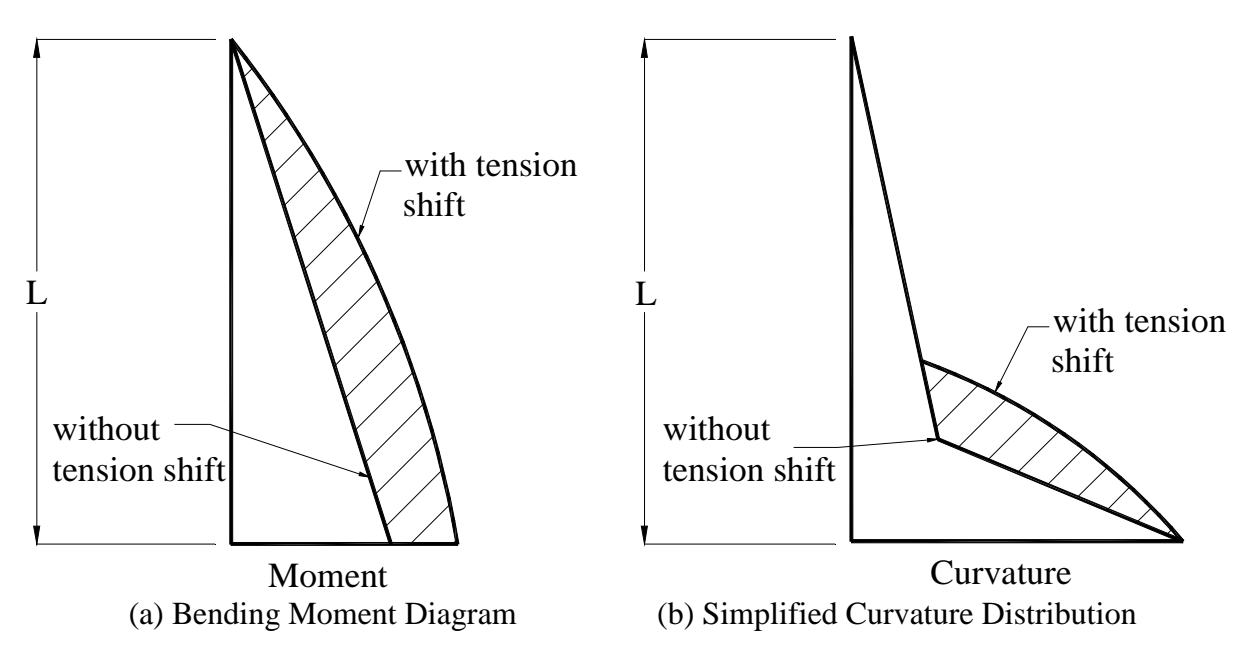


Figure 2-6: Effect of Tension Shift on Bending Moment and Curvature

The third phenomenon affecting the spread of plasticity in reinforced concrete columns is the strain penetration (also known as bond slip) of reinforcement into the column's footing. The longitudinal reinforcing bars are anchored a distance into the footing. Given that large inelastic demands occur at the base of the column, a portion of the inelastic strains penetrate the anchorage length of the reinforcement and transfer some of this strain to the surrounding concrete. Typically, cracks will generate in the footing near the column's base due to this behavior, causing the reinforcement to slip and increased plastic rotations to occur at the column's base as shown in Figure 2-7. The strain penetration phenomenon has been found to contribute to about 35% of the lateral deformations in experimental columns (Zhao and Sritharan 2007).

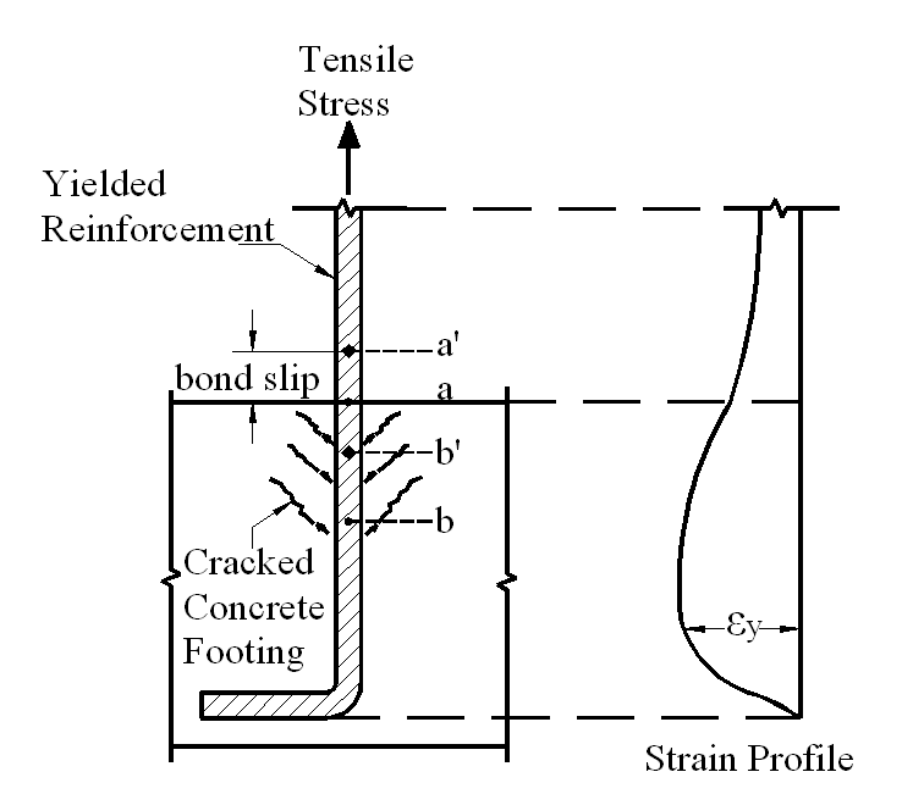


Figure 2-7: Schematic of Strain Penetration Phenomenon

#### 2.3 The Plastic Hinge Concept

In an attempt to efficiently analyze the inelastic response of reinforced concrete elements without addressing in detail the complex nature of a column's spreading plasticity, researchers have simplified the plastic hinge region by representing it with a constant length, termed the plastic hinge length,  $L_p$  (Park and Paulay 1975, Priestley et al. 1996). This representation simplifies the actual curvature distribution into two segments: elastic and plastic portions, as shown in Figure 2-8. The height of the plastic portion is  $L_p$ , which is a combination of the plastic curvatures above the column base ( $L_p$ ') and those penetrating the column footing, termed the strain penetration length,  $L_{sp}$ . This concept is widely used because it makes determination of displacements very simple. Like curvature, ultimate displacement at the top of a cantilever column may be defined by the sum of its elastic and plastic components;

$$\Delta_u = \Delta_y + \Delta_p$$
 2-2

where  $\Delta_y$  is the yield displacement and  $\Delta_p$  is the plastic displacement, as shown in Figure 2-9a. The yield and plastic displacements are a function of the sectional response quantities and the plastic hinge components as seen in Equations 2-3 and 2-4:

$$\Delta_{y} = \frac{\varphi_{y}(L + L_{Sp})^{2}}{3}$$
 2-3

$$\Delta_p = (\varphi_u - \varphi_y) L_p H$$
 2-4

where 
$$H = L - \frac{Lp}{2}$$
 2-5

A more refined approach to estimating displacements is possible by taking strain hardening into account rather than assuming a bilinear response (see Figure 2-4a). In this case, the following equations are used (Priestley et al. 2007):

$$\Delta' y = \frac{\varphi' y \left(L + L_{Sp}\right)^2}{3}$$
 2-6

$$\Delta_p = \Delta' y \frac{M}{M_y} + \left(\varphi_u - \varphi' y \frac{M}{M_y}\right) L_p H$$
 2-7

In both cases shown, all plastic deformation is assumed to occur within the plastic hinge, with rotations occurring at a single point in the middle of the plastic hinge length, as shown in Figure 2-9b. It is also acceptable to assume rotations occur at the base, rather than the middle of the plastic hinge; in this case H in Equation 2-5 would be equal to the length of the column, L (Priestley et al. 2007). Therefore, based on this concept, a column's inelastic response can be estimated from simple hand calculations using its plastic hinge length.

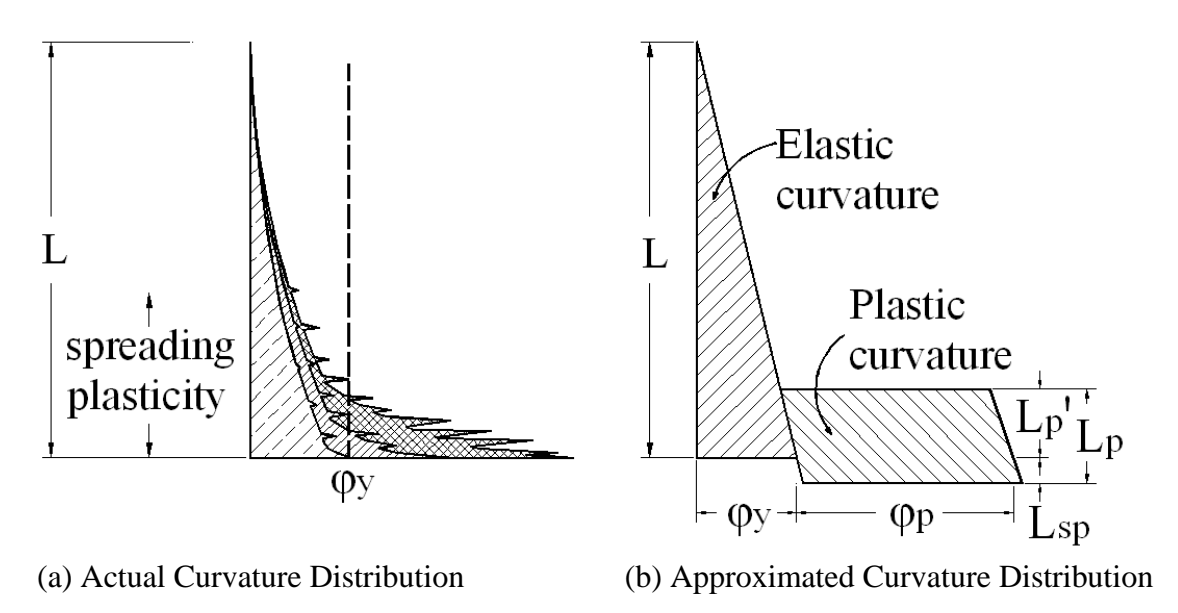


Figure 2-8: Schematic of the Plastic Hinge Concept

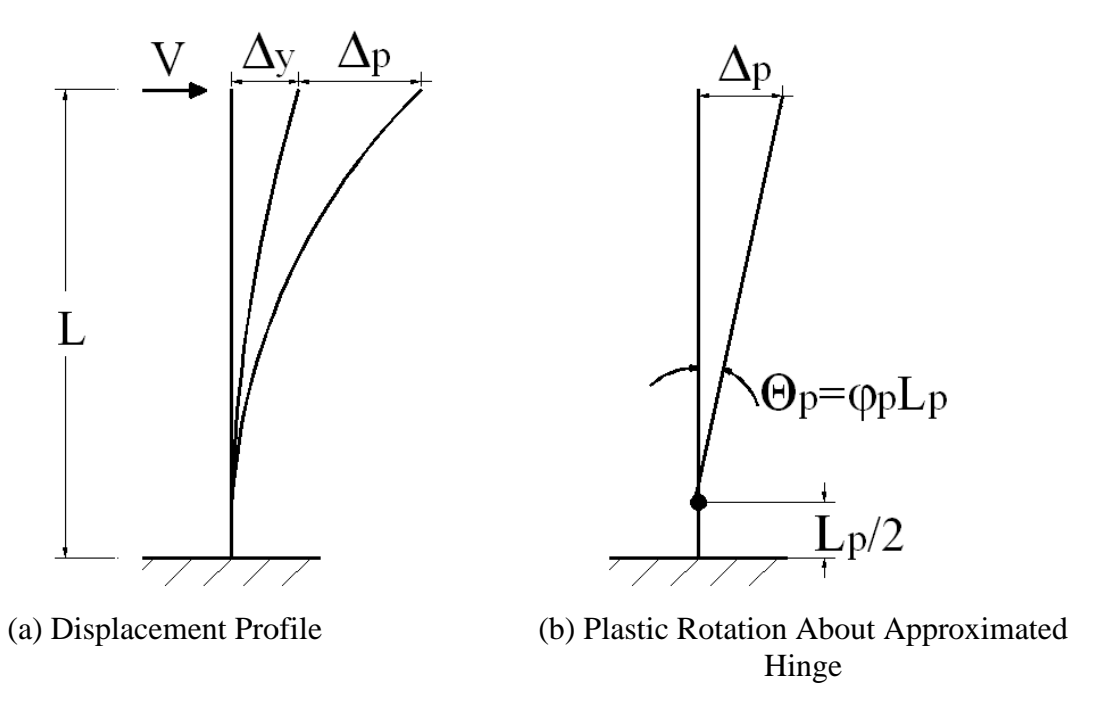


Figure 2-9: Displacement Profile and Plastic Rotation Based on Plastic Hinge Concept

#### 2.3.1 Plastic Hinge Length Design Models

The plastic hinge concept and models to define this equivalent length for reinforced concrete structures has been under study since the early 1950's. Various researchers have proposed expressions for the plastic hinge length, which are calibrated from experimental data; and all have agreed that  $L_p$  is a function of the column's length, amount of reinforcement and/or axial load level. The history of plastic hinge development over the decades was covered extensively by Hines in Chapter 2 of his doctoral dissertation (Hines 2002) and the most relevant discoveries to this research are presented in the following discussion.

Early forms of the plastic hinge length were calibrated for global limit states, such as ultimate tip displacement. In light of PBD, modern plastic hinge equations have been developed for more accurate estimation of local limit states. The plastic hinge length expressions that were

determined to be most relevant to this research are discussed in this section and in subsequent chapters.

### Priestley et al.:

Perhaps the most commonly used expression for the plastic hinge is that by Priestley et al. shown in Equation 2-8 (Priestley et al. 1996). The earliest forms of this expression can be traced to 1984 in a publication by Priestley and Park (Priestley and Park 1984). Revisions to this model were made over the past decades by Priestley and Park (Priestley and Park 1987), Priestley and Seible (Priestley and Seible 1991), Paulay and Priestley (Paulay and Priestley 1992), Priestley, Seible and Calvi (Priestley et al. 1996), with the most recent version being that by Priestley, Calvi and Kowalsky (2007) as shown in Equation 2-9. The expression consists of two components determined to have the largest effect on inelastic behavior. The first component is to account for moment gradient, and the second component accounts for strain penetration into the foundation. This expression remains the most widely known, and is also specified as the plastic hinge length to use when estimating plastic column rotations in the California Department of Transportation Bridge Design Specifications (Caltrans 2010). It is noted that Caltrans is the only seismic design code with a specified method for determining inelastic deformations, while other codes leave the method as a choice for the designer (AASHTO 2010).

$$L_p = 0.08L + 0.15d_b f_y \ge 0.3d_b f_y (ksi)$$
 2-8

$$L_p = kL + 0.15d_b f_y \ge 0.3d_b f_y (ksi)$$
 2-9

where 
$$k = 0.2 \left( \frac{f_u}{f_y} - 1 \right) \le 0.08$$

### Berry et al.:

While the plastic hinge equation by Priestley et al. is the most widely used in practice, it was calibrated based on ultimate conditions and there is no validation of its use for PBD. Lehman et al. attempted to further the understanding of issues affecting the plastic hinge region by performing experiments on columns of varying aspect ratio, longitudinal reinforcement ratio, spiral reinforcement ratio, axial load ratio, and length of confined region adjacent to the expected plastic hinge zone (Lehman et al. 2004). This research was conducted in order to determine seismic performance at several damage states for the direct application of PBD. In 2008, Berry et al. proposed a new plastic hinge expression length based directly on the findings from the Lehman et al. study and evaluation of 37 columns from the PEER Structural Performance Database (PEER 2011). Using statistical analysis from these columns, equations were proposed to evaluate effective elastic stiffness, strain at the onset of bar buckling, as well as a new expression for the plastic hinge length. This new plastic hinge length expression was meant to provide accurate estimates for intermediate limit states, besides ultimate displacement, specifically for strains at the onset of spalling and bar buckling, as is given in Equation 2-10 (Berry et al. 2008). Like the Priestley et al. expression, the Berry et al. model includes both a moment gradient and strain penetration component.

$$L_p = 0.0375L + 0.01 f_y \frac{d_b}{f_c'}$$
 (psi)

## Bae & Bayrak:

Bae and Bayrak proposed a new plastic hinge length expression about the same time as the Berry et al. expression was introduced. The researchers studied previous formulations of plastic hinge length and the discrepancies between them, specifically in their sensitivity to axial load, P. They

determined that axial load, aspect ratio and reinforcement ratio were important factors in determining the plastic hinge region. Equation 2-11 was therefore developed to determine the ultimate tip displacement of a column under a wide range of axial loads (Bae and Bayrak 2008). In this equation,  $A_{\text{S}}$  represents the area of steel,  $A_{\text{g}}$  the gross cross-sectional area, h the section depth, f'c the concrete compressive strength and fy the reinforcing steel yield strength. The expression implies that the plastic hinge region occurs at a distance 0.25h above the column/footing interface, and therefore adds this distance to the plastic hinge length. Bae and Bayrak (2008) note the calibrated plastic hinge length does not include a strain penetration component (Lsp), rather they recommend displacement due to this phenomena be calculated separately an added to the flexural deformations. Therefore in order to compare to other plastic hinge models in a finite element approach, a strain penetration component was included, as indicated in Equation 2-11. The experimental work in which this expression was calibrated included rectangular columns with very large footings. The additional stiffness provided to the column base from the large footings may be the reason for the observed damage to be a distance away from the base.

$$L_p = L\left(0.3\frac{P}{P_0} + 3\frac{A_S}{A_g} - 0.1\right) + 0.25h + L_{Sp} \ge 0.25h$$

$$where P_0 = 0.85f'_c(A_g - A_S) + f_y A_S$$
2-11

### Corley:

The expressions discussed to this point represent the most widely used and/or most recently proposed plastic hinge length models. One further plastic hinge length expression however is of interest due to its simplicity and acts as a type of control for the comparative studies presented

within the thesis. Corley (1966) is among the first researchers to document work on the plastic hinge length expression. He determined that the plastic hinge length was primarily a function of the geometry of the column section and concluded that the simple equation given in Equation 2-12 is sufficient (Corley 1966). This expression does not separate response into different components, but rather assumes that all inelastic phenomena contributing to the response may be lumped into one simple expression. Lumped plasticity approaches are used due to their simplicity, therefore if more complex plastic hinge expressions, such as those previously introduced, do not necessarily provide more accuracy, it may be seen that the Corley equation is sufficient for seismic analysis. The Corley equation does not contain a strain penetration component; however one was not added to the expression for analysis since it is assumed the simplified expression is meant to include all components of inelastic behavior as-is.

$$L_p = 0.5D$$
 2-12

#### Hines et al.:

Hines et al. realized that there are shortcomings in using a single, constant plastic hinge length in evaluating seismic performance (Hines et al. 2004). The researchers discuss that the combination of the three concepts effecting the spread of plasticity; moment gradient, tension shift and strain penetration; is not well quantified nor agreed upon among researchers. They note that newer work has been done to include the effect of tension shift but that it did not apply to a wide range of cases. Hines et al. therefore attempt to solve these issues. By testing large-scale bridge piers, the researchers have identified all three components of the plastic hinge length discussed, but found it difficult to formulate a specific plastic hinge length and base curvature based on the data. They therefore created a new approach to evaluate the spread of plasticity in the plastic

hinge region. This approach was simplified based on the assumption that plastic curvatures are distributed linearly over the length of the plastic hinge region. This assumption was determined to be valid, and to be more accurate than the assumption of plastic hinge length in which the curvatures are assumed constant.

In contrast to the previously discussed empirical plastic hinge length models, Hines et al. developed expressions estimating the plastic hinge region in which the plastic hinge varies as a function of the section's inelastic demand. Equations were derived to predict the plastic hinge region using first principles based on a free-body diagram of a cracked reinforced concrete section. Parameters of which are be obtained through a moment-curvature analysis. It should be noted that the equations given are not necessarily valid for bridge piers with axial load ratios greater than 20%. Two equations were developed to take into account the spreading of plasticity along the element's length as a function of inelastic section demand. The first is referred to as the shear crack model, the other as the bond stress model. The more accurate model depends on the type of structural system being analyzed. The shear crack model proved to be most accurate for well-confined, slender, circular columns and is shown in Equation 2-13 (variables are defined in Table 2-2). The bond stress model describes the effect of tension shift but only partially captures the moment gradient effect. The bond stress model is given in Equation 2-14. In well-confined, slender columns, the spread of plasticity is much greater than predicted by the bond slip model. The crack angle within the plastic hinge would have to be less than 15 degrees in order to capture the full effect. Therefore the shear crack model was developed to limit the crack angle by the estimated shear cracking behavior of the column and better capture the spread of plasticity in such columns. Using these models, Hines et al. compared the experimental data to the monotonic envelopes formed from the shear crack model as well as the Priestley  $L_p$  model, verifying accuracy of the shear crack model. While the methods in the Hines et al. study showed accuracy for predicting ultimate displacement and the hysteretic envelope (i.e., monotonic response) to a cyclically loaded member, it does not explicitly discuss the implications for use in PBD or prediction/quantification of intermediate limit states. The models presented by Hines et al. certainly take more realistic behavior into account; however, the requirement of a sectional analysis as well as the complexity of the equations has hindered its adoption into regular practice by researchers.

$$L_{pr} = \left(T - T_{yav}\right)\frac{jd}{V} + \frac{V}{2\left(\frac{A_v f_{yv}}{S} + f_1 t_w\right)} \ge 0$$
2-13

$$L_{pr} = jdcot\theta = \sqrt{\frac{2(T - T_{yav})jd}{\left(\frac{A_v f_{yv}}{s} + v_{cr} t_w \frac{2d_{cr}}{jd}\right)}}$$
2-14

Table 2-2: Symbol Definitions for Implementation of Hines et al. Plastic Hinge Model

$A_{V}$	Area of transverse steel at a given level	
С	Net compressive force	
d <sub>cr</sub>	Distance between $T_{CT}$ and $C$ , from moment-curvature analysis	
$f_1$	Principle tensile stress	
$f_{yy}$	Transverse reinforcement yield stress	
jd	Distance between flexural tension centroid and compression centroid	
T	Flexural tensile force resultant	
T <sub>cr</sub>	Vertical flexural tensile concrete force resultant	
T <sub>yav</sub>	Effective flexural tensile yield force resultant	
V	Horizontal force applied to test unit	
v <sub>cr</sub>	Horizontal tensile concrete stress	

### 2.3.2 Parameters Affecting Lp

As discussed in Section 2.3.1, there are many parameters that affect the plastic hinge length, however not all researchers agree on the significance of each. These parameters include materials strength, such as steel yield strength (f<sub>y</sub>) and concrete compressive strength (f'<sub>c</sub>), axial load (P), reinforcement ratio and aspect ratio. While the model by Bae and Bayrak (2008) addresses the majority of these factors, other researchers such as Priestley et al. (1996, 2007) and Berry et al. (2008) have determined that moment gradient and reinforcement have the largest affect on the plastic hinge, while parameters such as axial load and aspect ratio are relatively insignificant. The significance of these parameters, as well as how sophisticated a model should be at the expense of simplicity remains a topic of discussion amongst the research community.

## 2.4 Numerical Analysis Methods

Several nonlinear beam and beam/column finite elements have been developed over the past three decades in order to perform numerical analyses and simulations of the inelastic response of reinforced concrete columns under seismic demands. The numerical approaches can generally be placed into two categories for nonlinear beam elements: lumped plasticity and distributed plasticity models. For both cases, discrete and fiber-based formulations have been developed.

Discrete formulations use single or multi-component nonlinear springs to capture the elements inelastic force-deformation relation. Plasticity-based discrete formulations have also been proposed. Most discrete models concentrate the inelastic response at the element ends, but the definition of serial models (e.g., multiple springs and multiple yield functions) has been proposed to allow these elements to capture the spread of plasticity.

Fiber-based models have become increasingly popular over the last two decades due to their increased accuracy over models that assume a generalized element response. Fiber models consider the detailed description of the geometry and material properties to evaluate the behavior of critical sections rather than a simplified and predefined set of hysteresis rules. The element's inelastic force-deformation response is thus obtained by analyzing single or multiple discretized cross-sections (see Figure 2-10.) and then interpolating the nonlinear response along the element in either displacement-based or force-based formulations. The following discussion on lumped and distributed plasticity elements is therefore with regard to fiber-based nonlinear beam-column elements. The lumped plasticity approach is advantageous due to its computational efficiency and for its analogy to simple elasto-plastic analysis procedures used in design practice. The distributed plasticity approach, however, is convenient for defining limit states for PBD since it has the ability to capture local behaviors at intermediate element lengths and takes the spread of plasticity along an element length into account. Both approaches and the concepts behind their derivation are discussed next.

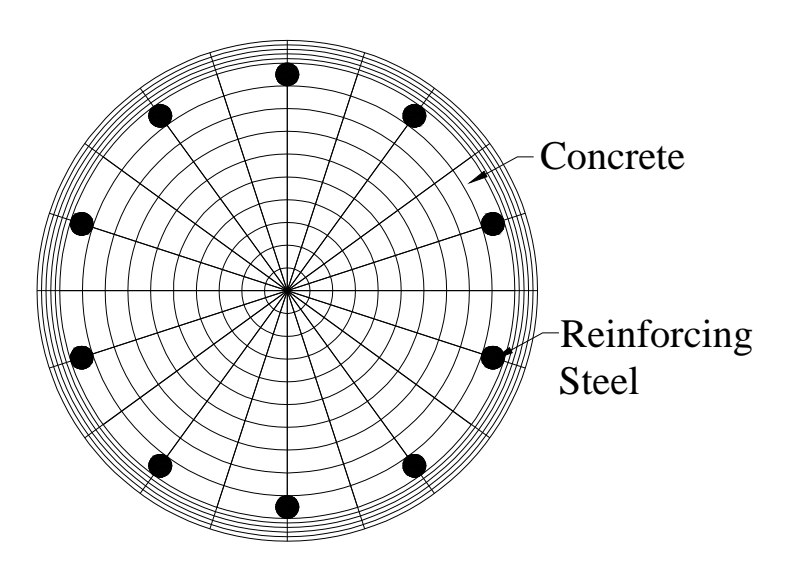


Figure 2-10: Discretized Fiber Section

## 2.4.1 Lumped Plasticity Models

The lumped plasticity approach utilizes the simplicity of the plastic hinge concept by separating a line element into elastic and inelastic components. A fixed point or predetermined length, typically the plastic hinge length, is determined to be the region in which all inelastic action is concentrated, while elastic properties are assigned to the remainder of the element. The inelastic behavior in the plastic hinge is determined from a sectional analysis of the critical section, which has detailed description of the geometry and material properties (uniaxial constitutive models) assigned to sections within this region. Uniaxial constitutive material models for both steel and concrete are defined and assigned to the corresponding components of a discretized section. This section is then assigned to the plastic hinge(s) of the element as shown in Figure 2-11. Determining the section's behavior usually requires a sectional analysis be completed first, and then the moment-curvature relationship is assigned to the plastic hinge(s) to determine the element response under external loads. Other methods define a backbone force-displacement hysteresis response to the plastic hinge(s). Such methods are acceptable when the element behavior is previously well known and does not require the initial sectional analysis.

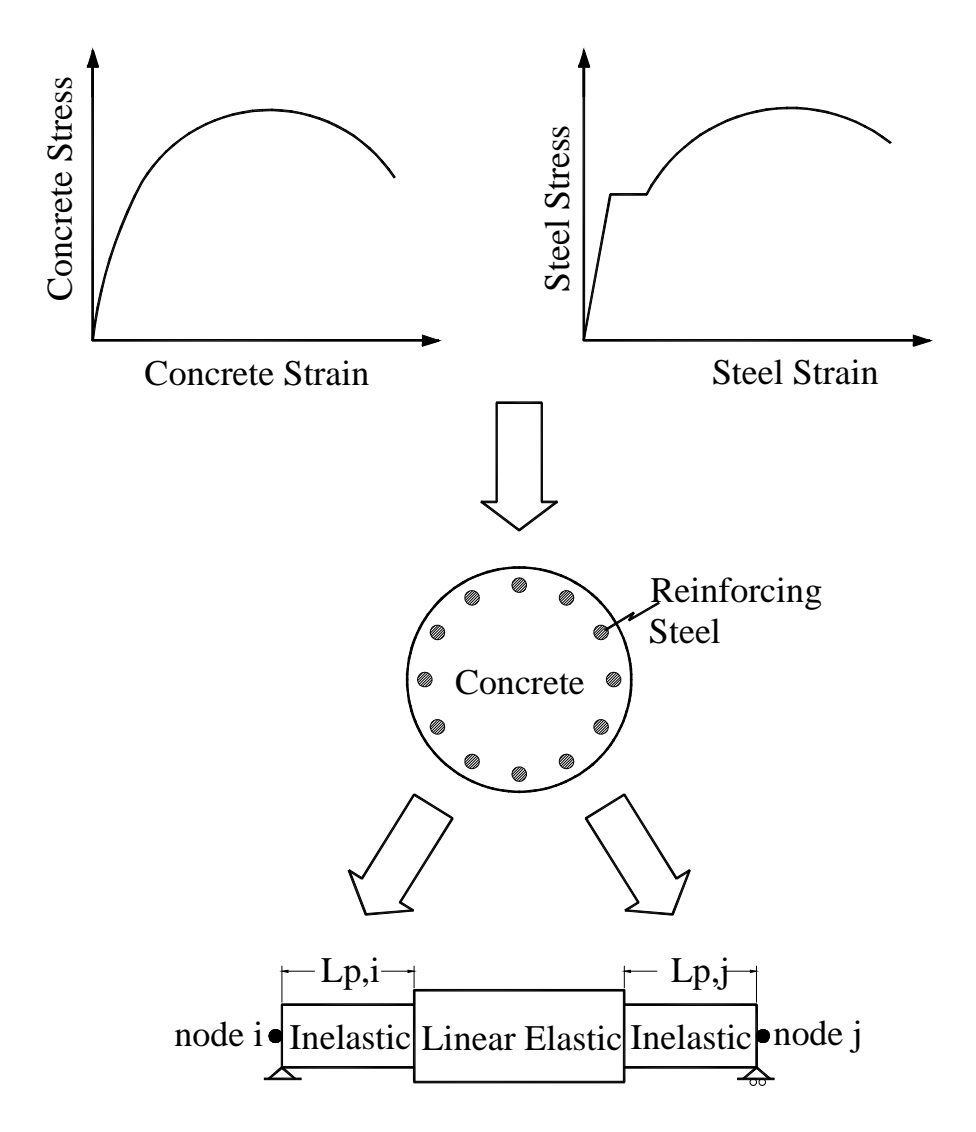
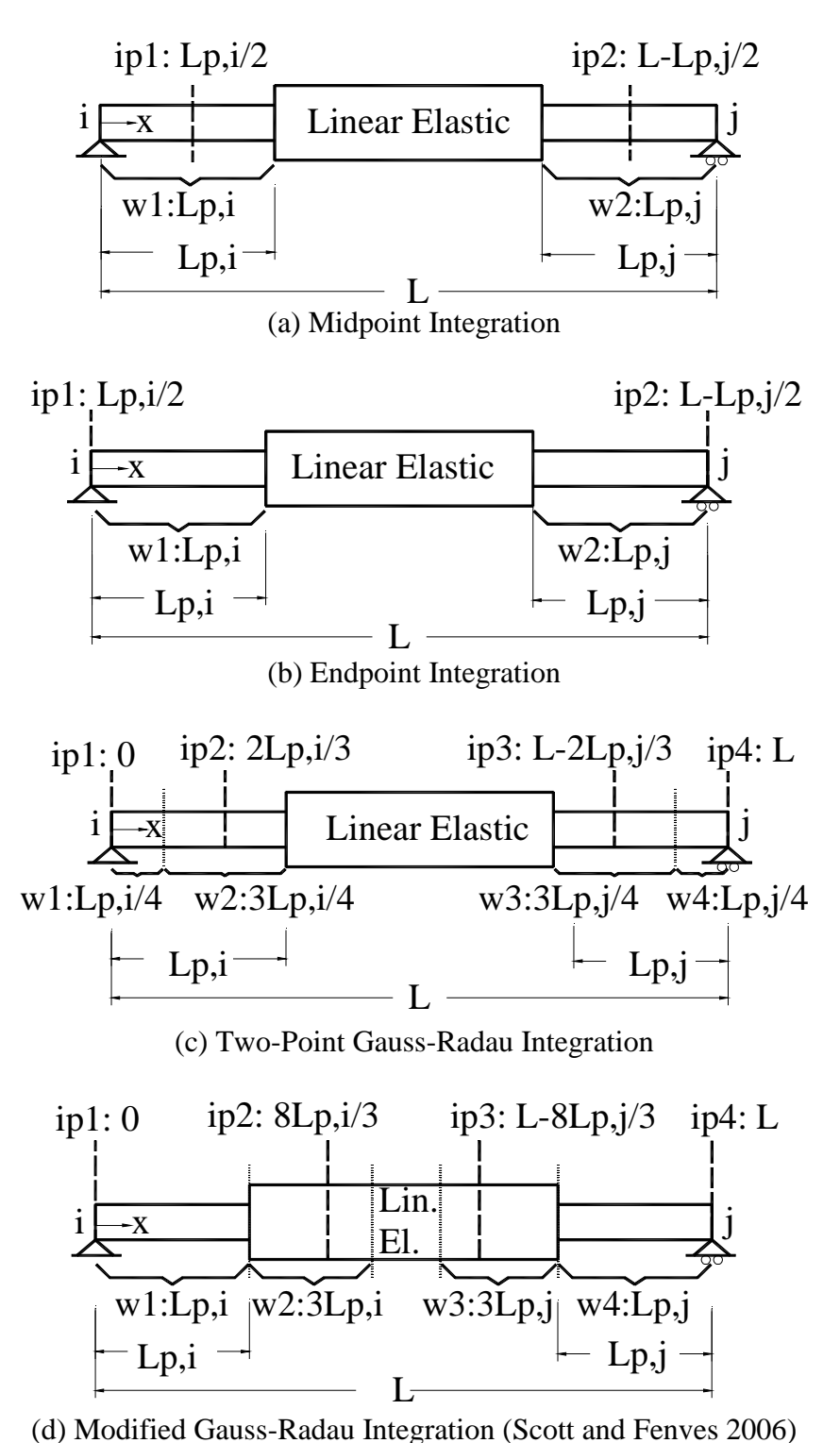


Figure 2-11: Schematic of Defining Inelasticity in a Lumped Plasticity Element

Assuming all inelasticity occurs at a single point is clearly the simplest method in analyzing a lumped plasticity element. Assuming inelastic behavior over a given length, however, requires integration techniques within the plastic hinge. Techniques for the distribution of inelastic strains and curvatures within the plastic hinges of the element have been proposed by various researchers. Simple schemes may monitor behavior at the center of the inelastic region or at the end node of the element and assume that inelastic curvatures are constant throughout the section. These however do not offer high accuracy. More sophisticated schemes include using two-point

Gauss-Radau integration which monitors behavior at the end node of the element and also at two-thirds the length of the inelastic region. Curvatures are assumed linear between integration points but the integration weights cause the input length to equate  $L_p$  when deformations localize within this region. Two integration points within the plastic hinge is less computationally efficient than using one point, therefore Scott and Fenves (2006) proposed an integration scheme that uses one integration point per plastic hinge while obtaining the accuracy of two (Scott and Fenves 2006). This method applies the Gauss-Radau integration over four times the plastic hinge where behavior is linear elastic. By adjusting the integration weights and assuming linear curvatures, the behavior within the plastic hinge may be calculated, again equating the plastic region to L<sub>p</sub>, for which the plastic hinge models are intended. These various integration approaches are shown in Figure 2-12 where "ip" indicates the integration points and "w" indicates the integration weights used for each point. The assumption in lumped plasticity models of a constant curvature over the plastic hinge length is described in Section 2.3 and in Figure 2-8. The assumed distribution of the modified Gauss-Radau integration scheme is shown in contrast to a fixed-length hinge model in Figure 2-13 (note that  $L_p$ ' is shown instead of  $L_p$  for consistency since a strain penetration component is not shown). It is seen that although the curvature distribution between integration points is linear, the Lp value used for calculations using this scheme is the same as that used in the fixed-length model (Berry et al. 2008, Scott and Fenves 2006). This is due to the integration weights shown in Figure 2-12d.



(d) Wouthed Gauss-Radau Integration (Scott and Penves 2000)

Figure 2-12: Integration Methods for Lumped Plasticity Elements

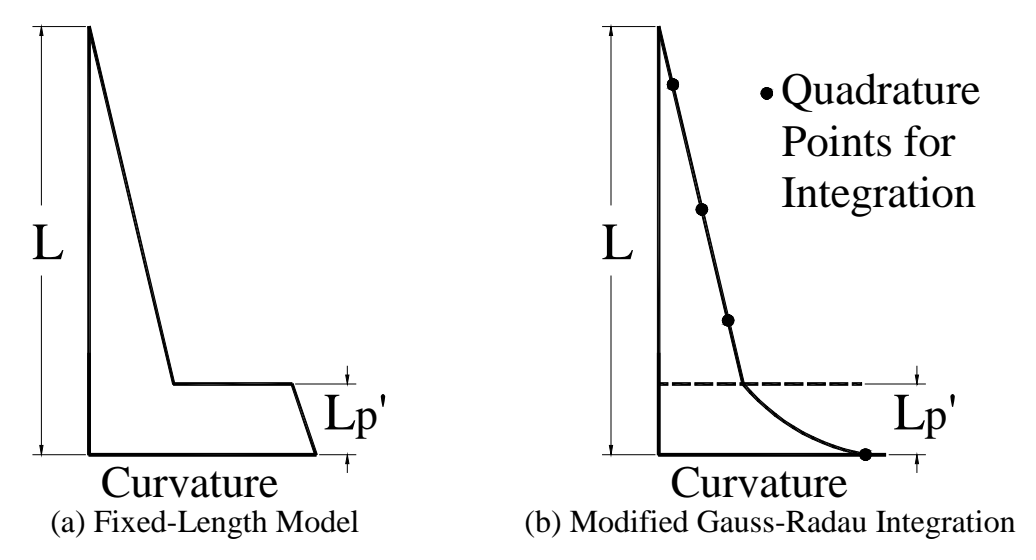


Figure 2-13: Assumed Curvature Distribution in Lumped Plasticity Models

The lumped plasticity approach is advantageous due to its simplicity, however it has serious limitations since inelastic flexural deformation are assumed to be concentrated at a hinge with predefined and constant length, which is dependent on material properties, boundary conditions and actual spread of plasticity. Because of these assumptions, a lumped plasticity approach is limited to strain-softening response and is unable to capture strain-hardening behavior (Lee and Filippou 2009).

## 2.4.2 Distributed Plasticity Models

Distributed plasticity approaches are more accurate than lumped approaches since the assumption of a lumped element (all inelastic behavior being lumped at the ends) is physically impossible (Spacone and El-Tawil 2004). In a distributed plasticity approach behavior is monitored at several integration points along an element length where inelastic behavior is allowed to occur. Like the lumped approach, constitutive material models are applied to a discretized section to account for the inelastic behavior. Rather than being applied to a single

point or region, however, the distributed approach applies the discretized section to each integration point along the element, as shown in Figure 2-14. At any time step within an analysis, the sectional response at each integration point along the element is evaluated. This approach therefore more accurately captures the spread of plasticity along an element.

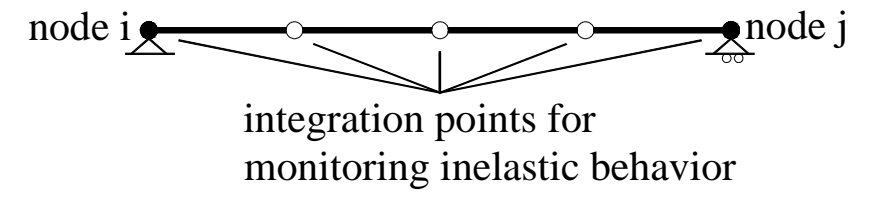


Figure 2-14: Schematic of Element in a Distributed Plasticity Approach

In a distributed plasticity approach the user generally defines the location and weights of integration points along an element; however, the most common approach is the Gauss-Lobatto integration. This scheme places an integration point at each end of an element, where extreme behavior typically takes place, as well as 'n' equally spaced integration points along the element length (Neuenhofer and Filippou 1997). For example, the integration scheme shown in Figure 2-14 would represent Gauss-Lobatto integration with 5 integration points. Deformations between each integration point are assumed to be linear with the Gauss-Lobatto or any other integration scheme. It is therefore intuitive that the more integration points used, the more representative an element is of actual structural behavior.

While the distributed plasticity approach offers the advantage of capturing spreading plasticity, it also has limitations. Increasing the number of integration points in an element where inelastic behavior does not spread the entire length is computationally wasteful and determining the most effective number and placement of integration points is not a straightforward task. Furthermore,

distributed plasticity approaches assume a strain-hardening response and fail to capture strainsoftening. Therefore the approach used, either lumped plasticity or distributed plasticity, may require some previous knowledge on the expected behavior of the structural element.

### 2.5 P-Delta Effects

Due to the focus on slender columns in this research, P-delta effects become a topic of discussion as future results are presented. According to modern seismic design codes, P-delta effects can typically be ignored if specific criteria are met. According to the California Department of Transportation Seismic Design Criteria, P-delta effects can typically be ignored if the following equation is satisfied (Caltrans 2010):

$$P\Delta \leq 0.20M_y$$
 2-15

According to AASHTO LRFD Bridge Design Specifications, P-delta effects can be ignored if the following is met (AASHTO 2010);

$$\frac{KL_u}{r} < 22$$

where  $KL_u$  is the effective column length and r is the radius of gyration. Of the five case study columns discussed in Chapter 5 of this thesis, only one satisfies this requirement, thus indicating the importance of P-delta in the design of slender columns.

P-delta effects are second order effects that magnify the internal forces and soften the response of a structure. P-delta effects are manifested at both the structural level (P- $\Delta$ ) and the element level (P- $\delta$ ), as seen in Figure 2-15a (Schellenberg et al. 2008). Global second order effects or P- $\Delta$  are caused when displacements are large and in combination with an external axial force cause additional overturning moment forces at the base of the column (Figure 2-15b). At the element

level, the internal axial force causes instability of the structural member, causing softening or even buckling. These are known as the geometric second-order effects, or P-δ. As lateral loads are induced, P-delta effects not only reduce the initial stiffness of a column, but drastically reduce post-yield stiffness as well, which could even become negative, as shown in Figure 2-15c (Priestley et al. 1996). The importance of P-delta effects on global response is well known, however there is limited research on the effect of local response and intermediate limit states.

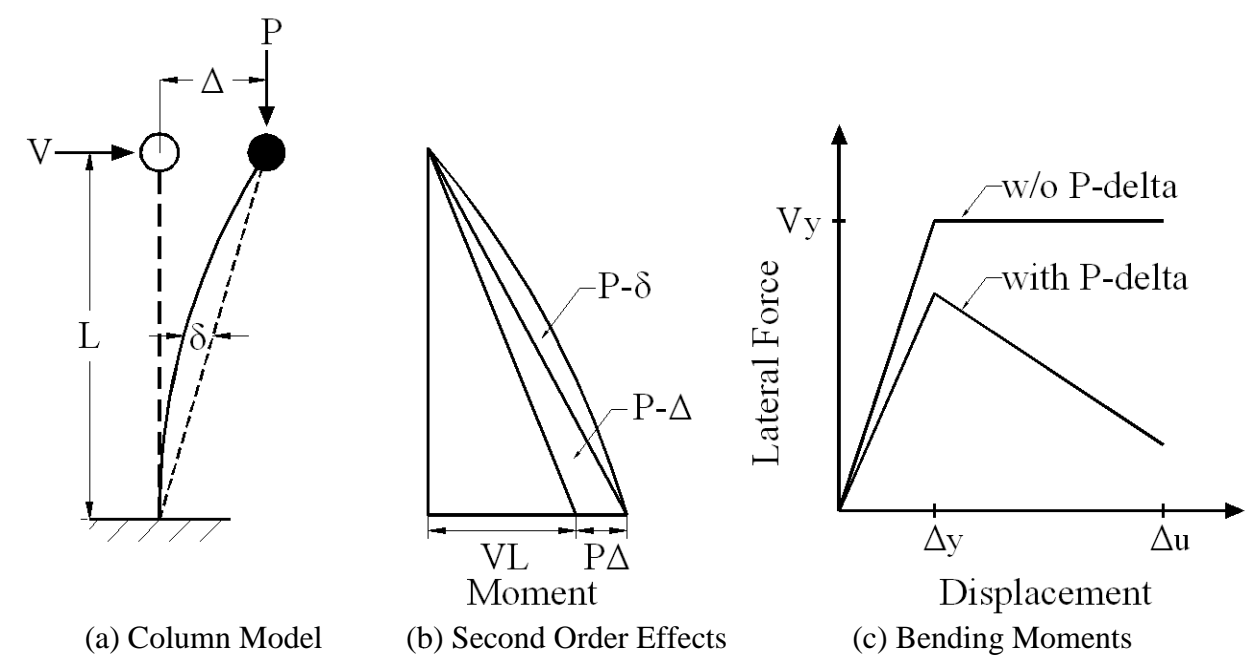


Figure 2-15: P-Delta Effects on Bridge Columns (Adapted from Priestley et al. 1996, Abell 2012)

### 3 METHODS

This chapter describes the numerical and experimental methods used for testing the hypotheses outlined in Chapter 1. First discussed are the analysis techniques in which all subsequent numerical models are based. Following is a description of experimental method followed in the test a half-scale reinforced concrete column used as part of the numerical analysis evaluation in Chapter 5.

## 3.1 Analysis Methods

The subsequent sections of this chapter describe the finite element platform and specific elements used to perform the analyses throughout this thesis. The models used to implement the approaches previously described are discussed in detail and will be referred to in the following chapters to indicate the exact models used in the modeling of all columns.

# 3.1.1 OpenSees

The finite element platform used in all the analyses described in this thesis is the Open System for Earthquake Engineering Simulation or OpenSees (OpenSees 2011). This program is an open-source program originally developed at the University of California, Berkeley as a software framework for simulating the seismic response of structural and geotechnical systems, and has been developed as the computational platform for research in performance-based earthquake engineering at the Pacific Earthquake Engineering Research (PEER) Center. OpenSees has advanced capabilities for modeling and analyzing the nonlinear response of systems using a wide range of material models, elements, and solution algorithms specifically aimed for simulating the seismic response of structures that exceed the available capabilities of general purpose finite element programs, particularly for reinforced concrete structures.

A structural member that is subject to both axial load and bending moments, such as the columns of interest, is referred to as a beam-column element. OpenSees provides several types of beam-column elements for structural models. A wide range of uniaxial materials and section models are also available for beam-column elements.

# 3.1.1.1 Lumped Plasticity Element

Lumped plasticity analyses are conducted in OpenSees by using the "beamWithHinges" element, which follows the modified Gauss-Radau integration scheme as discussed in Section 2.4.1. This element uses flexibility formulation and assumes all inelastic behavior is concentrated over a user-defined length at the element ends, as described for the lumped plasticity approaches in Chapter 2. The element allows for a plastic hinge at either end of an element. However, for analysis of a cantilever column the plastic hinge is defined at the column base only, defining the plastic hinge at the other end of the column as zero. The inputs necessary to define a lumped plasticity element in OpenSees include: location of the element nodes, the length of the plastic hinge(s), a fiber-based section with inelastic material models, which is assigned to the plastic hinge region, and the elastic modulus (E), area (A), and moment of inertia (I), which are assigned to the elastic region of the element. A schematic of a column discretized into a lumped plasticity element is shown in Figure 3-1a, where L<sub>p</sub> is one of the plastic hinge lengths discussed in Section 2.3.1.

### 3.1.1.2 Distributed Plasticity Element

Distributed plasticity analyses are conducted in OpenSees using a "nonlinearBeamColumn" element. This element uses either force-based or displacement-based formulation to analyze element behavior. Used in the following analyses is a displacement-based formulation in which

and 2-3. OpenSees allows multiple integration schemes for analysis of this element; however the Gauss-Lobatto integration discussed previously was used in this research due to its advantages over other schemes. OpenSees also allows an element to be divided into several sub-elements. The advantage of using sub-elements is the ability to extract global force data (data which is typically only available at element ends) from several intermediate nodes. Inputs required for a distributed plasticity element in OpenSees include the number of sub-elements, number of integration points per sub-element, and the definition of a fiber-based section to be applied to each integration point for analysis. The Gauss-Lobatto scheme implemented for the analyses in this thesis had three sub-elements and three integration points per sub-element. The number of sub-elements and integration points was chosen to monitor behavior at every sixth of the column length. This is thought to capture relatively accurate data while not being computationally wasteful. A schematic of the distributed plasticity element used for the analyses in this thesis is shown in Figure 3-1b.

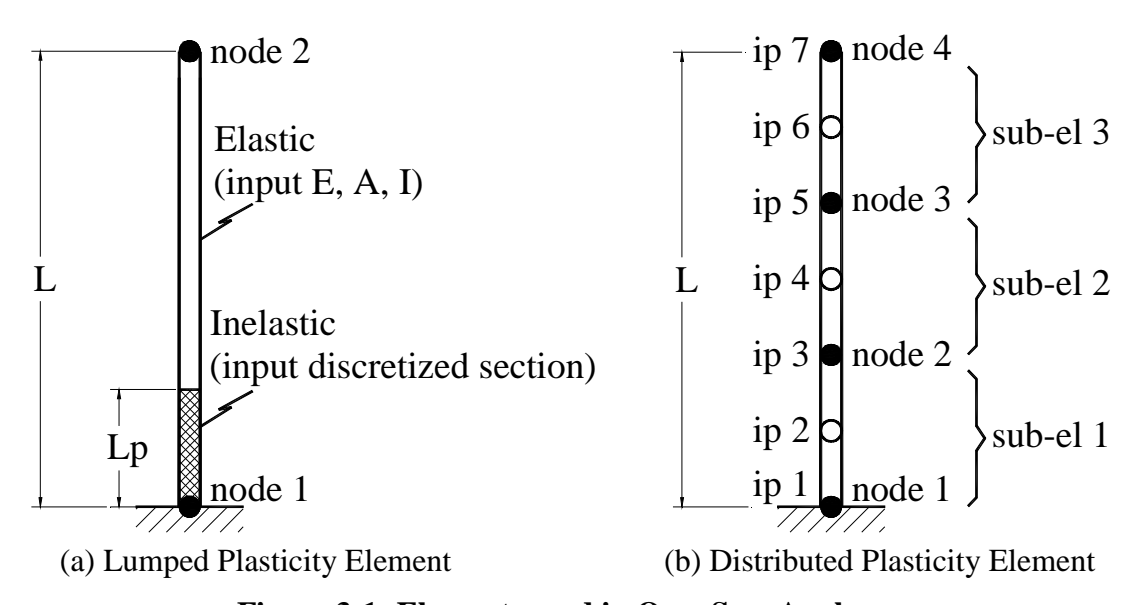


Figure 3-1: Elements used in OpenSees Analyses

### 3.1.1.3 Material Models

OpenSees offers a wide range of material models to represent the material behavior of fiber sections. The specific material models used in the following analyses are described in this section. The input required for each model is given, along with any assumptions necessary to implement the material model into the OpenSees analyses. All analyses described in subsequent chapters use the same material models described here, varying only by the material strengths defined by the corresponding test unit material testing program.

The longitudinal reinforcing steel of the column sections was modeled using OpenSees material model "ReinforcingSteel," which is based on the commonly used Chang and Mander uniaxial steel model (Chang and Mander 1994). Several parameters are needed to define the stress-strain curve of the steel material model, as shown in Figure 3-2. The definitions of these parameters along with the values used are given in Table 3-1. As seen, yield strength is the only parameter typically given in experimental documentation, therefore varying between column models. The remaining parameters were defined based on common observed relations and/or values.

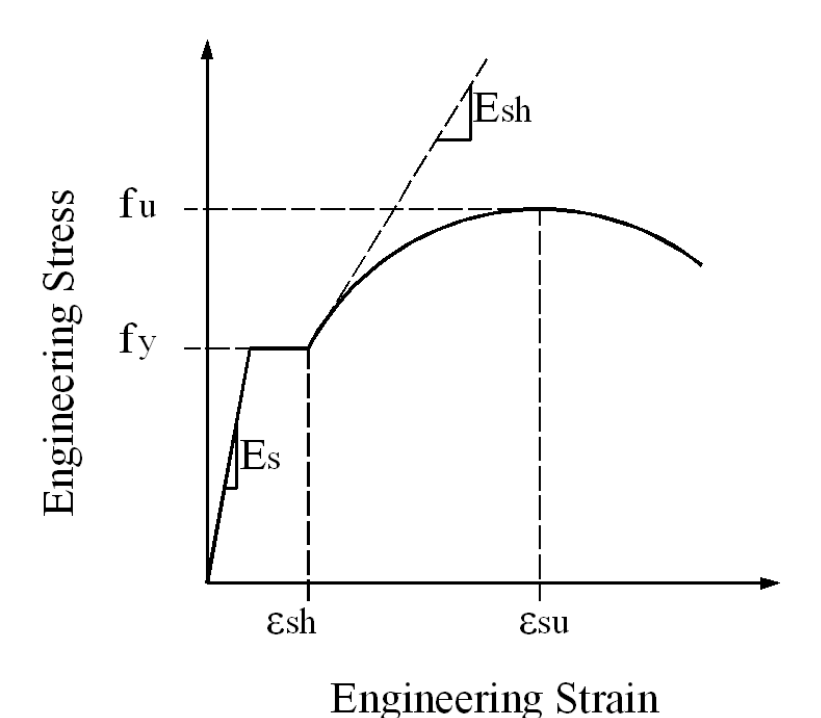


Figure 3-2: Reinforcing Steel Model

Table 3-1: Assumed Reinforcing Steel Material Properties in OpenSees Modeling

Input Parameter	Assumed Value	
Yield Strength (fy)	Given in documentation (varies)	
Ultimate Strength (f <sub>u</sub> )	$1.5f_{y}$	
Elastic Modulus of Steel (E <sub>s</sub> )	29,000 ksi	
Elastic Modulus after Strain Hardening (E <sub>sh</sub> )	1633 ksi	
Strain at Hardening $(\varepsilon_{sh})$	0.0036	
Ultimate Strain ( $\varepsilon_{su}$ )	0.1	

When performing a monotonic analysis, the above model is sufficient for reinforcing steel. This reinforcement however is sensitive to loading pattern when performing a cyclic analysis. Tensile strains will accumulate during repeated loading, creating a softening response in the steel. To simulate this behavior, OpenSees offers several optional input parameters to the "ReinforcingSteel" model. The cyclic material model used in analyses in this thesis was the

Gomes and Appleton buckling model for nonlinear cyclic response (Gomes and Appleton 1997).

Use of this model requires the input of four additional parameters:

ullet Slenderness ratio,  $L_{sr}$ . This parameter describes the slenderness of an individual reinforcing bar to take into account its susceptibility to buckling. The slenderness ratio of a bar is defined as:

$$L_{ST} = \frac{L_u}{d_h}$$
 3-1

where  $d_b$  is the bar diameter and  $L_u$  is the unsupported bar length, typically the spacing between transverse reinforcing spirals, as shown in Figure 3-3. In this study however,  $L_u$  was taken as twice the spiral spacing, since the spiral spacing in many cases is 4 inches or less, resulting in an unlikely scenario that a reinforcing bar will buckle over this short distance.



Figure 3-3: Bar Slenderness Parameters for Gomes and Appleton Cyclic Steel Model

• Amplification factor for the buckled stress-strain curve,  $\beta$ . This parameter scales the buckling curve of the stress-strain relationship, as shown in Figure 3-4, where the variables are defined in Gomes 1997. The  $\beta$  factor is typically taken as 1.0, and is therefore the value used for the OpenSees models in this study.

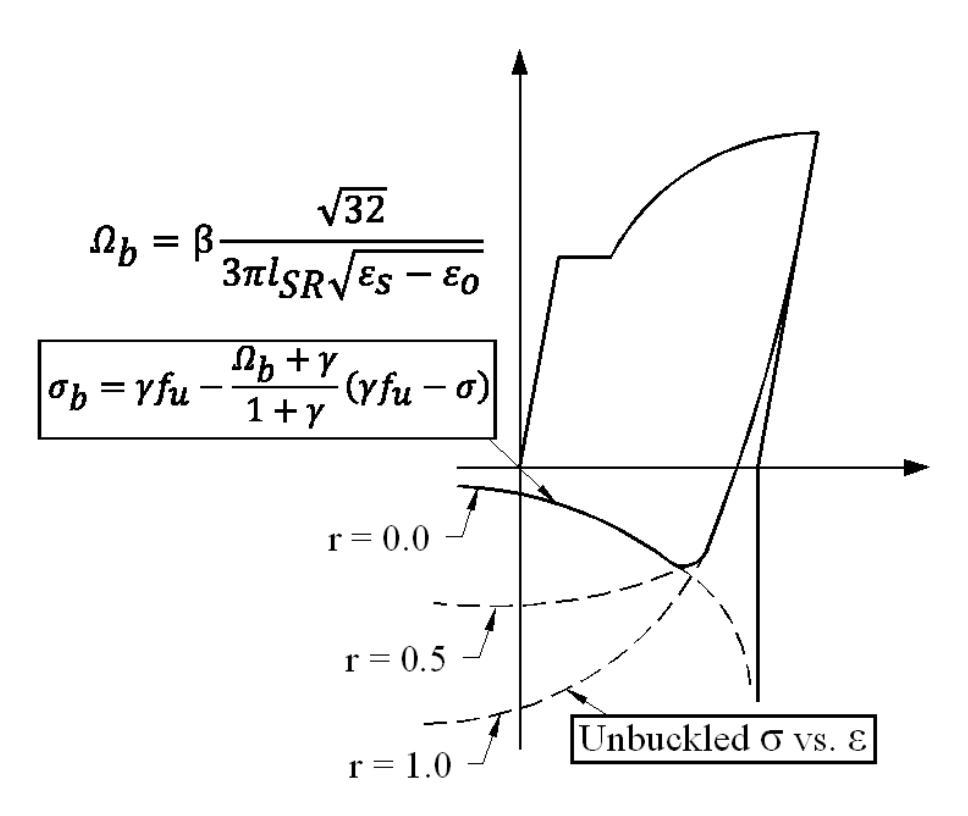


Figure 3-4: Buckling Parameters as Defined by the Gomes and Appleton Model for Cyclic Steel Behavior (Adapted from Gomes and Appleton 1997)

- Buckling reduction factor, r. This parameter is used to adjust the curve between the buckled and unbuckled curve as shown in Figure 3-4. The r factor may be any real number between 0 and 1.0. Since this model is applied to a wide range of flexural columns in which the individual material behavior is unknown, an intermediate value of r equal to 0.5 was used.
- Buckling constant,  $\gamma$ . This parameter is the stress location about which the buckling factor, r, is initiated. The  $\gamma$  factor is typically used to avoid kinks in the reloading branch of the stress-strain response of the material and may be a real number between 0 and 1.0 (OpenSees 2011). Again, an intermediate value of 0.5 was chosen in this study.

OpenSees does not contain a specific material model for the transverse steel reinforcement, but rather allows the definition of the concrete in a section into two separate models: one to simulate normal, unconfined concrete response and the other to simulate the confined concrete within the confinement reinforcement, as shown in Figure 3-5. Given that the purpose of transverse steel is to enhance the core concrete behavior this method of modeling is quite accurate. Two OpenSees concrete materials were therefore used in the modeling of the fiber sections. The unconfined concrete section was modeled with OpenSees material, "Concrete01", which follows a typical Kent-Scott-Park uniaxial material model (OpenSees 2011). This model assumes a concrete material with zero tensile strength and degraded linear unloading/reloading stiffness as shown in Figure 3-6. The required input parameters for this material model along with their assumed values are given in Table 3-2.

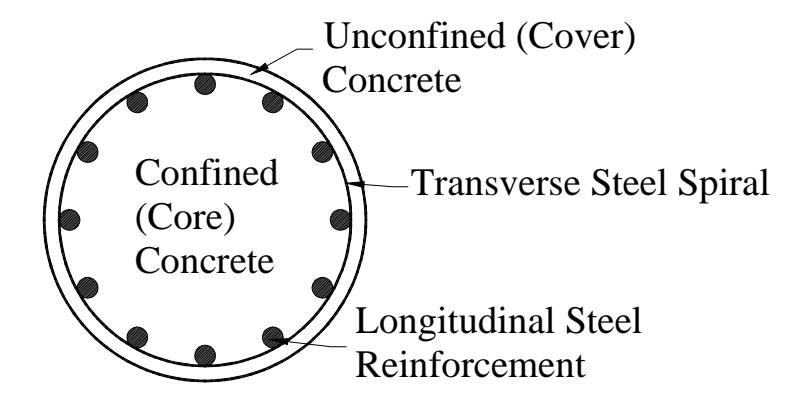


Figure 3-5: Typical Reinforced Concrete Section for Circular Columns

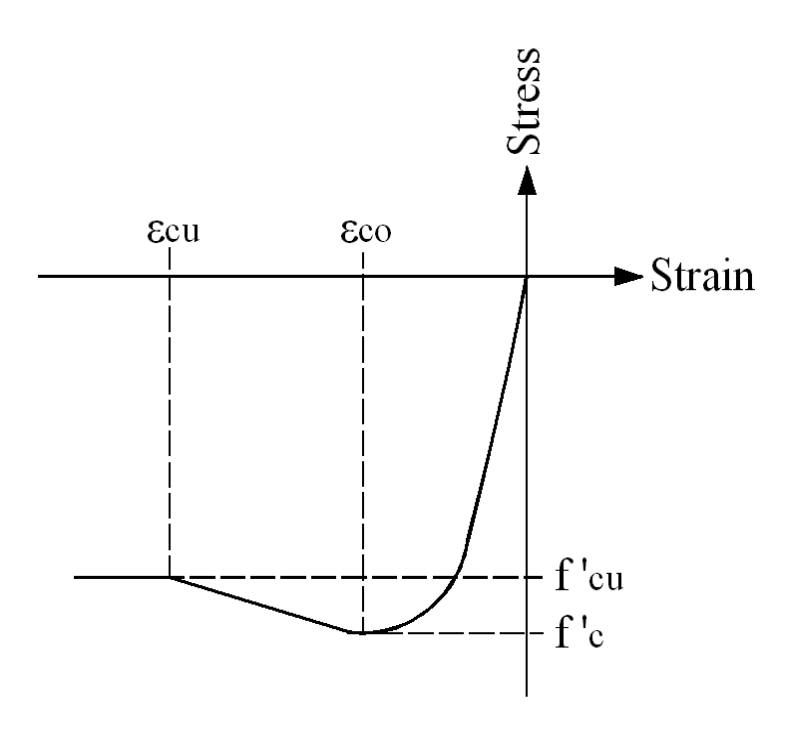


Figure 3-6: Zero-Strength Concrete Material Model

Table 3-2: Assumed Unconfined Concrete Material Properties in OpenSees Modeling

Input Parameter	Assumed Value	
Compressive Strength at 28 days (f'c)	Given in documentation (varies)	
Strain at Maximum Strength ( $\varepsilon_{c0}$ )	0.002 in/in	
Crushing Strength (f'cu)	1.0 ksi	
Strain at Crushing Strength (ε <sub>cu</sub> )	0.01 in/in	

The confined concrete region was modeled with OpenSees material, "Conrete07," which is an implementation of the Chang and Mander concrete model (Chang and Mander 1994). This model takes into account the increase of strength and ductility provided by transverse steel reinforcement (see Figure 3-7). The implementation of this model in OpenSees requires the input of eight parameters as outlined in Table 3-3. Chang and Mander proposed that the increased

compressive strength of concrete due to confinement is a function of the unconfined strength and the effective lateral confinement stress,  $K_e f_l$ :

$$f'_{cc} = f'_{c} \left( 2.25 \sqrt{1 + \frac{7.94 K_{e} f_{l}}{f'_{c}}} - \frac{2 K_{e} f_{l}}{f'_{c}} - 1.254 \right)$$
3-2

where  $K_e$  is the effectiveness of confinement (95% for circular sections) and  $f_l$  is the volumetric reinforcement ratio as defined in Equation 3-3.

$$f_l = \frac{1}{2}\rho_S f_{YS} \tag{3-3}$$

In the above expression,  $f_{ys}$  is the yield strength of the transverse steel and  $\rho_s$  is the spiral or transverse reinforcement ratio:

$$\rho_S = \frac{4A_S p}{D's}$$

where  $A_{sp}$  is the cross-sectional area of the transverse steel bar, D' is the outer diameter of the spiral and s is the spacing of the spiral pitch, shown in Figure 3-8. The strain at peak confined compressive strength is defined by Chang and Mander in Equation 3-5, where  $\epsilon_{co}$  is typically taken as 0.002.

$$\varepsilon'_{CC} = \varepsilon_{CO} \left[ 1 + 5 \left( \frac{f'_{CC}}{f'_{C}} - 1 \right) \right]$$
 3-5

The elastic modulus of concrete used for implementation of this model is:

$$E_C = 57,000\sqrt{f'_C} \ (psi)$$
 3-6

which is typical for normal weight concrete. Tensile properties of the confined concrete model are defined by the tensile strength:

$$f_t = 7.5\sqrt{f'_c} \ (psi)$$
 3-7

And the tensile strain at maximum stress is:

$$\varepsilon_t = \frac{f_t}{E_c}$$
 3-8

The remaining non-dimensional terms required for implementing the OpenSees "Conrete07" material model represent simplified loading and unloading branches of the uniaxial material (see Figure 3-9):

$$x_p = 3$$
 3-9

$$x_n = \frac{\varepsilon_{c0}}{\varepsilon'_{cc}}$$
 3-10

$$r_{C} = \frac{E_{C}}{E_{C} - f'cc/\varepsilon'_{cc}}$$
3-11

The input parameters for the above documented material models and other basic information such as geometry and axial load for the case studies considered in this thesis were obtained from databases and test reports on the respective tests All other parameters for implementing the material models were assumed values as discussed or calculated by the equations given in this chapter.

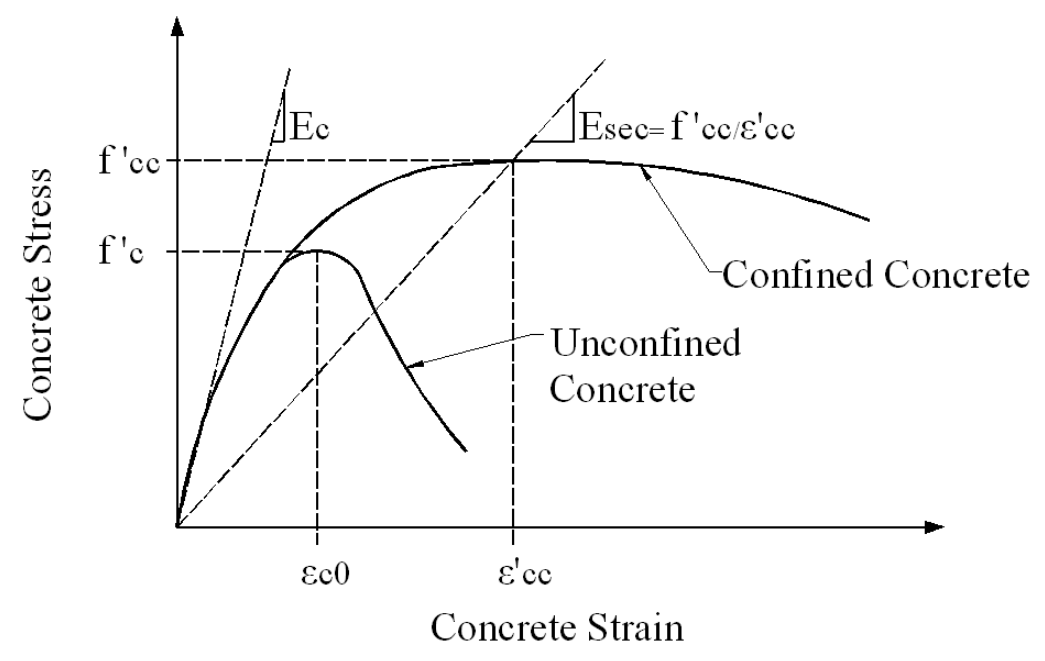


Figure 3-7: Confined versus Unconfined Concrete (Adapted from Priestley et al. 1996)

Table 3-3: Definition of Terms for Confined Concrete Material Model

Input Parameter	Definition	
f'cc	Confined Concrete Compressive Strength	
ε'cc	Strain at Maximum Compressive Strength	
E <sub>c</sub>	Initial Concrete Elastic Modulus	
$f_{t}$	Tensile Strength of Concrete	
$\epsilon_{t}$	Tensile Strain at Maximum Tensile Strength	
x <sub>p</sub>	Non-dimensional term that defines the strain at which the straight line descent begins in tension	
x <sub>n</sub>	Non-dimensional term that defines the strain at which the straight line descent begins in compression	
r <sub>c</sub>	Parameter that controls the nonlinear descending branch	

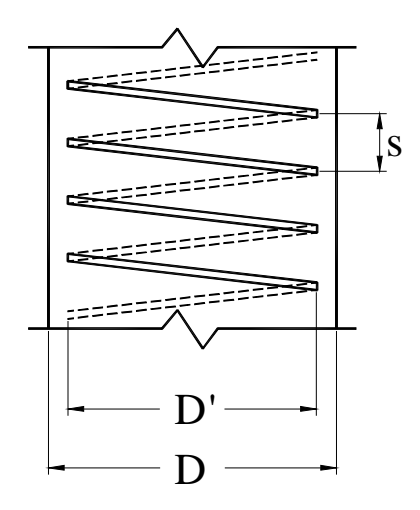


Figure 3-8: Portion of Column in Elevation Defining Transverse Reinforcement Terms

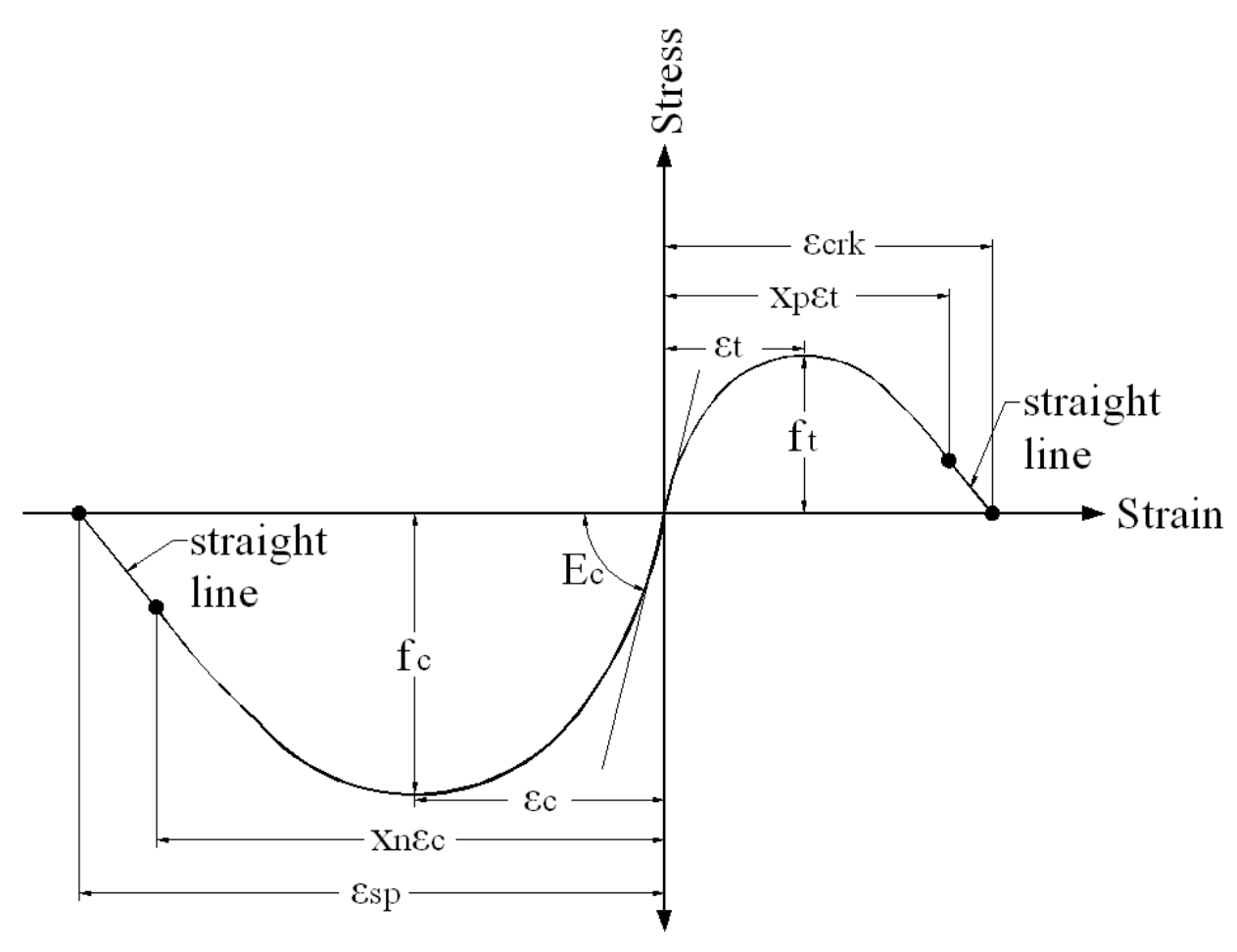


Figure 3-9: Concrete Material Envelope and Variable Definitions (Adapted from OpenSees 2011)

## 3.2 Experimental Methods

In order to evaluate the spread of plasticity and numerical accuracy in predicting the inelastic response of reinforced concrete columns with high aspect ratio, a column of aspect ratio 12 was tested at the Civil Infrastructure Laboratory at Michigan State University. This column was tested in order to complete a data set of varying aspect ratio for an evaluation of slenderness. The distribution of slenderness in the PEER Structural Performance Database was shown in Figure 1-2. Most columns that have been tested in an experimental setting are below aspect ratio 6. Just two columns have been tested with aspect ratio 10 and none have been tested with aspect ratio 12. This test will therefore complete the column series desired for understanding the effects of slenderness as well as provide new data for a column more slender than other previously reported.

## 3.2.1 Test Unit Design Parameters

The tested column, referred to as test unit 123007, was a circular reinforced concrete column designed at half-scale with aspect ratio (length/diameter) of 12, in order to have a test series for analysis with aspect ratios 4, 6, 8, 10 and 12. The column therefore had a 24 ft effective length and 2 ft section diameter.

The column reinforcement was designed to provide the column with sufficient strength and ductility and to meet the specifications outlined in the Caltrans Seismic Design Criteria (Caltrans 2010). Longitudinal reinforcement consisted of 18 number 8 (1 in. diameter) steel bars with a 1 inch concrete cover, resulting in a longitudinal reinforcement ratio ( $\rho_I$ ) of 3% of the cross-sectional area. Confinement was provided with transverse steel reinforcement in the form of a

continuous number 4 (0.5 in. diameter) spiral at 3 in. pitch spacing. This results in a transverse reinforcement ratio ( $\rho_s$ ) of 1.2% as defined in Equation 3-4.

The geometry and reinforcement layout of column 123007 is shown in Figure 3-10. As shown, the column components include a 66 in. square footing with a 19 in. depth and 42 in. wide loading block, provided to ensure an evenly applied load to the top of the column. The reinforcement extended into the footing and loading block with the longitudinal bars anchored into the footing with  $90^{\circ}$  hooks. The footing and loading block were also reinforced with longitudinal and transverse steel as well as shear resisting steel hooks.

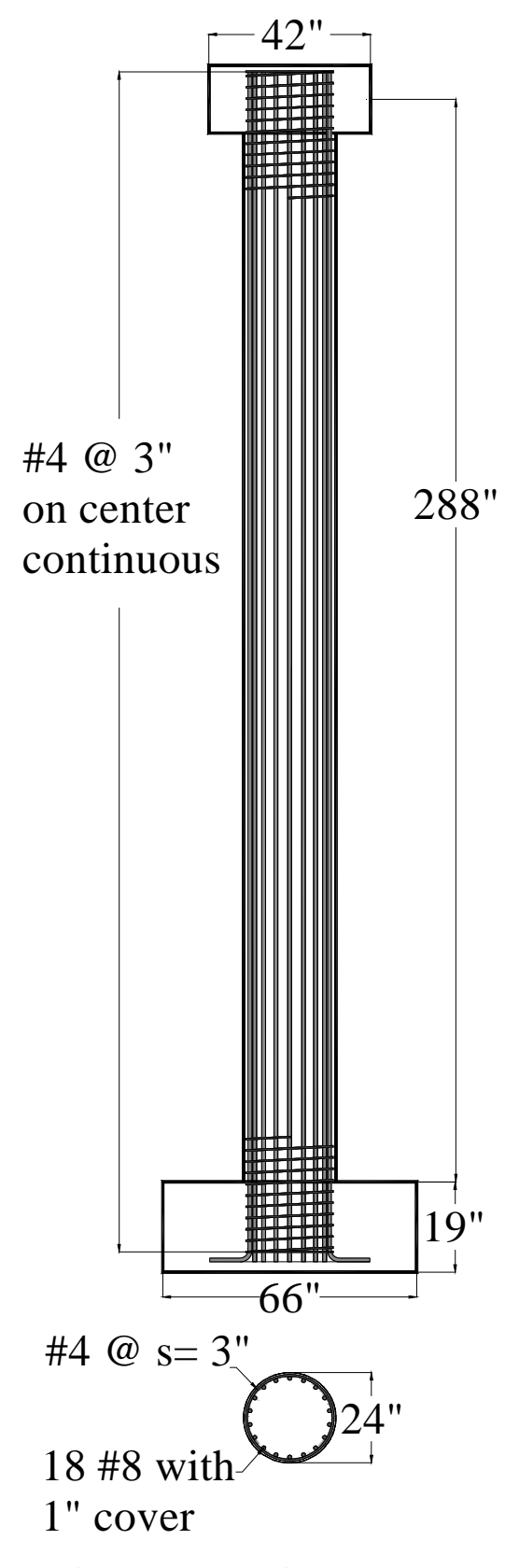


Figure 3-10: Test Column 123007 Geometry and Reinforcement

### 3.2.2 Material Properties

The column was designed using normal weight concrete and grade 60 reinforcing steel for both the longitudinal and transverse directions. Material testing was completed prior to testing to determine the properties of all materials, which are summarized in Table 3-4. The material strengths were taken as the average of three samples for each material.

**Table 3-4: Material Properties Day of Testing** 

Material	Strength (ksi)	
Materiai	Yield	Ultimate
Concrete	6.5	4.6
Longitudinal Steel	70.5	107.2
Transverse Steel	66	100.4

### 3.2.3 Instrumentation

Instrumentation was provided to obtain data in the form of steel strains, curvature, lateral deformations and shear deformations. Strain gauges were provided on the extreme longitudinal bars as well as generator and follower sides of the spiral at several planes along the column length. Lateral deformations along the column height were measured with displacement transducers. The flexure-induced curvatures of several segments along the column height were calculated from deformation measurements along the generator sides of the column. Shear deformations were calculated from instrumentation panels that arranged five displacement transducers to measure deformations along the sides and diagonal of a rectangle. Three shear deformation panels were mounted over the first 30 in. of the column and on one side. The instrumentation setup is shown in Figure 3-11.

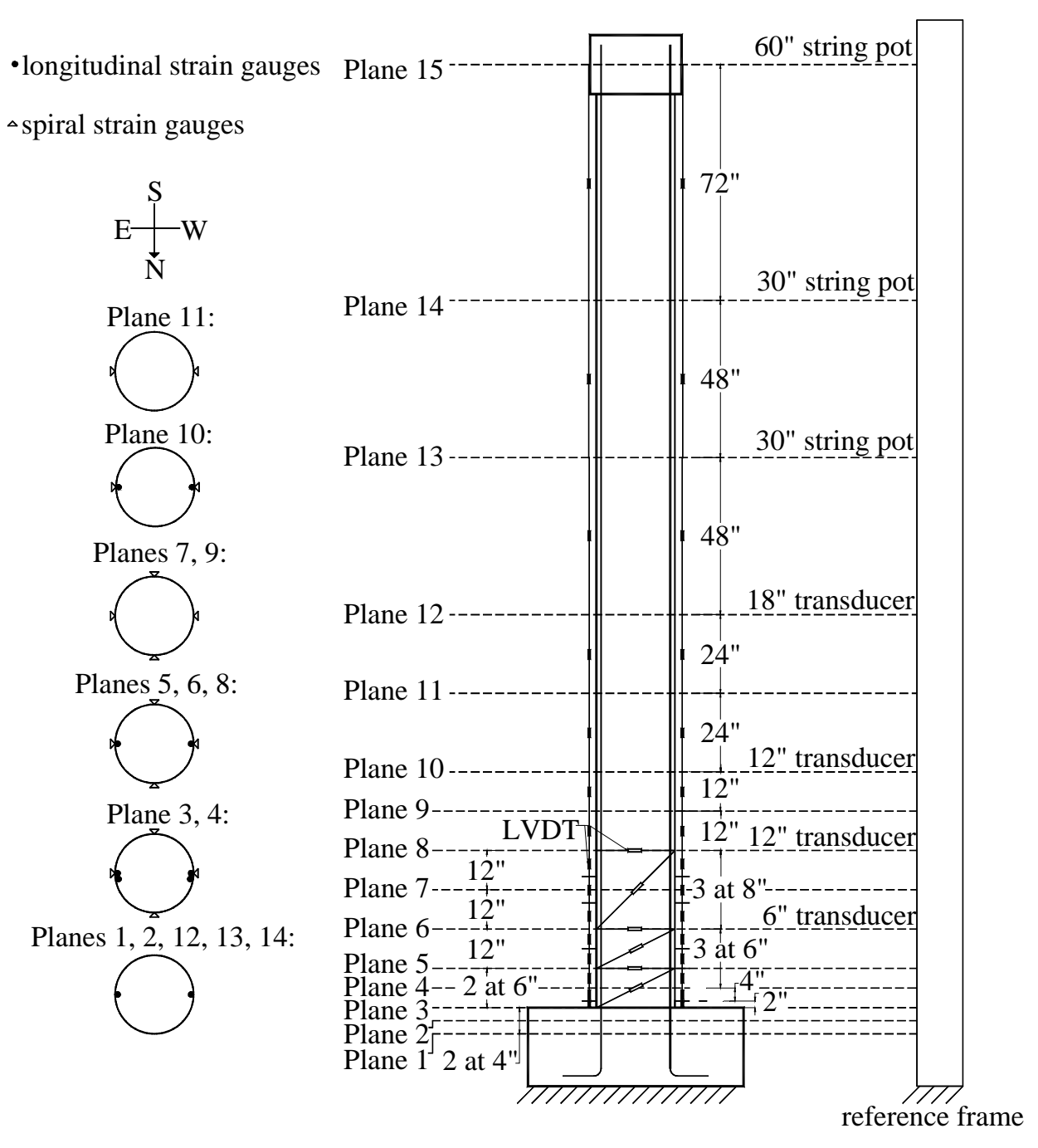


**Figure 3-11: Instrumentation Setup** 

#### 3.2.3.1 Strain Measurement

Strains were measured with electrical resistance quarter-bridge strain gauges with 120 ohm resistance and a 5 mm gauge length. Strain gauges were placed at key locations (planes) on the longitudinal reinforcing bars as well as the spiral in the follower and generator sides, as indicated in Figure 3-11.

### 3.2.3.2 Curvature Calculation

Flexure curvature along the column height were calculated from the extension and shortening deformations measured with displacement transducers placed at multiple heights along the column generator sides, as shown in Figure 3-11. The displacement transducers were mounted on aluminum brackets mounted on threaded bars anchored in the confined concrete region of the column. The displacement transducers were mounted on the supporting brackets so as to measure deformations in the vertical direction (parallel to the column axis). The mounting brackets served the purpose of both securing the transducers as well as a target surfaces for the instrument immediately above. This setup can be seen in Figure 3-12. The instrument displacement readings,  $\delta$ , were converted to strain by the following equation:

$$\varepsilon_{E,W} = \frac{\delta_{E,W}}{L_g}$$
 3-12

where the subscript, E or W denotes the East or West face of the column in which the instrument is located and  $L_g$  is the gauge length between instruments (i.e., segment length). Curvature at the middle of each segment was then calculated by:

$$\varphi = \frac{\varepsilon_W - \varepsilon_E}{dist_i}$$
 3-13

where  $dist_i$  is the distance between the East and West instruments. Displacement in the column due to flexure was calculated by integrating the curvatures along the column height, which due to the discrete measurement points simplifies to:

$$\Delta F = \sum_{i} \varphi_{i} L_{gi} h_{i}$$
 3-14

where  $h_i$  is the distance of the centroid of each curvature measurement segment from the top of the column, as shown in Figure 3-13.



**Figure 3-12: Curvature Instrumentation** 

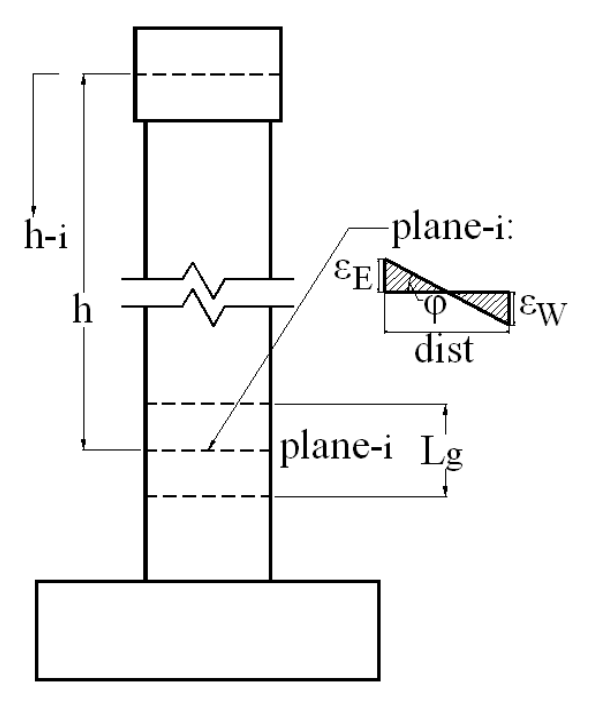


Figure 3-13: Schematic of Displacement due to Curvature

# 3.2.3.3 Shear Measurement

Shear deformations along the plastic hinge region in the column were calculated from the measurements of three rectangular deformation panels that consisted of an arrangement of displacement transducers along the four sides and one diagonal of a rectangle. The panels were placed on the North face of the column over the first 36 in., as shown in Figure 3-14a. The shear deformation panel sides and diagonal was realized by using a pair of aluminum tubes that slide one inside the other with a displacement transducer attached to one end and a rigid target attached to the other (Figure 3-14b). Aluminum rods protruding from the column concrete were used to attach frictionless swiveling rod connectors to the aluminum tubes. Pictures of the shear instrumentation panel are shown.



(a) Shear Panels



(b) View of Instrument and Frictionless Connections

**Figure 3-14: Shear Instrumentation** 

60

Lateral column deformations due to shear were calculated according to the methods proposed by Lehman et al. in the PEER research report on well-confined columns (Lehman and Moehle 2000). The true diagonal displacement due to shear ( $\Delta D$ ) was taken as the measured diagonal displacement ( $\Delta D_d$ ) with the subtraction of the vertical and horizontal movement of the panels ( $\Delta D_{vh}$ ):

$$\Delta D = \Delta D_d - \Delta D_{vh}$$
 3-15

Where: 
$$\Delta D_{vh} = \sqrt{(b + \Delta_h)^2 + (v + \Delta_v)^2} - d$$
 3-16

with specific variables according the schematic in Figure 3-15. The resulting shear strain,  $\gamma$ , in the column is then:

$$\gamma = \frac{\sqrt{\left(d + \Delta D_d\right)^2 - \left(v + \Delta_v\right)^2 - \left(b + \Delta_h\right)}}{h + \Delta_v}$$
3-17

The preceding equations give the shear deformation within each panel. Using these values, the total horizontal displacement in the column due to shear deformation is:

$$\Delta S = \sum_{i} \gamma_i h_i$$
 3-18

The shear deformation above the upper-most panel was assumed constant, as shown in Figure 3-16.

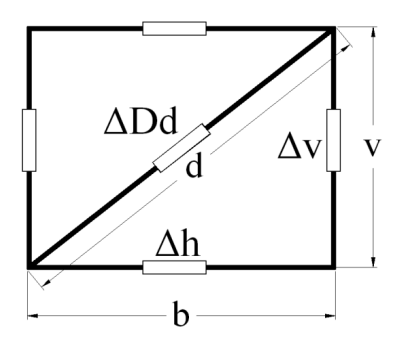


Figure 3-15: Shear Panel Configuration

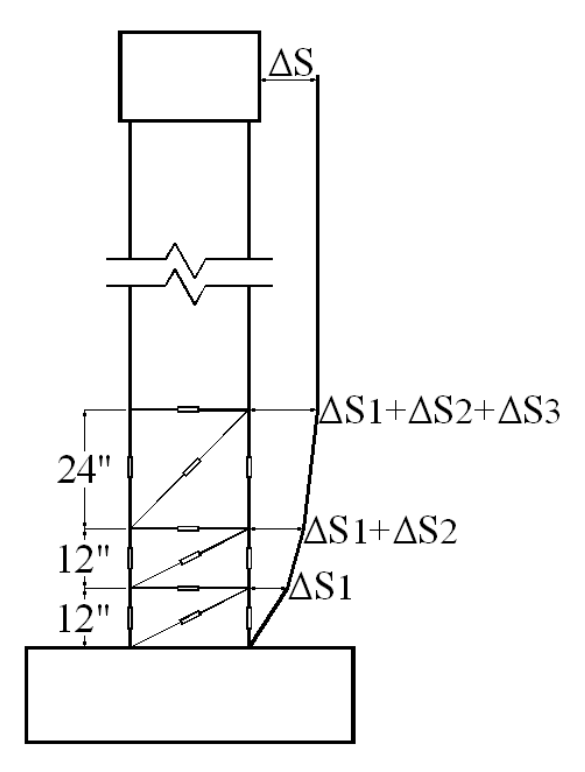


Figure 3-16: Schematic of Displacement Due to Shear

# **3.2.3.4** Lateral Displacement Measurement

In order to measure the horizontal displacement of the column at intermediate heights, displacement transducers were placed at seven locations along the column length, as shown in Figure 3-11. Since the column does not deform linearly, displacement profiles show the curvature of the overall test unit. Displacement transducers were secured to a reference frame and extended to a target near the West face of the column as shown in Figure 3-17.



(a) Displacement Transducers on Reference Frame



(b) Target for Horizontal Measurement

**Figure 3-17: Horizontal Measurement** 

63

#### 3.2.4 Loading

A constant axial load was applied to top of the column by means of external post-tensioning. The axial load fixture used a spandrel beam at the top of the column load block and two G150 1-3/8 in. threadbars that were anchored in the laboratory strong floor, extended through an opening in the column footing and then trough hollow-core jacks. Axial load to the column was applied as the external rods were tensioned with the use of the hydraulic jacks and the spandrel beam reacted against the column load block thus imposing the compressive force to the test unit. The applied axial load of 158 kips corresponds to 7% of the nominal crushing capacity ( $f_cA_g$ ) with  $f_c$  taken as the specified or design concrete compressive strength of 5 ksi, and corresponds to 5.4% of  $f_cA_g$  when  $f_c$  is the actual compressive strength of 6.5 ksi. The axial load was chosen to represent an average load applied by a bridge superstructure to a single column bridge bent (Lehman and Moehle 2000).

Lateral loading was applied to the top of the column by means of a servo-controlled hydraulic actuator connected to the column loading block as shown in Figure 3-18. Lateral loads were applied in a reverse cyclic pattern with increasing demands at pre-defined load and deformation levels. Load levels were determined in increments of expected yield values. A theoretical yield force was determined from a sectional analysis by the following:

$$F'_{y} = \frac{M'_{y}}{L}$$
 3-19

Load was applied in force control up to the theoretical yield force value in quarter increments and in a cyclic form. The ideal yield displacement was determined from the measured displacement at theoretical yield according to the relation:

$$\Delta_y = \frac{M_y}{M'_y} \Delta'_y$$
 3-20

The ideal yield displacement defines displacement ductility ( $\mu\Delta$ ) 1. The remaining load levels were applied in displacement control in increasing levels of displacement ductility:

$$\mu_{\Delta} = \frac{\Delta m}{\Delta_{V}}$$
 3-21

where  $\Delta_m$  is the target displacement and  $\Delta_y$  is the calculated yield displacement. During testing, the displacement at theoretical yield force of 1.0 F'y was larger than the expected  $\Delta'_y$  and was closer to the estimated value of  $\Delta_y$ . The larger measured displacement is attributed to second-order, or P-delta, effects, which were not considered in the predictive analyses. Research by Silva et al. (2012) has shown that P-delta effects to not significantly change the ideal yield displacement. Thus, it was decided to use the calculated ideal yield displacement from analyses without P-delta effects as the displacements for ductility 1.. The resulting load history of the test is shown in Figure 3-19. One cycle was applied at each pre-yield load level:  $0.25F'_y$ ,  $0.5F'_y$ ,  $0.75F'_y$ ; and three cycles were applied at each post-yield load level:  $1\Delta_y$ ,  $1.5\Delta_y$ ,  $2\Delta_y$ ,  $3\Delta_y$ . The displacement at ductility 3 was estimated to be 20 inches, which is the limit of the actuator, and therefore the last loading level applied. The target force and displacement values (at first cycle) are summarized in Table 3-5.

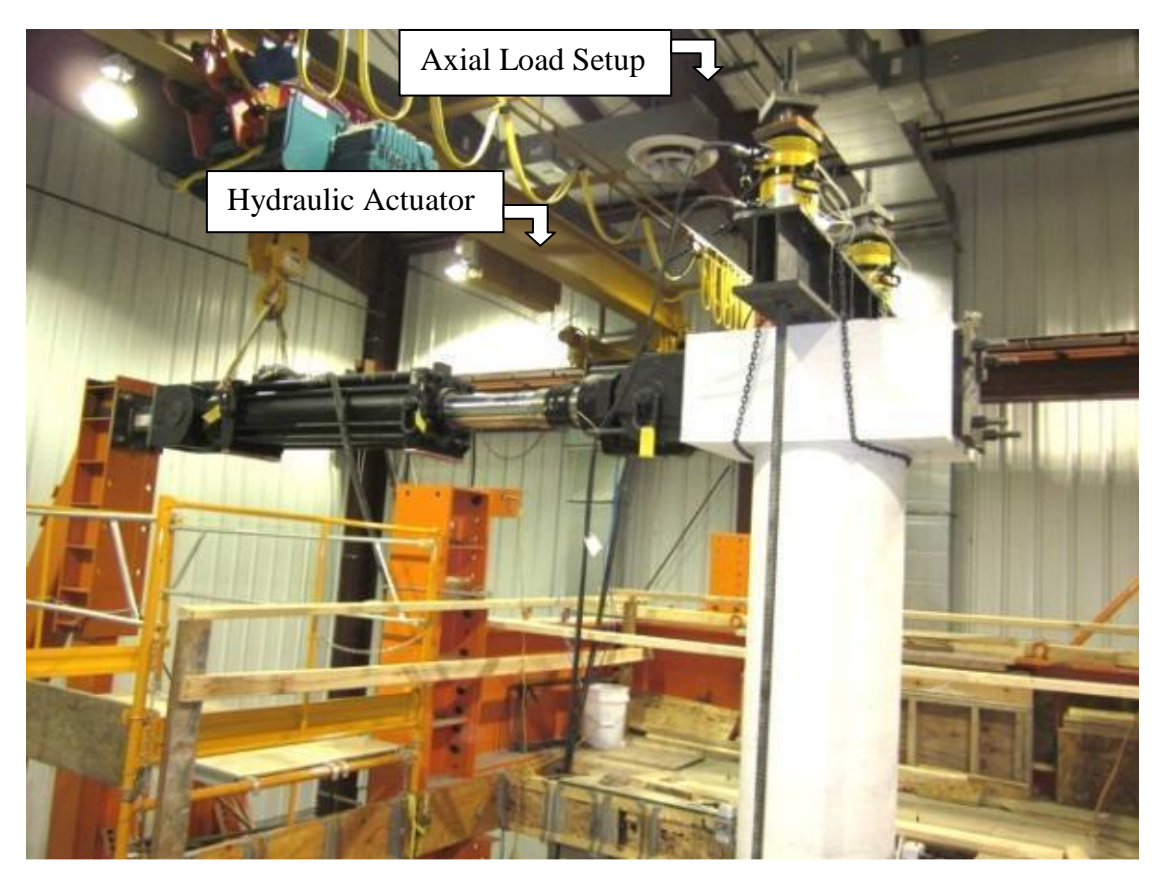


Figure 3-18: Loading Setup

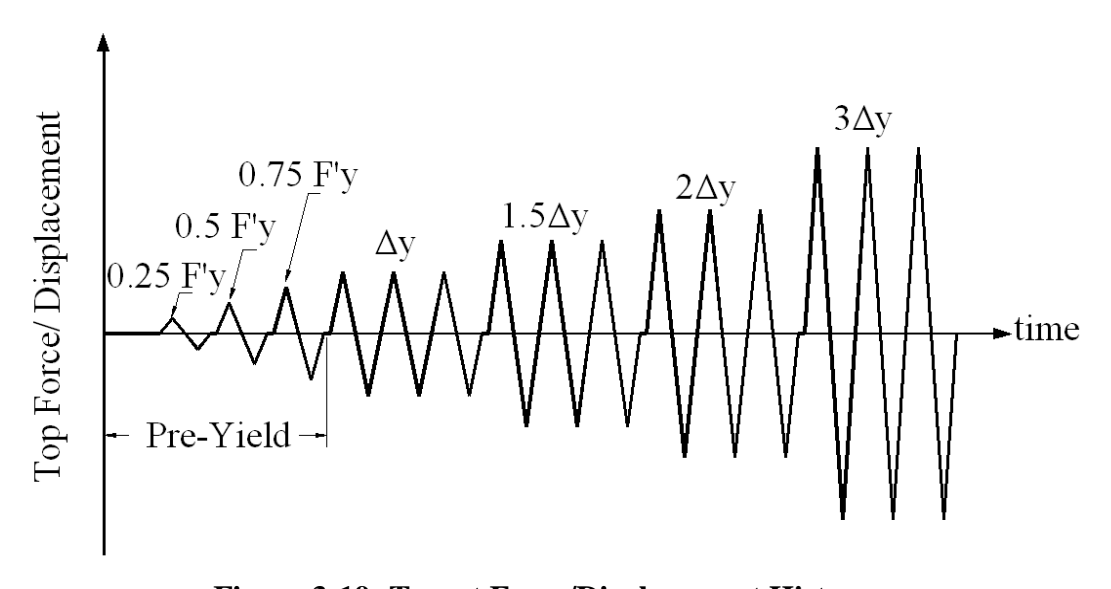


Figure 3-19: Target Force/Displacement History

**Table 3-5: Target Load and Displacement Levels** 

	Force (kip)	Disp. (in)
0.25 E	6.7	0.96
0.25 F' <sub>y</sub>	-6.7	-0.98
0.5.5!	13.3	2.6
0.5 F' <sub>y</sub>	-13.3	-2.8
0.75 F' <sub>y</sub>	20	4.6
	-20	-4.8
_	26.7	6.81
$\mu_{\Delta}=1$	-26.7	-6.81
	30.9	10.2
$\mu_{\Delta}=1.5$	-30.8	-10.2
$\mu_{\Delta}=2$	32	13.6
	-31.5	-13.6
$\mu_{\Delta}=3$	33	20
	-33.1	-20

### 3.2.5 Test Setup

The overall testing setup consisted of the test unit components and test fixtures as shown in Figure 3-20. The test unit included the main column segment, its footing and a loading block. The unit was secured by post-tensioning the footing to the laboratory strong floor with six high-strength threadbars. Two additional threadbars were used for the axial load setup. These rods were anchored in the strong floor but continued through tapered slots in the footing (to allow horizontal movement as the column deformed) and continued past the spandrel beam (which sat on top of the column load stub) and then trough hollow-core jacks. The test fixtures included the reference frame for instrumentation and the loading fixtures. The hydraulic actuator was anchored to a steel reaction frame atop reinforced concrete support blocks. These fixtures were also secured by post-tensioning the frame and support blocks to the floor with threadbars. The constructed test setup components are shown in Figure 3-21.

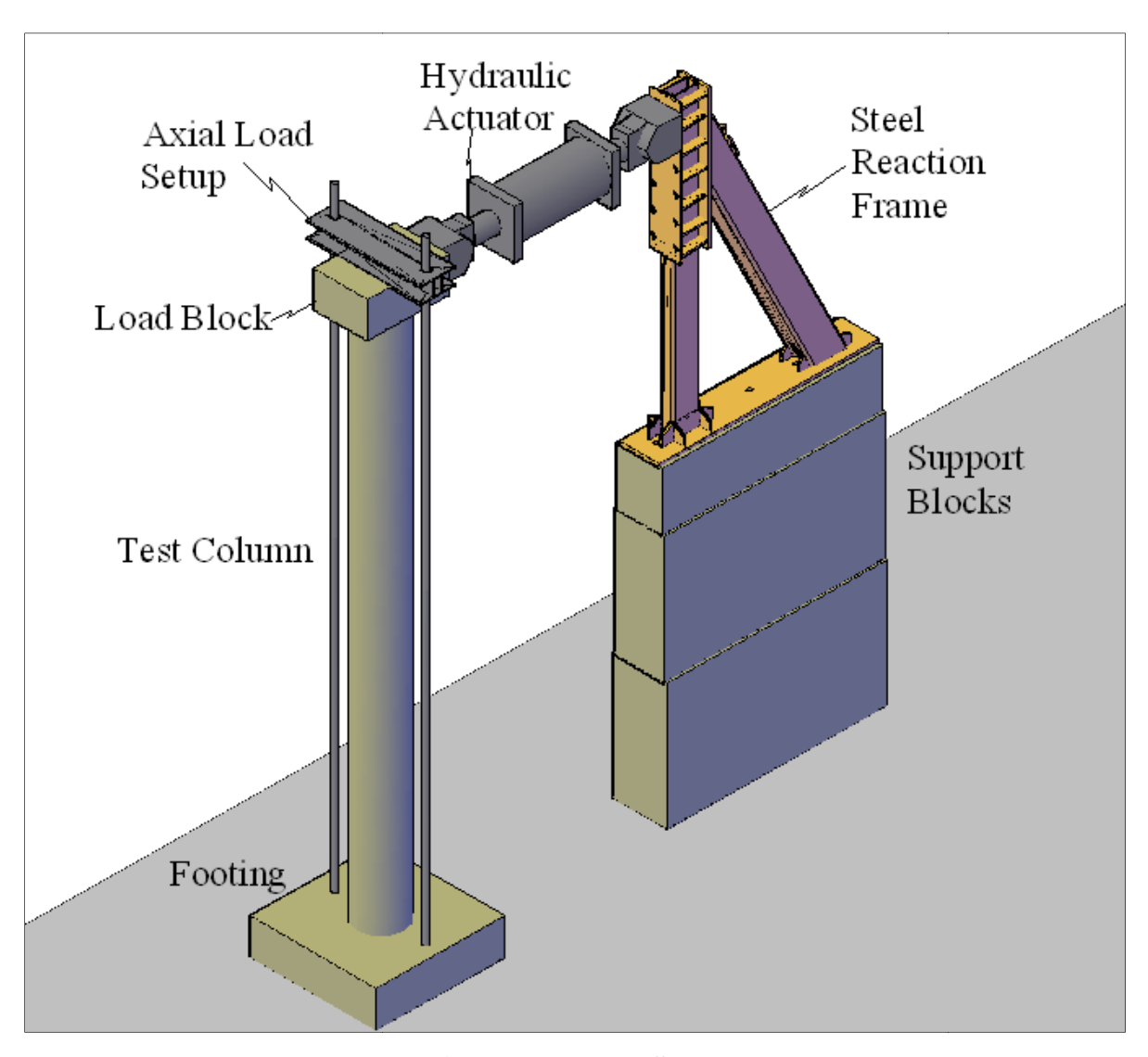


Figure 3-20: Test Setup



Figure 3-21: Test Setup Components

### 3.2.6 Observations

# **3.2.6.1** Cracking

The first level of loading did not show any signs of damage. Cracking initiated at the second load level (0.5F'<sub>y</sub>). At this cycle, cracks were spaced about 6 in. apart. Crack widths were approximately 0.004 in. and extended to a height of 12 ft. In the next load level (0.75 F'<sub>y</sub>) crack spacing decreased to 3 in., matching the pitch of the steel spiral within. Cracks continued to grow in length and width in subsequent loading cycles, with maximum crack widths of 0.011 in. at

 $\mu\Delta=1$  and 0.25 in. at the end of testing ( $\mu\Delta=3$ ). Cracks began to cross the neutral axis of the column at  $\mu\Delta=2$ , indicating initial shear effects. This extension of crack length through the neutral axis continued in subsequent cycles and reached an extent of 12 ft along the column length by the end of testing. The crack pattern is shown in Figure 3-22. The majority of new cracks propagated along the length of the column between loading cycles 0.5F'y and  $\mu\Delta=1$ , although cracking continued to extend until  $\mu\Delta=3$ . By the end of testing, cracking had reached a maximum height of 21 ft.



Figure 3-22: Column Cracking Pattern at  $\mu_{\Delta}{=}3$ 

Cracks in the footing, indicating strain penetration effects were observed at the first cycle of  $\mu\Delta=1$ . These cracks continued to grow in width and length in subsequent cycles, reaching a maximum width of 0.013 in. A small number of cracks were also observed to extending over the surface of the footing as well as through its depth.

#### 3.2.6.2 Spalling and Overall Damage

Spalling of the cover concrete initiated at  $\mu\Delta=1.5$  near the base of the column. By the end of three cycles at this load level, some exposing of the steel spirals was evident. The inside of the spiral was exposed at  $\mu\Delta=2$  on the East face of the column, which was taken as indicative of the crushing limit state. The concrete on this face however was suspected of being poorly vibrated during casting. Spalling continued to extend during subsequent cycles and reached a height of 27 in. by the end of  $\mu\Delta=3$ . Longitudinal bars became exposed during the three cycles at  $\mu\Delta=3$  as well. The final testing state at 20 in. top displacement is shown Figure 3-23, and the final damage due to spalling is shown in Figure 3-24.



Figure 3-23: Column at 20-inch Displacement  $(\mu_{\Delta}{=}3)$ 



Figure 3-24: Damage due to Spalling at end of  $\mu_{\Delta}{=}3$  (20-inch Displacement)

#### 4 EVALUATION OF PLASTIC HINGE DESIGN MODELS

This chapter describes a numerical investigation conducted to determine the effectiveness of current plastic hinge models in predicting several limit states for the implementation for PBD. Thirty-four previously tested columns were selected for this analysis based on relevance to this thesis topic and current design methods, as described below.

#### 4.1 The PEER Structural Performance Database

The Pacific Earthquake Engineering Research (PEER) Center sponsored a project to create a Structural Performance Database (SPD) in 2003, consisting of 416 reinforced concrete columns that were tested by various researchers under cyclic lateral loads (PEER 2011). This project was assembled to service the earthquake engineering research community and may be accessed online by the public. The PEER SPD contains columns of both rectangular and circular cross-section, but only circular columns were considered in this study. Information available for these columns includes column geometry, material properties, reinforcing details, test configuration, axial load level, force-displacement history of test data and references of documented tests. The database also gives specific displacement values at each of six damage states. These damage states are: spalling of the unconfined concrete, crushing of the confined concrete, buckling of longitudinal reinforcement, fracture of longitudinal reinforcement, fracture of transverse reinforcement and failure. These values were obtained from the documentation available for each test; therefore not every column has values recorded for each of the noted six damage states.

#### 4.2 Selected Columns

The PEER SPD contains 163 circular columns; therefore in order to be considered relevant to this study, columns used for analyses were selected according to specific criteria. The criteria for chosen columns are as follows:

- Column failure type must be due to flexure. Columns resulting in shear failure or shearflexure failure were eliminated.
- Columns must be of aspect ratio greater than 3. Those of aspect ratios of 3 and below were eliminated. The first criterion eliminated many, but not all, of these columns.
- Columns must be well-confined according to modern design standards. This was determined by inspecting the experimental force-displacement hysteresis pattern and eliminating those column tests showing unstable results. An example of a column eliminated due this criterion is shown in Figure 4-1.
- Lastly, columns without recorded limit state data were eliminated since they offer no comparison to the analyses performed.

#### Force-Displacement Experimental Response: Davey 1975, No. 1 50 40 30 20 Force (kip) 10 0 -10 -20 -30 -40 -50 -3 2 3 -5 -2 0 1 4 Displacement (in)

Figure 4-1: Example of Unstable Hysteresis, Resulting in Elimination from PEER Analysis

Program (PEER 2011)

The resulting 34 columns used in this study are shown in Table 4-1. The table presents information on each column's geometric properties, axial load and reinforcement properties. Properties shown include the column's aspect ratio (L/D), axial load ratio and reinforcement ratios. The axial load ratio is expressed as the percentage of load over the column's nominal crushing capacity:

Axial Load Ratio = 
$$\frac{P}{f'cAg}$$

where P is the axial force,  $f'_c$  is the concrete compressive strength and  $A_g$  is the gross cross-sectional area of the column. The longitudinal reinforcement ratio is represented by  $\rho_l$ , which is the ratio of the reinforcement cross-sectional area to  $A_g$ :

$$\rho_l = \frac{nA_b}{A_g}$$
 4-2

where n is the number of reinforcing bars, and  $A_b$  is the individual bar cross-sectional area. The effective confinement ratio of the column,  $\rho_{eff}$ , is expressed in Equation 4-3 where terms have been previously defined:

$$\rho_{eff} = \frac{\rho_S f_{yS}}{f'c}$$
 4-3

**Table 4-1: PEER SPD Columns Used for Limit State Analysis (PEER 2011)** 

Reference	Unit	Length (in)	L/D	P/f'cAg (%)	ρι	Peff	S/d <sub>b</sub>
Davey 1975	No. 2	68.9	3.5	12.07	0.0271	0.0461	3.53
Munro et al. 1976	No. 1	107.5	5.5	0.34	0.0271	0.0948	1.85
Ng et al. 1978	No. 3	36.6	3.7	33.95	0.0230	0.2173	0.83
Ang et al. 1981	No. 1	63.0	4.0	20.81	0.0256	0.0881	2.50
Stone et al. 1986	Model N6	59.1	6.0	10.49	0.0196	0.1283	2.07
Stone et al. 1989	Full Scale Flexure	359.8	6.0	6.85	0.0200	0.0826	2.07
Watson & Park 1989	No. 10	63.0	4.0	52.76	0.0192	0.0743	5.25
Kowalsky et al. 1996	FL1	143.9	8.0	29.65	0.0362	0.1176	4.79
Kowalsky et al. 1996	FL2	143.9	8.0	27.13	0.0362	0.0724	3.21
Kowalsky et al. 1996	FL3	143.9	8.0	28.11	0.0362	0.1115	4.79
Kunnath et al. 1997	A2	54.0	4.5	9.44	0.0204	0.1439	2.00
Kunnath et al. 1997	A3	54.0	4.5	9.44	0.0204	0.1439	2.00
Kunnath et al. 1997	A4	54.0	4.5	8.56	0.0204	0.1176	2.00
Kunnath et al. 1997	A5	54.0	4.5	8.56	0.0204	0.1176	2.00
Kunnath et al. 1997	A7	54.0	4.5	9.26	0.0204	0.1272	2.00
Kunnath et al. 1997	A8	54.0	4.5	9.26	0.0204	0.1272	2.00
Kunnath et al. 1997	A9	54.0	4.5	9.35	0.0204	0.1284	2.00
Kunnath et al. 1997	A10	54.0	4.5	10.14	0.0204	0.1546	2.00
Kunnath et al. 1997	A11	54.0	4.5	10.14	0.0204	0.1546	2.00
Kunnath et al. 1997	A12	54.0	4.5	10.14	0.0204	0.1546	2.00
Hose et al. 1997	SRPH1	144.1	6.0	14.82	0.0266	0.0965	2.56
Henry 1998	415p	96.0	4.0	12.04	0.0149	0.0857	2.00
Henry 1998	415s	96.0	4.0	6.02	0.0149	0.0428	4.00
Lehman et al. 1998	407	96.0	4.0	7.22	0.0075	0.1028	2.00
Lehman et al. 1998	415	96.0	4.0	7.22	0.0149	0.1028	2.00

Table 4-1 (cont'd)

Lehman et al. 1998	430	96.0	4.0	7.22	0.0302	0.1028	2.00
Lehman et al. 1998	815	192.0	8.0	7.22	0.0149	0.1028	2.00
Lehman et al. 1998	1015	240.0	10.0	7.22	0.0149	0.1028	2.00
Calderone et al. 2000	828	192.0	8.0	9.06	0.0273	0.113	1.33
Calderone et al. 2000	1028	240.0	10.0	9.06	0.0273	0.113	1.33
Kowalsky & Moyer 2001	1	96.0	5.3	4.31	0.0207	0.1427	4.01
Kowalsky & Moyer 2001	2	96.0	5.3	4.12	0.0207	0.1365	4.01
Kowalsky & Moyer 2001	3	96.0	5.3	4.44	0.0208	0.1478	4.00
Kowalsky & Moyer 2001	4	96.0	5.3	4.16	0.0208	0.1385	4.00
	Mean	105.9	5.4	12.37	0.0221	0.1157	2.59
Statistics	Stand. Dev.	69.8	1.8	10.54	0.0063	0.0339	1.11
	Coef. Var.	0.7	0.3	0.85	0.2873	0.2931	0.43
	Minimum	36.6	3.5	0.34	0.0075	0.0428	0.83
	Maximum	359.8	10.0	52.76	0.0362	0.2173	5.25

#### 4.3 OpenSees Model

In order to predict global and intermediate behavior of the columns listed in Table 4-1, a pushover (i.e., monotonic) analysis was performed on each using the lumped plasticity element in OpenSees. Although tests were performed under cyclic loading, a pushover analysis was used to capture the monotonic envelope of these tests and more efficiently estimate intermediate limit states. Four analyses were performed on each column to compare the accuracy in which the different common plastic hinge length models described in Section 2.3.1 predict inelastic behavior at several limit states. A summary of the four plastic hinge length expressions implemented in these analyses is given in Table 4-2.

**Table 4-2: Plastic Hinge Expressions Used in OpenSees Analysis** 

Reference	Plastic Hinge Expression					
Priestley et al. 2007	$L_p = kL + 0.15d_b f_y \ge 0.3d_b f_y \text{ (ksi)}$ $where \ k = 0.2 \left( \frac{f_u}{f_y} - 1 \right) \le 0.08$					
Berry et al. 2008	$L_p = 0.0375L + 0.01f_y \frac{d_b}{\sqrt{f_c'}} (psi)$					
Bae & Bayrak 2008	$L_p = L\left(0.3\frac{P}{P_0} + 3\frac{A_S}{A_g} - 0.1\right) + 0.25h + L_{Sp} \ge 0.25h$					
Corley 1966	$L_p = 0.5D$					

In order to implement the lumped plasticity element to each of the PEER SPD columns, a sectional analysis was first performed to obtain the moment-curvature data for each column. The sectional analyses were performed on fiber sections featuring the OpenSees material models described in Section 3.1.1.3. The sections were typically discretized into 10 transverse divisions in the core concrete, 5 transverse division in the cover concrete, and 20 radial divisions within

both, as shown in Figure 4-2. The number of fiber divisions however varied slightly for some columns in order to achieve convergence. Each intersection of these fiber divisions are monitored for sectional behavior during the analysis. Moment-curvature behavior obtained from these analyses was used to estimate yield and ultimate displacement values to use as targets for the element analysis, as well as the effective stiffness. The lumped plasticity element was then assigned the fiber section within the plastic hinge length. The elastic portion was defined by the effective stiffness (see Figure 2-4a) obtained from the sectional analysis and the column's geometric properties.

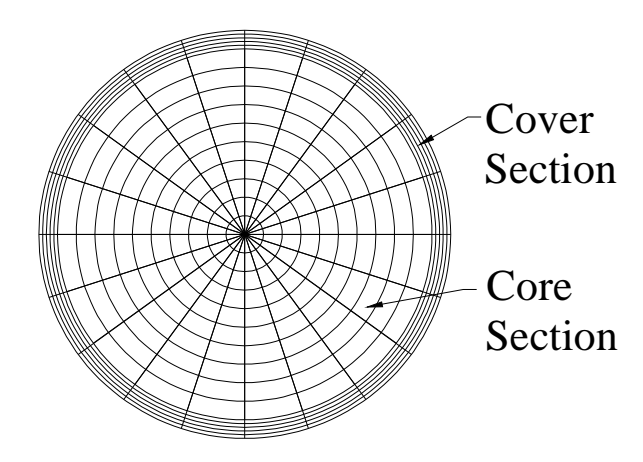


Figure 4-2: Typical Discretized Fiber Column Section

#### **4.3.1** Analytical Target Displacements

Pushover analyses were performed using a displacement control integrator, using yield and ultimate values as target displacements. Yield and ultimate displacement were calculated from parameters found from the sectional analysis of each column, using the expressions discussed in Section 2.3, specifically Equations 2-2 through 2-4. Analyses were completed first until yield, then to ultimate or failure conditions.

Experimental yield displacement was not given in the PEER SPD and therefore a calculated estimate was required. While experimental values for ultimate displacement are available in the SPD, these values were not used in the analysis as the target ultimate displacement. Given that the purpose of this research was to find the error between estimated and actual limit state behavior, it was of interest to find the difference in predicted ultimate displacement to that which would occur in the simulated seismic event. In order for PBD to be implemented, the methods presented here would be used without any experimental data available; therefore it was assumed that ultimate behavior was a limit state to be used for comparisons.

#### 4.4 Analysis Results

In order to determine how well each of the four plastic hinge models perform compared to experimental data, the displacement at which each of the six damage states listed in the SPD occurs was estimated from the pushover analysis performed. Statistics were obtained to determine the error to which each of the plastic hinge models predicted each limit state. In order to compare the displacement at each limit state, data was evaluated as a percentage of the column length, which is known as drift. This offers dimensionless data in order to avoid misleading results. The experimental drift of each column used in this analysis is shown in Table 4-3.

**Table 4-3: Limit State Results from Experimental Data (PEER 2011)** 

Reference	Unit	L/D	Δcc/L (%)	Δbb/L (%)	Δfract/L (%)	Δult/L (%)
Davey 1975	No. 2	3.5	3.49	4.69		4.69
Munro et al. 1976	No. 1	5.5	1.39	-	-	-
Ng et al. 1978	No. 3	3.7	1.08	-	-	-
Ang et al. 1981	No. 1	4.0	0.94	3.75	3.75	3.75
Stone et al. 1986	Model N6	6.0	2.24	4.77	6.72	4.48
Stone et al. 1989	Full Scale Flexure	6.0	1.96	5.89	5.89	5.89
Watson & Park 1989	No. 10	4.0	-	-	-	1.97
Kowalsky et al. 1996	FL1	8.0	-	9.08	9.08	9.08
Kowalsky et al. 1996	FL2	8.0	1.91	5.74	-	5.74
Kowalsky et al. 1996	FL3	8.0	1.86	9.30	9.30	9.30
Kunnath et al. 1997	A2	4.5	-	4.70	-	4.98
Kunnath et al. 1997	A3	4.5	19.70	-	-	-
Kunnath et al. 1997	A4	4.5	-	-	-	4.15
Kunnath et al. 1997	A5	4.5	-	-	5.47	5.47
Kunnath et al. 1997	A7	4.5	1.46	5.83	-	5.83
Kunnath et al. 1997	A8	4.5	2.33	5.83	-	5.83
Kunnath et al. 1997	A9	4.5	-	4.59	-	4.59
Kunnath et al. 1997	A10	4.5	2.33	6.61	-	5.98
Kunnath et al. 1997	A11	4.5	3.64	-	7.65	7.65
Kunnath et al. 1997	A12	4.5	3.64	5.90	-	5.90
Hose et al. 1997	SRPH1	6.0	1.64	8.74	8.74	8.74
Henry 1998	415p	4.0	-	5.21	5.54	5.21
Henry 1998	415s	4.0	-	5.21	-	5.21
Lehman et al. 1998	407	4.0	1.56	5.21	5.21	5.21
Lehman et al. 1998	415	4.0	1.56	5.29	7.30	5.54

Table 4-3 (cont'd)

Lehman et al. 1998	430	4.0	1.56	7.30	-	7.30
Lehman et al. 1998	815	8.0	2.73	9.12	9.12	9.12
Lehman et al. 1998	1015	10.0	3.13	10.42	10.42	10.42
Calderone et al. 2000	828	8.0	3.65	12.30	-	12.30
Calderone et al. 2000	1028	10.0	4.17	14.58	-	14.58
Kowalsky & Moyer 2001	1	5.3	1	6.15	7.66	6.15
Kowalsky & Moyer 2001	2	5.3	-	10.73	12.29	10.73
Kowalsky & Moyer 2001	3	5.3	3.02	10.74	-	10.74
Kowalsky & Moyer 2001	4	5.3	3.02	13.75	-	13.75
	Mean	5.4	3.08	7.46	7.61	7.11
Statistics	Stand. Dev.	1.8	3.66	3.00	2.26	3.03
	Coef. Var.	0.3	1.19	0.40	0.30	0.43
	Minimum	3.5	0.94	3.75	3.75	1.97
	Maximum	10.0	19.70	14.58	12.29	14.58

#### 4.4.1 Limit State Analysis

In order to estimate the displacement at each damage state, a definition of each was required. Experimental data for each limit state in the PEER SPD is based on observation during testing, therefore in order to compare to a numerical study, damage states were defined based on the strain at which the onset of the damage is expected to occur. The first occurrence of this strain was then found within the analysis data and the corresponding displacement was used to compare to the experimental data. The definition assumed for each of the compared limit states is described in the subsequent sections, followed by the performance of the analysis models in predicting them.

#### **4.4.1.1** Unconfined Concrete Spalling

Concrete spalling is the action of the unconfined cover concrete cracking and breaking off from the column. Within the PEER SPD the data listed is for "significant spalling" which indicates not the onset of the action, but rather once a large portion of the plastic hinge region has experienced loss of concrete cover. What is considered to be "significant" is largely dependent on the opinion of the researcher conducting each experiment; therefore the limit state varies with individual perception. This limit state is very ill defined among the research community and a large error in analytical comparison is expected.

For this study, significant spalling was defined at the instant when the unconfined concrete reaches a strain of 0.005. It was assumed that unconfined concrete typically begins to spall at a strain of about 0.002; therefore, a strain of 0.005 would indicate significant spalling. The

displacement at which the extreme compression fiber in the concrete cover reached a strain of 0.005 was therefore taken as the limit state for significant spalling.

The experimental versus predicted drift at the significant spalling limit state is compared for each of the four plastic hinge models in Figure 4-3. Data points are differentiated based on aspect ratio to view any effect that slenderness may have on the trend. The least squares value is also given for the trend-line of the data points. These may be compared to the "y=x" line, which indicates a prediction equal to the experimental data. As shown in Figure 4-3, none of the plastic hinge models appear capable of capturing this limit state. The data shows an almost constant trend, indicating that spalling is predicted at about the same drift level regardless of other parameters. Significant spalling was assumed to occur at a specific strain value, which is why the analytical displacement for this damage state does not vary much between columns. The experimental definition of significant spalling, however, varies greatly. It is therefore concluded that the spalling limit state is not well-defined, either in observation or numerical definition, causing its prediction for PBD extremely difficult.

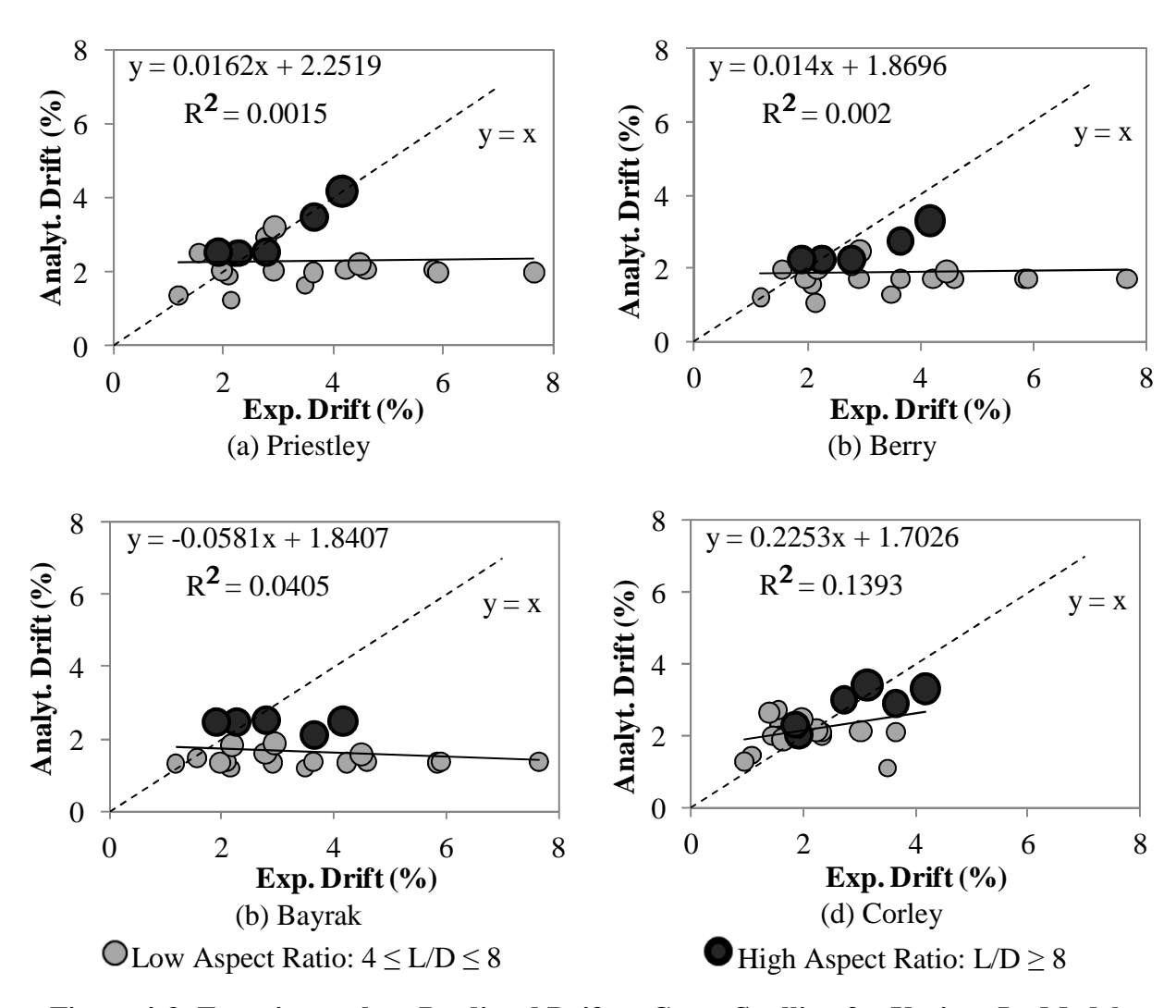


Figure 4-3: Experimental vs. Predicted Drift at Cover Spalling for Various  $\boldsymbol{L_p}$  Models

# 4.4.1.2 Confined Core Crushing

Concrete crushing is the point at which the core of the column cracks and breaks apart due to high compressive inelastic strains. Most researchers take this damage state to be the point when the inside of the steel spiral is exposed (Lehman et al. 2004). This definition however may vary between researchers which, like for the spalling limit state, may lead to high error when comparing to analytical or numerical estimates.

In this study, crushing was defined as the instant when the extreme compression fiber in the core concrete reaches the maximum compressive strain as defined by the Chang and Mander concrete model described in Section 3.1.1.3 (Chang and Mander 1994). The crushing strain is therefore computed with Equation 3-5 and the displacement at which this strain is first reached in the analytical data is considered the crushing limit state.

The experimental versus predicted drift at the crushing limit state is compared in Figure 4-4 for each of the four considered plastic hinge models. While slightly more accurate than the spalling limit state predictions, crushing prediction appears very random, with increasing scatter at large drift values. The Priestley and Berry plastic hinge models show slightly more success than the Bayrak or Corley models, however not to a significant amount. Given the complexity of concrete as a material, it is natural that defining limit states and predicting these numerically is difficult. Like spalling, the comparison of observed and predicted crushing displacements indicates a needed improvement before these methods may be implemented in PBD.

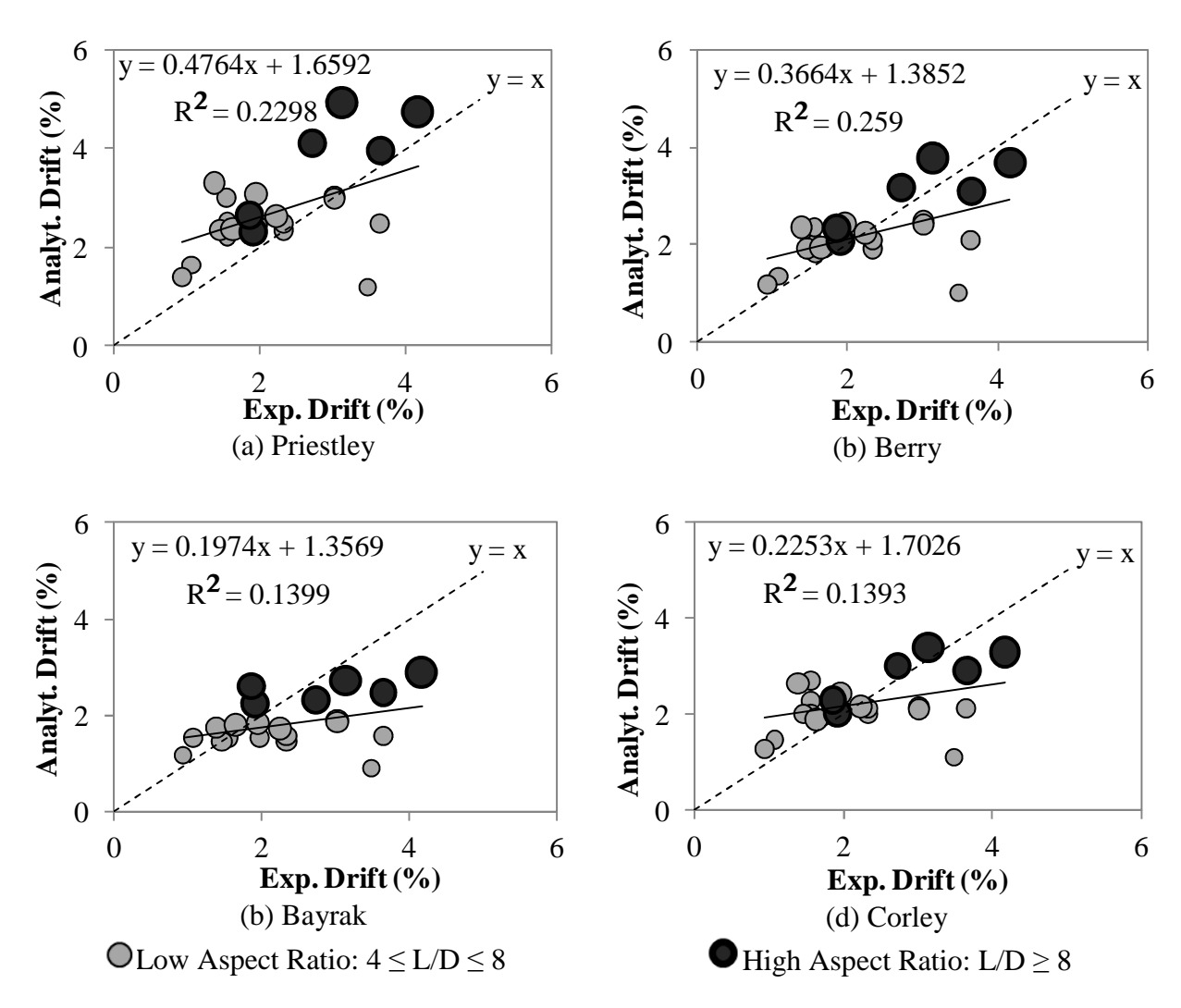


Figure 4-4: Experimental vs. Predicted Drift at Core Crushing for Various  $\mathbf{L}_{\mathbf{p}}$  Models

# 4.4.1.3 Longitudinal Bar Buckling

Buckling of the main reinforcement occurs at high strain levels when the steel bars have yielded (and elongated) in tension and become unstable when forced to recover their original length upon reloading under compression. This behavior is much less open for interpretation as damage effecting concrete limit states since steel buckling is simpler to observe in an experimental setting, and occurs at similar strain levels.

As previously discussed, buckling behavior is dependent on the cyclic loading path of the column since strains accumulate over time and the onset of buckling (under compressive stress) depends on the strain level experienced in the prior tensile demand. In a monotonic analysis, such as those performed in this portion of the study, strains will accumulate in a different manner since the bar does not switch between tension and compression. Therefore the instant at which a bar buckles may occur at a lower displacement in a cyclic analysis. Such analyses are presented in Chapter 5 of this thesis, where the discussion of this limit state is revisited. For the purposes of the statistical analysis, however, using a monotonic analysis to compare buckling displacement has been determined sufficient.

The strain at which longitudinal bar buckling was defined in this study is shown in Equation 4-4. This expression was proposed by Berry et al. in their publication proposing the plastic hinge expression used in these studies (Berry et al. 2008). The researchers found that the onset of bar buckling was best predicted as a function of the effective confinement ratio,  $\rho_{eff}$ . The constants,  $X_1$  and  $X_2$  in Equation 4-4 were calibrated using experimental data from several test columns from the PEER SPD. Berry et al. proposed various values for the constants for different plastic hinge models used in an analysis. The purpose of using different constants in each case is to account for the error in predicting buckling by each  $L_p$  expression, similar to the error which is being analyzed in this thesis. Reducing the error in the prediction by different  $L_p$  expressions would defeat the purpose of this study, and the constants calibrated by Berry et al. do not include each of the plastic hinge models being compared. The same constants were therefore used for each of the analysis cases discussed herein. Since the  $L_p$  expression proposed by Berry et al. was

also calibrated on error from the same column tests, the constants proposed for their model are used for all analyses (i.e., for all the Lp models).

$$\varepsilon_{bb} = X_1 + X_2 \rho_{eff}$$
 4-4

where  $X_1 = 0.050$  and  $X_2 = 0.224$ 

The experimental versus predicted drift at bar buckling are compared in Figure 4-5 for each plastic hinge model. Compared to the concrete damage states, buckling prediction data have far less scatter. However, the plastic hinge models used also show significant differences in their ability to predict this limit state. The Priestley and Berry models predict the limit state relatively well, with the Priestley model showing the least amount of error. The Priestley model also shows a convergence with the experimental data at higher drift ratios, while the Berry model shows a divergence as drift levels increase. Both the Bayrak and Corley plastic hinge models show a more constant trend, which fails to predict this limit state, especially at higher drift levels. A possible explanation for the models' abilities is the fact that the Priestley and Berry models were calibrated with large sets of data and aim to capture deformations based on moment gradient and strain penetration. The Corley model does not include any steel parameters, which may lead to its poor prediction of buckling behavior. While the Bayrak model was analyzed using a strain penetration component, the model was calibrated with a smaller data set and focused on high axial loads, rather than behavior of steel.

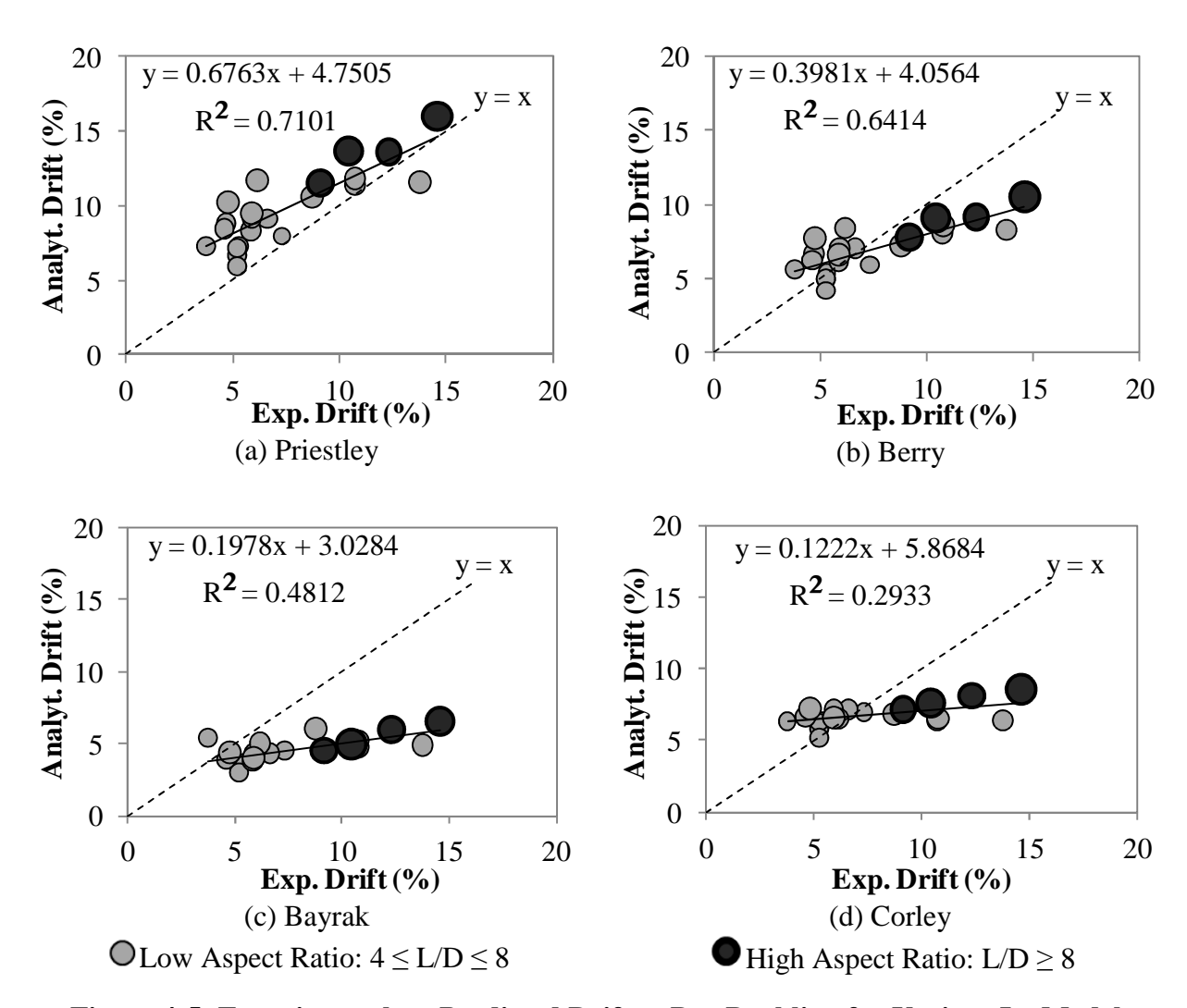


Figure 4-5: Experimental vs. Predicted Drift at Bar Buckling for Various  $L_{\mathbf{p}}$  Models

#### 4.4.1.4 Longitudinal Bar Fracture

Fracture of the main reinforcement occurs at very high tensile strains and typically occurs due to low-cyclic fatigue in the steel. Like bar buckling, cyclic loading may cause these strains to accumulate more quickly.

In this study, longitudinal bar fracture was defined as the point when the tensile strain in the extreme fiber reaches 0.1. It is well confirmed that steel fractures at a strain between 0.1-0.15

(Priestley et al. 1996), therefore the lower limit was used. Since fracture would also typically indicate failure of a column, a steel strain of 0.1 is also used as one of the three failure criteria in the analyses.

The experimental versus predicted drift at fracture is shown in Figure 4-6 for each plastic hinge model. Few columns in the database were noted to have experienced this damage state, therefore data points are limited. Similar to the buckling limit state, the Priestley and Berry models indicate better prediction of fracture than the Bayrak or Corley models. The trends however are slightly different. While the Priestley model shows a 1:1 slope, it consistently overestimates the actual drift value. The Berry model on the other hand shows slightly more success with data points falling within a smaller range of error with the experimental values. The Bayrak and Corley models again perform poorly with prediction of the fracture limit state. The Bayrak model consistently underestimates the fracture drift and diverges as drift values become larger. The Corley model shows a more constant trend, which is likely due to the simplicity of the model, having just one term in the plastic hinge expression.

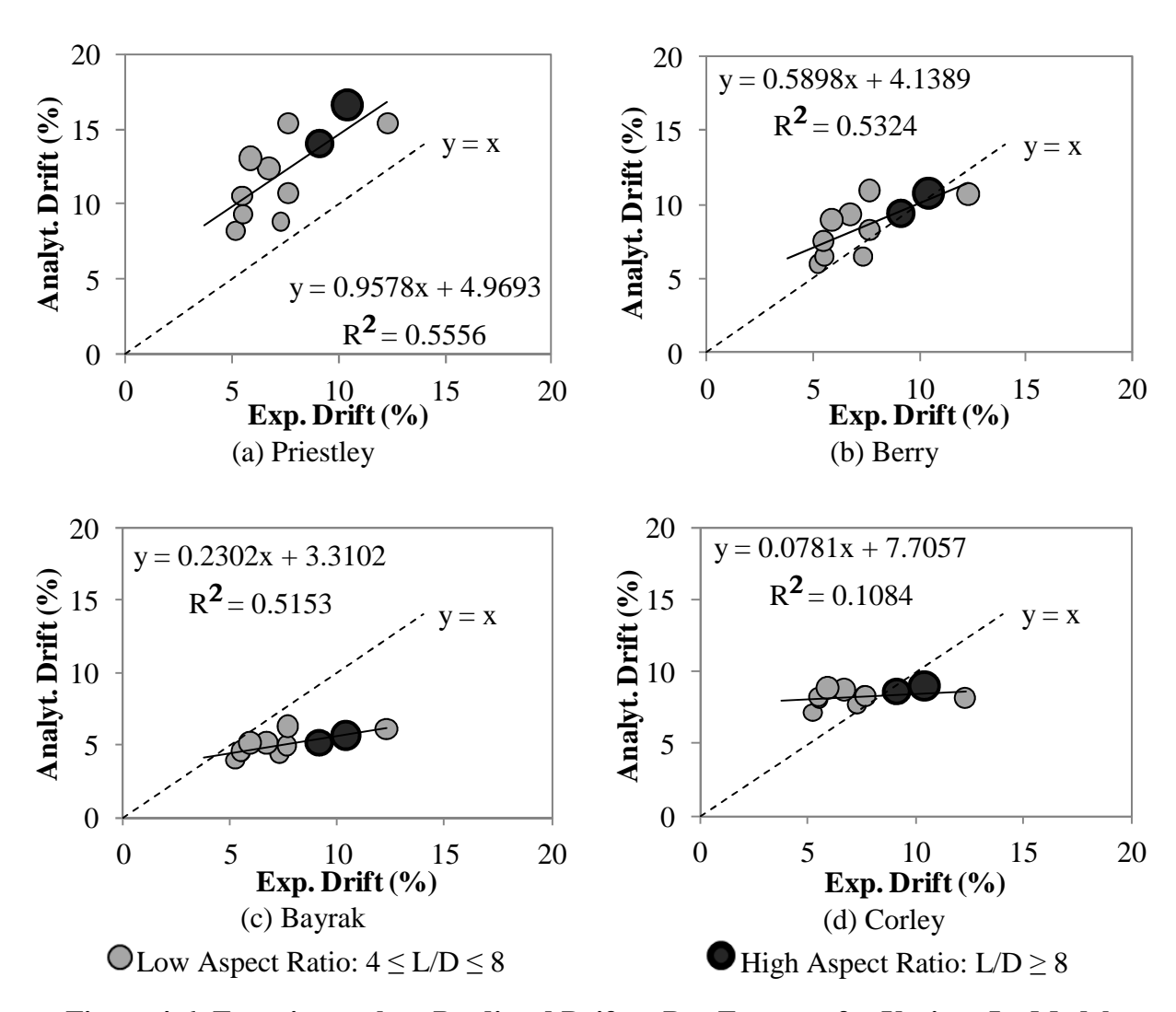


Figure 4-6: Experimental vs. Predicted Drift at Bar Fracture for Various  $L_p$  Models

# **4.4.1.5** Transverse Spiral Fracture

Transverse steel spiral fracture typically occurs when buckled longitudinal reinforcement pushes against the spiral over successive loading cycles, causing it to eventually kink and fracture. Such a damage state would also result in failure of a column. Due to the fact that this component of the column is not explicitly modeled as a steel part in the sectional analyses, this limit state was not directly compared to the experimental data given in the SPD. This damage state however was

assumed as an instance of failure if a displacement was recorded for spiral fracture in the database and is taken into account in the following discussion on ultimate displacement.

## **4.4.1.6** Ultimate Displacement

Ultimate displacement is also referred to as column failure within this study. There is no damage state listed as ultimate, or failure, within the PEER SPD; however, if a column experienced longitudinal bar fracture or transverse spiral fracture, the corresponding displacement was assumed to be the failure instant of the column. In a few cases, a column listed in the database was documented to have experienced spalling of crushing of concrete but no damage to the steel reinforcement. In such cases, the column was assumed to have not failed and the ultimate limit state for the column was not compared to the numerical data.

Determining failure or ultimate conditions in the finite element simulations consisted of defining three criteria that typically indicate failure in a column. The displacement at first occurrence of the following criteria was assumed to be the ultimate displacement of the column:

• Concrete failure: The column is said to have failed by concrete failure in the analyses if the strain in the extreme fiber in the concrete core reaches the ultimate strain,  $\varepsilon_{cu}$ , as defined by the Chang and Mander concrete model (Chang 1994). According to this model, the ultimate concrete strain is defined as (variables defined in Section 3.1.1.3):

$$\varepsilon_{CU} = 0.004 + 1.4 \rho_S \varepsilon_{SU} \frac{f_y}{f'_{CC}}$$
 4-5

- Steel failure: The column is said to have failed by steel failure if the strain in the extreme tensile fiber of the reinforcing steel reaches the ultimate strain,  $\varepsilon_{su}$ , defined in the bar buckling section as 0.1.
- Capacity loss failure: The column is said to have failed by capacity loss if the load
  carrying capacity of the structure falls below 80% of the maximum force determined
  from the element analysis before succumbing to failure of concrete or steel materials as
  described above.

The experimental versus predicted drift at column failure is shown in Figure 4-7 for each plastic hinge model. The Priestley and Berry models again show better correlation to the experimental data than the others. These models also show similar trends to the fracture limit state. The Priestley model again overestimates nearly all data points, while the Berry model shows slightly less error. The Bayrak and Corley models show slightly better prediction of ultimate conditions than the intermediate limit states. Since these models were mainly calibrated with ultimate displacements, improved results are expected. However, their accuracy in predicting ultimate displacement is inferior to the other two models and does not show ideal results for use in PBD.

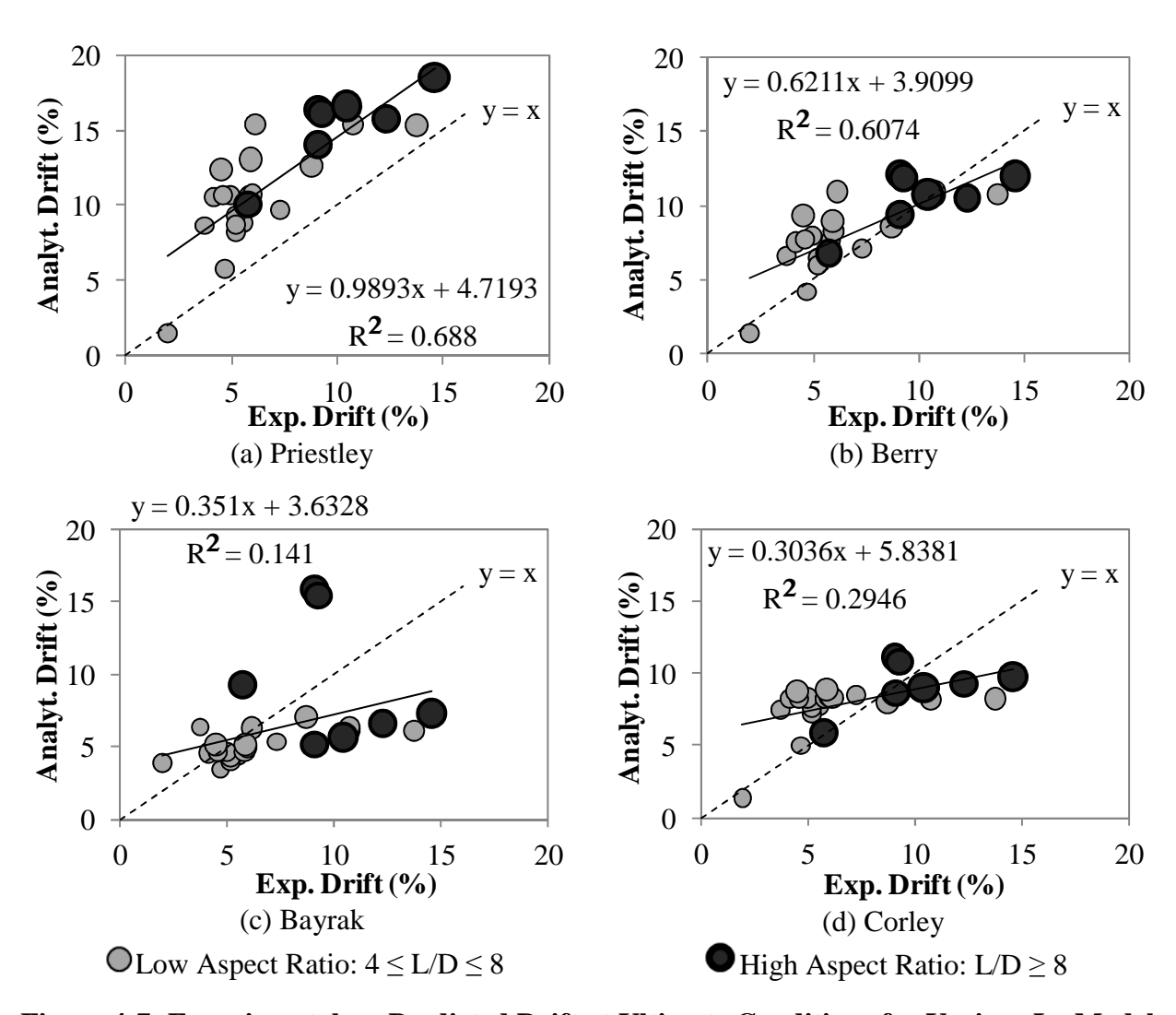


Figure 4-7: Experimental vs. Predicted Drift at Ultimate Conditions for Various  $L_{\rm p}$  Models

## **4.4.2** Conclusions of Plastic Hinge Design Models

The mean error produced by each plastic hinge model for the five limit states is given in Table 4-4. Based on the results of the limit state analyses, many trends were observed regarding the plastic hinge models' abilities for use in PBD. It was shown that none of the current plastic hinge models accurately predict concrete damage states. Concrete is a complex material with largely varying properties. While sophisticated models exist for concrete materials (OpenSees 2011, Chang and Mander 1994), it is difficult to predict the instant at which damage to the material will

initiate, either by observation or numerical studies. Also due to its complexity, well-defined limit states at concrete damage states do not currently exist. Before prediction models can be improved, a more uniform definition of concrete limit states (especially concrete spalling) is necessary. While concrete damage states do not typically indicate significant structural damage, their onset indicates a need for column repair and retrofit in order to prevent more severe damage in the future. Developing improved definitions and models for concrete damage states is very important to the implementation of PBD.

Individual performance by plastic hinge design models varies between limit states. This is shown in Table 4-4 which gives the mean error and coefficient of variance for each plastic hinge model. The Priestley and Berry models generally show higher capability in predicting intermediate and ultimate limit states over the models by Bayrak and Corley. The model by Berry shows more consistency in its prediction than the Priestley model, which at increasing damage shows over-prediction of drift. The Berry model shows the least amount of error for the majority of the limit states as shown in Table 4-4; however error is still quite large for the data set of 34 columns. This therefore indicates that improvements may be necessary before any of the studied plastic hinge models may be reliably used for PBD.

**Table 4-4: Mean Percent Limit State Error and COV per Plastic Hinge Model** 

CRUSHING L.S.							
Lp Model	Mean Error (%)	COV (%)					
Priestley	40	79					
Berry	26	70					
Bayrak	27	71					
Corley	30	74					
SPALLING L.S.							
Priestley	32	78					
Berry	36	67					
Bayrak	44	55					
Corley	36	67					
BAR I	BAR BUCKLING L.S.						
Priestley	42	76					
Berry	22	74					
Bayrak	37	40					
Corley	27	68					
BAR F	BAR FRACTURE L.S.						
Priestley	66	48					
Berry	22	80					
Bayrak	30	44					
Corley	26	70					
ULTIMATE L.S.							
Priestley	75	60					
Berry	32	92					
Bayrak	34	71					
Corley	39	72					
Total							
Priestley	51	68					
Berry	27	77					
Bayrak	35	56					
Corley	32	70					

# 5 EVALUATION OF NUMERICAL ANALYSIS METHODS AND SLENDERNESS EFFECTS

This chapter documents a numerical study aimed at evaluating modeling methods previously discussed in the thesis and compares them in detail to experiments on columns of varying slenderness. In order to study the accuracy of different numerical methods and the effect of slenderness in reinforced concrete columns, test units were modeled with lumped plasticity and distributed plasticity elements. The evaluation of global behavior is presented first, which compares the predicted and experimental hysteretic responses. Local behavior was studied by considering curvature and displacement distributions along the column's height. The spread of plasticity was also determined and trends were observed in relation to the previously discussed model by Hines et al. (2004). Finally, limit states were compared between monotonic and cyclic analyses and between element models to determine any significant cumulative damage effects and accuracy to the experimental data.

#### 5.1 Selected Columns

In order to test the validity of different numerical models for predicting limit states as well as study the effects of slenderness, five columns were chosen to complete a data set of aspect ratios (L/D) between 4 and 12. The distribution of slenderness in the columns studied from the PEER SPD is shown in Figure 5-1. As shown, most columns that have been tested in an experimental setting are between aspect ratio 4 and 6. Therefore, there is a lack of research completed in slender columns such as those with aspect ratios 8 and above. The set of five columns studied herein cover a wide range of slenderness ratios to determine the effectiveness of several modeling approaches as well as determine the effect of slenderness on the spread of plasticity

and modeling capabilities. The columns studied were three units tested at the University of California, Berkeley (L/D = 4, 8, 10) (Lehman and Moehle 2000), one unit tested at the University of California, San Diego (L/D = 6) (Hose et al. 1997) and one tested at Michigan State University (L/D = 12) as part of this study. All columns were half-scale models of circular cross-section and conformed to modern seismic design standards for reinforced concrete structures. The geometric and reinforcement properties of each column are given in Table 5-1.

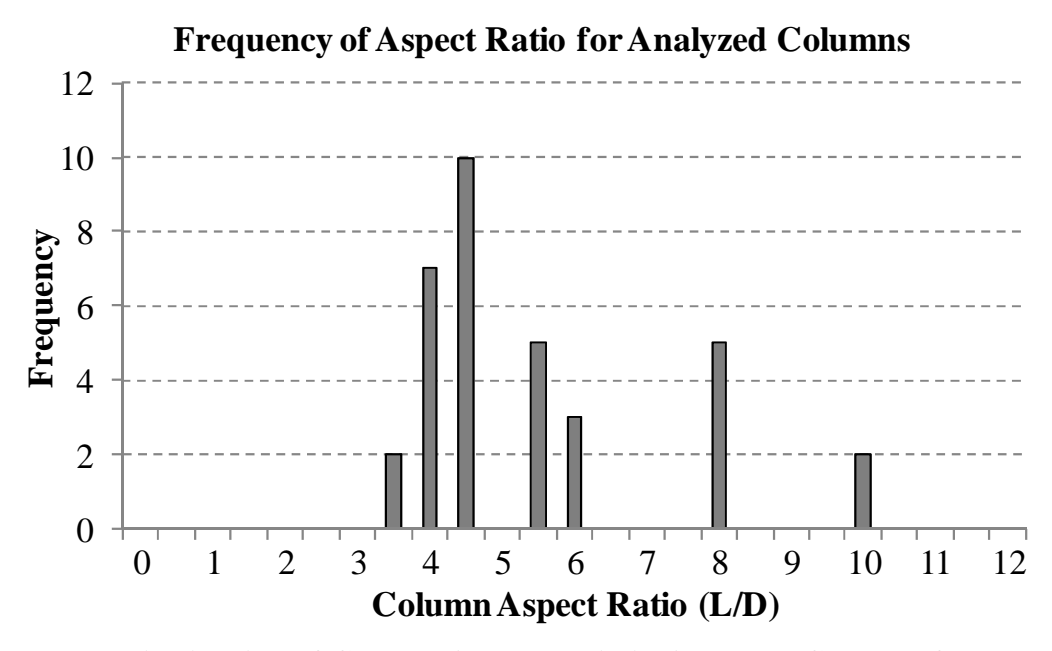


Figure 5-1: Distribution of Column Aspect Ratio in Analyzed Columns from the SPD

Table 5-1: Column Properties for Evaluation of Numerical Analysis and Slenderness

Column Reference	Aspect Ratio	Length (ft.)	Longitudinal Reinforcement	Cover (in)	Transverse Reinforcement	Axial Load Ratio
415 (Lehman and Moehle 2000)	4	8	22 # 5 ρ <sub>l</sub> =1.5%	0.75	#2 spiral @ 1.25" ρ <sub>s</sub> =0.70%	7.22%
SRPH1 (Hose et al. 1997)	6	12	20 # 7 ρ <sub>1</sub> =2.7%	1	#3 spiral @ 2.25" ρ <sub>s</sub> =0.86%	14.82%
815 (Lehman and Moehle 2000)	8	16	22 #5 ρ <sub>1</sub> =1.5%	0.75	#2 spiral @ 1.25" ρ <sub>S</sub> =0.70%	7.22%
1015 (Lehman and Moehle 2000)	10	20	22 #5 ρ <sub>1</sub> =1.5%	0.75	#2 spiral @ 1.25" ρ <sub>S</sub> =0.70%	7.22%
123007 (see Ch.4)	12	24	18 #8 ρ <sub>1</sub> =3.1%	1	#4 spiral @ 3" ρ <sub>S</sub> =1.16%	7.00%

# **5.2** Specific Modeling Approaches

The aforementioned columns were evaluated in OpenSees simulation platform using lumped plasticity and distributed plasticity elements. The general description and formulation of these elements was presented in Section 3.1. The fiber section shown in Figure 4-2 was refined to include 50 radial divisions for the inelastic cyclic assessment in each analysis.

Monotonic and cyclic analyses were performed as part of this study. Monotonic (pushover) loading was applied as discussed in Section 4.3.1. Cyclic loading was applied under displacement control in increments of the final displacement target, as specified by each column loading protocol. Thus, the displacement targets used in the cyclic analyses match those reached during each test, rather than based on predicted yield and ultimate values. This was done to facilitate comparison of the experimental analytical responses. The loading history completed

during testing of each column and implemented in the simulations is shown in Table 5-2. Preyield cycles varied per column; however, for modeling purposes, pre-yield loading consisted of one cycle for each quarter-increment of the ideal yield force. Post-yield loading consisted of three fully-reversed cycles for each ductility level considered (see Table 5-2) before proceeding to the loading/deformation level.

Table 5-2: Cyclic Load Levels of Analyzed Columns

415	SRPH1	815	1015	123007
pre-yield	pre-yield	pre-yield	pre-yield	pre-yield
Δy	Δy	Δy	Δy	Δy
1.5∆y	1.5∆y	1.5∆y	1.5∆y	1.5∆y
2Δ <b>y</b>				
3∆у	3∆у	3∆у	3∆у	3∆у
5∆у	4∆y	5∆у	5∆у	-
7∆у	6∆у	-	-	-
-	8Ду	-	-	-

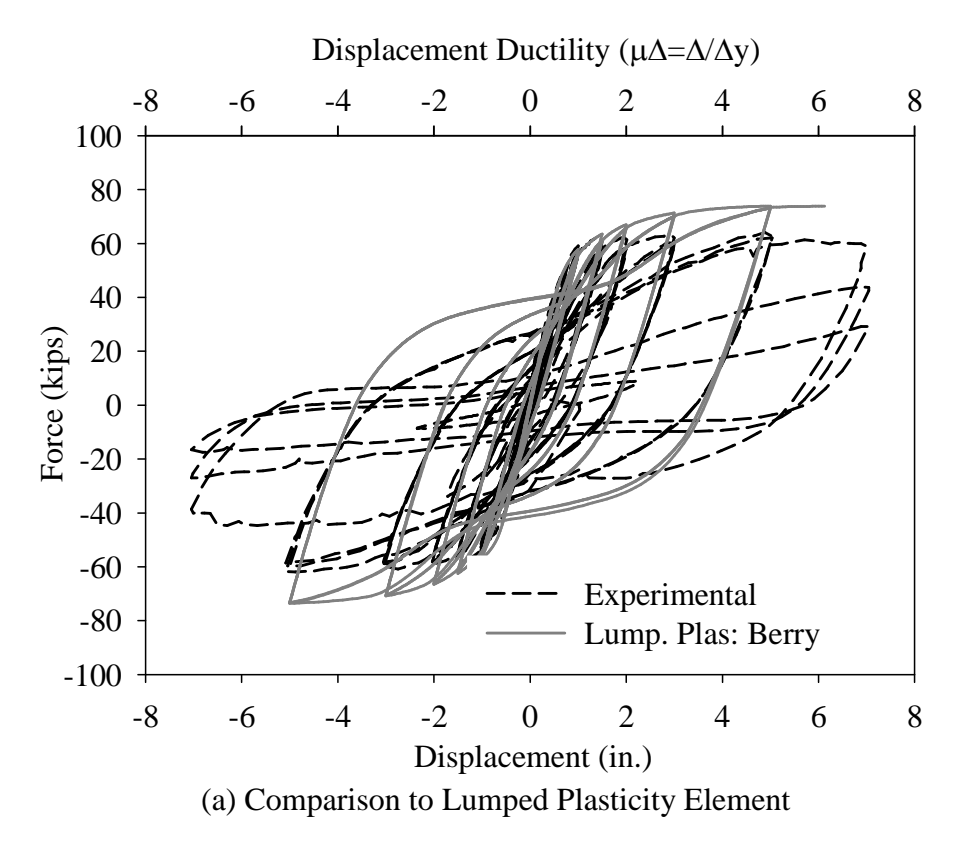
## **5.3** Global Response

The experimental global hysteretic force-displacement (shear force vs. tip lateral displacement) response of each of the five test units was compared to analyses using both lumped plasticity and distributed plasticity elements. The lumped plasticity element was modeled using the plastic hinge length model by Berry et al (2008). Results from the SPD study in Chapter 4 gave preliminary evidence of the Berry plastic hinge model being most accurate of the four studied; this fact is further confirmed with the results presented later in this chapter in Section 5.6. The L<sub>p</sub> model proposed by Berry et al. was therefore used for further analyses. Figure 5-2 through Figure 5-6 give the experimental versus analytical response of each column, in order of increasing aspect ratio. Graph (a) in each figure shows the response obtained from the lumped

plasticity model against experimental results, while graph (b) shows the distributed plasticity model results against the experimental measurements.

It can be seen that for all five columns the lumped plasticity models more accurately captured the initial stiffness of the column compared to the distributed plasticity models, which showed a softer initial response. However, again for all five cases the distributed plasticity models more accurately captured post-yield behavior than the lumped plasticity models, which tend to overestimate the force capacity of the columns.

Regardless of element type, a trend in accuracy based on aspect ratio was also observed from the comparisons. With the exception of column 415, the error in global force response increases as aspect ratio increases. The aspect ratio 4 column, while not as well predicted as the following two columns (Hose and 815), does show reasonably accurate results. One possible explanation of discrepancy between experimental and analytical data in this case may be due to shear effects since column 415 is relatively short. The comparisons show that the columns with aspect ratios 6 and 8 were very well predicted by the analyses, while the numerical prediction for the columns with aspect ratios 10 and 12 were over-estimated in force capacity by both analysis approaches. This indicates that there are factors in the higher aspect ratio columns that are not captured by the evaluated analysis methods. The lower capacity reflected in the experimental response of columns 1015 and 123007 is likely due to second order (P-delta) effects controlling the behavior. This effect is addressed in the following section.



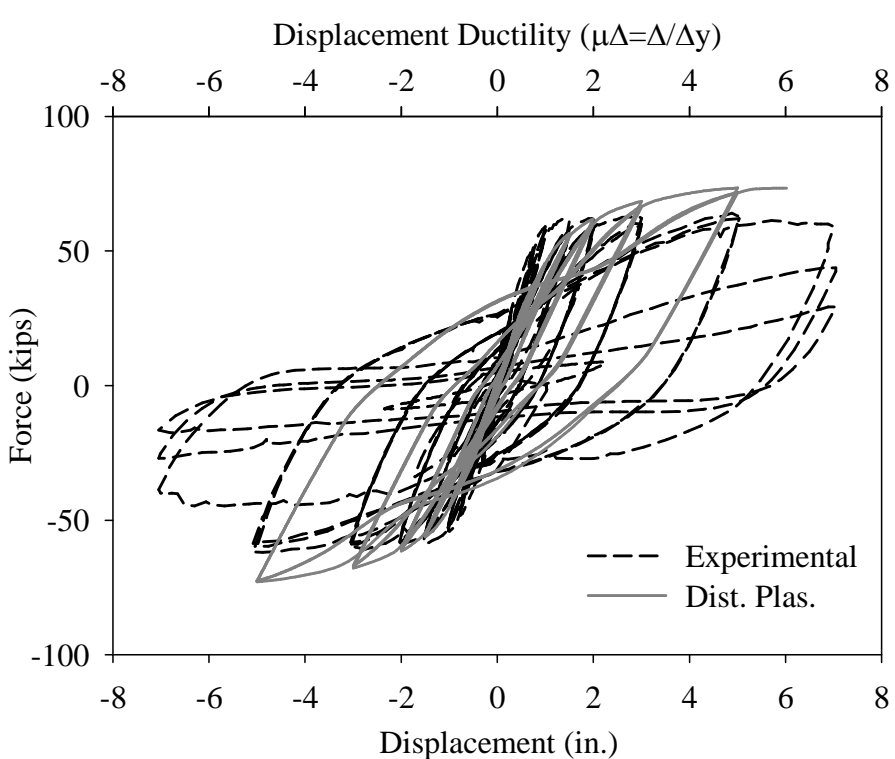
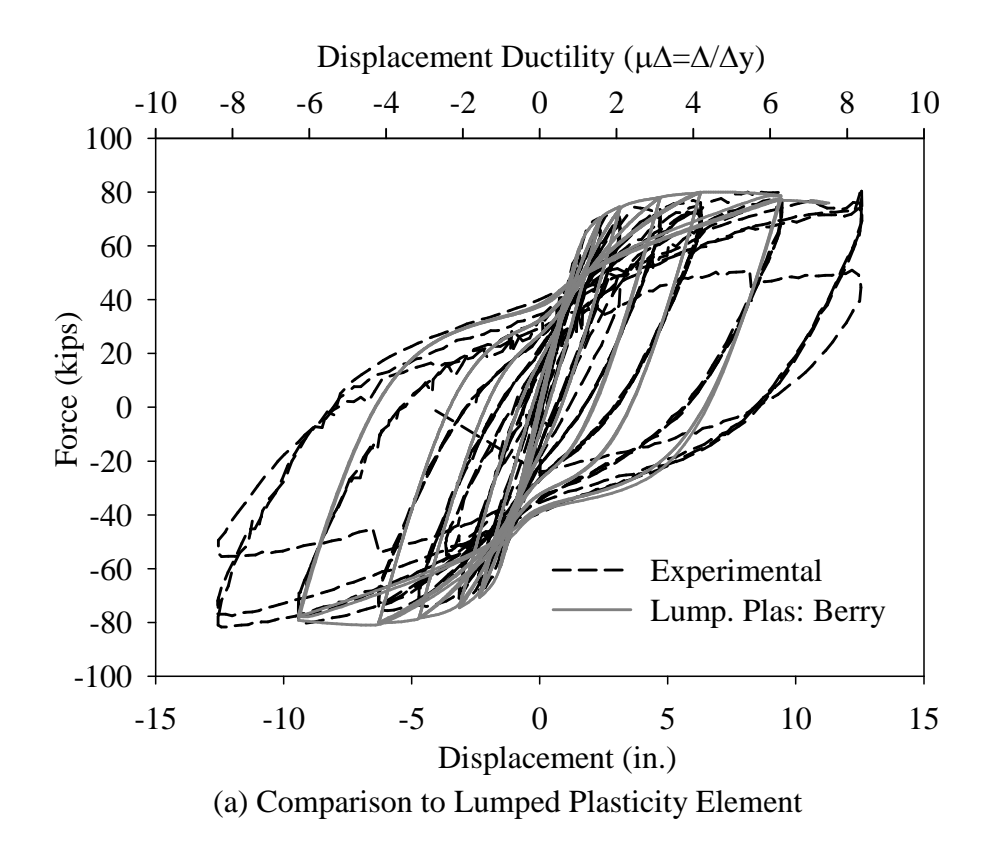


Figure 5-2: 415 Experimental vs. Analytical Hysteretic Response

(b) Comparison to Distributed Plasticity Element



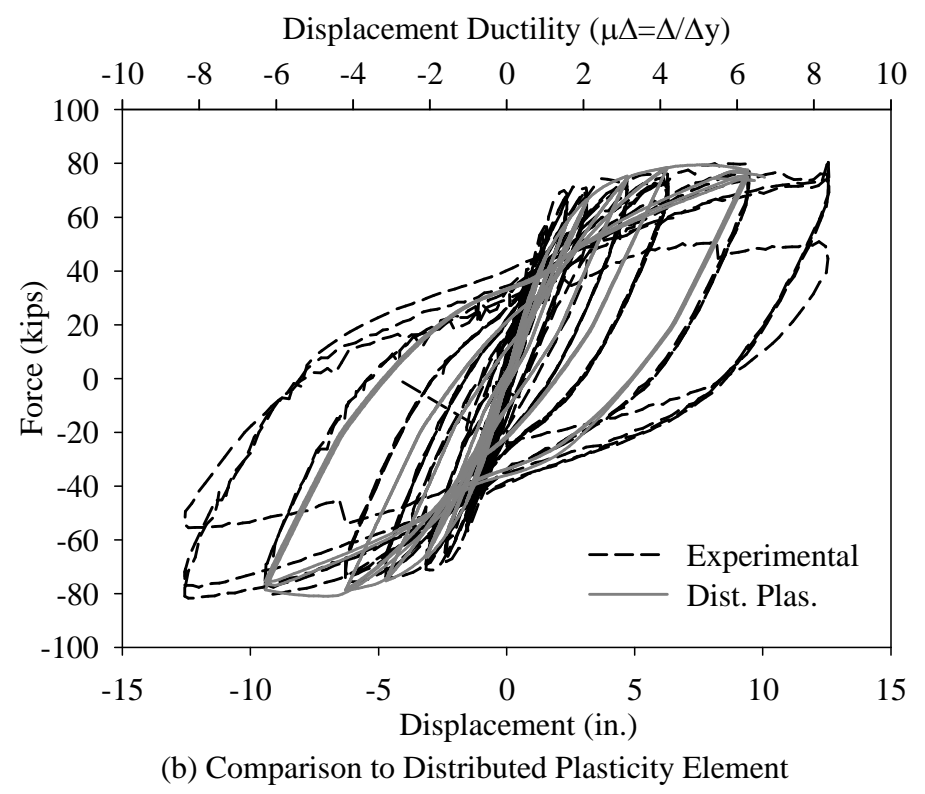
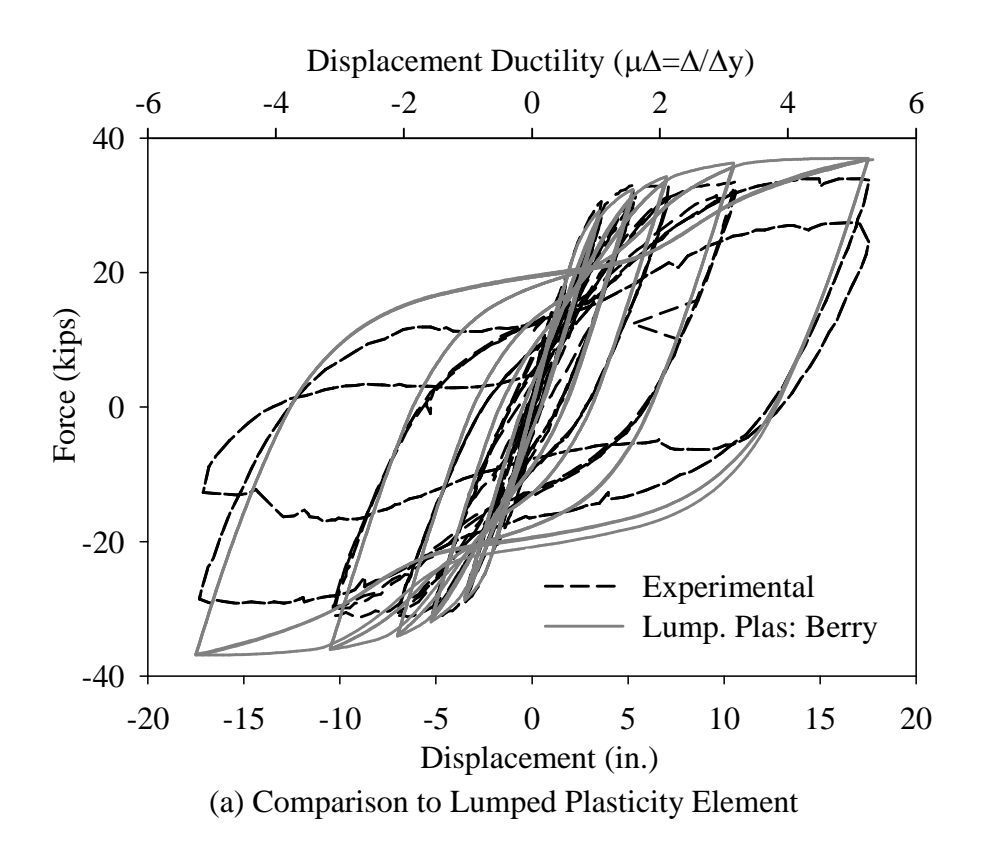


Figure 5-3: SRPH1 Experimental vs. Analytical Hysteretic Response



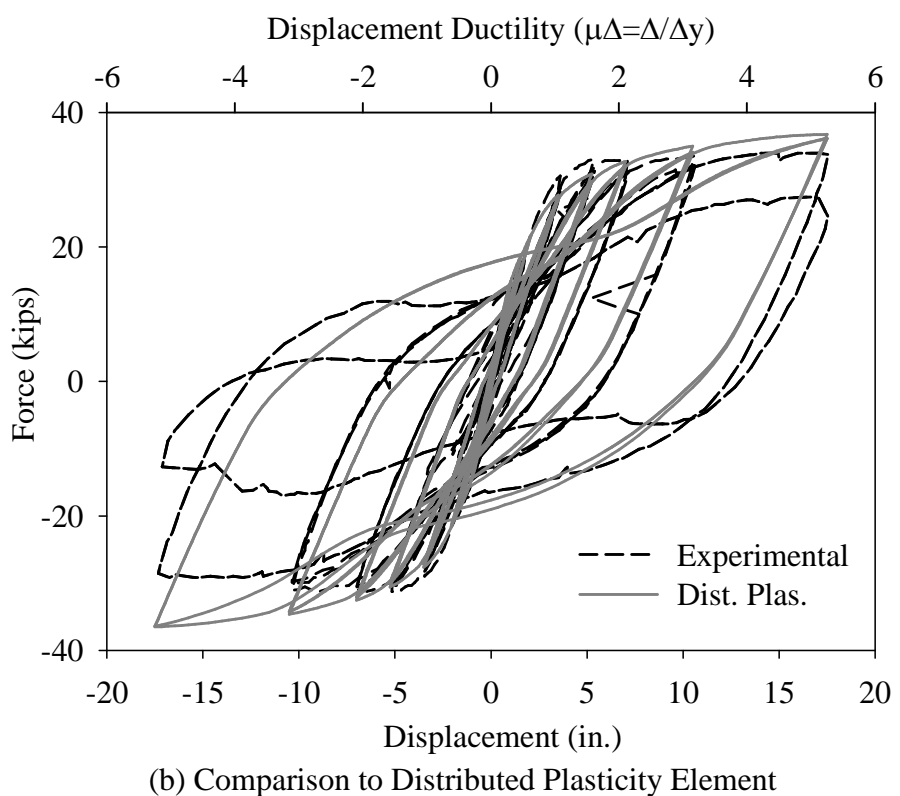
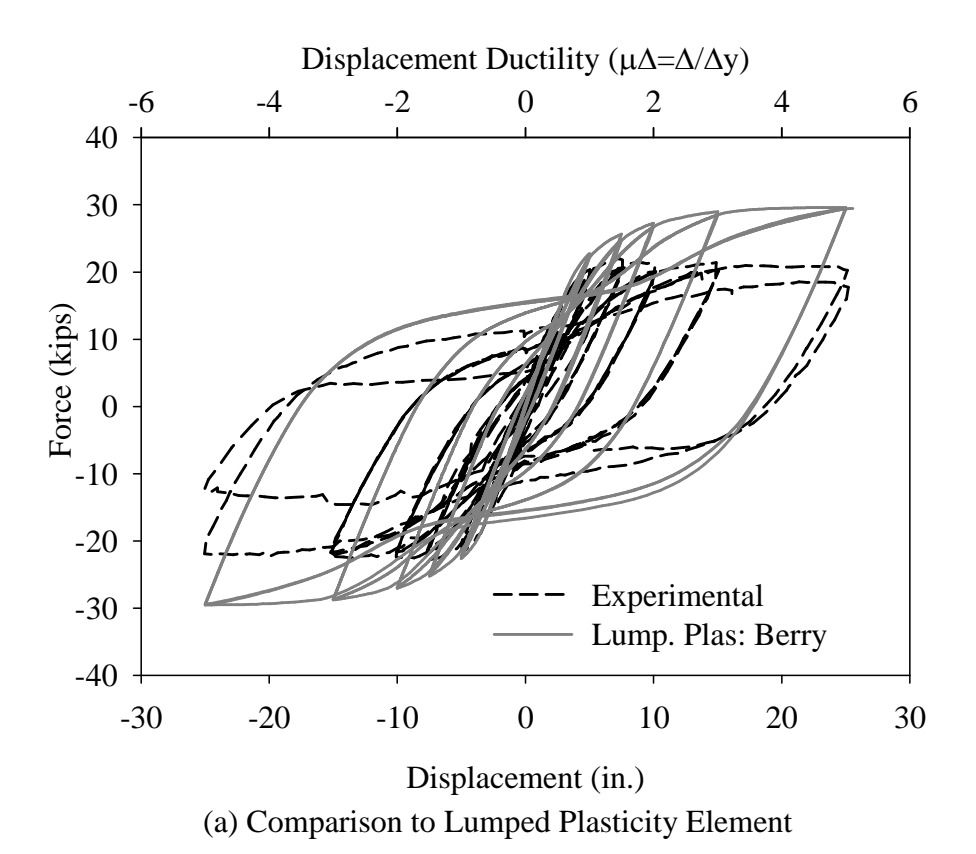


Figure 5-4: 815 Experimental vs. Analytical Hysteretic Response



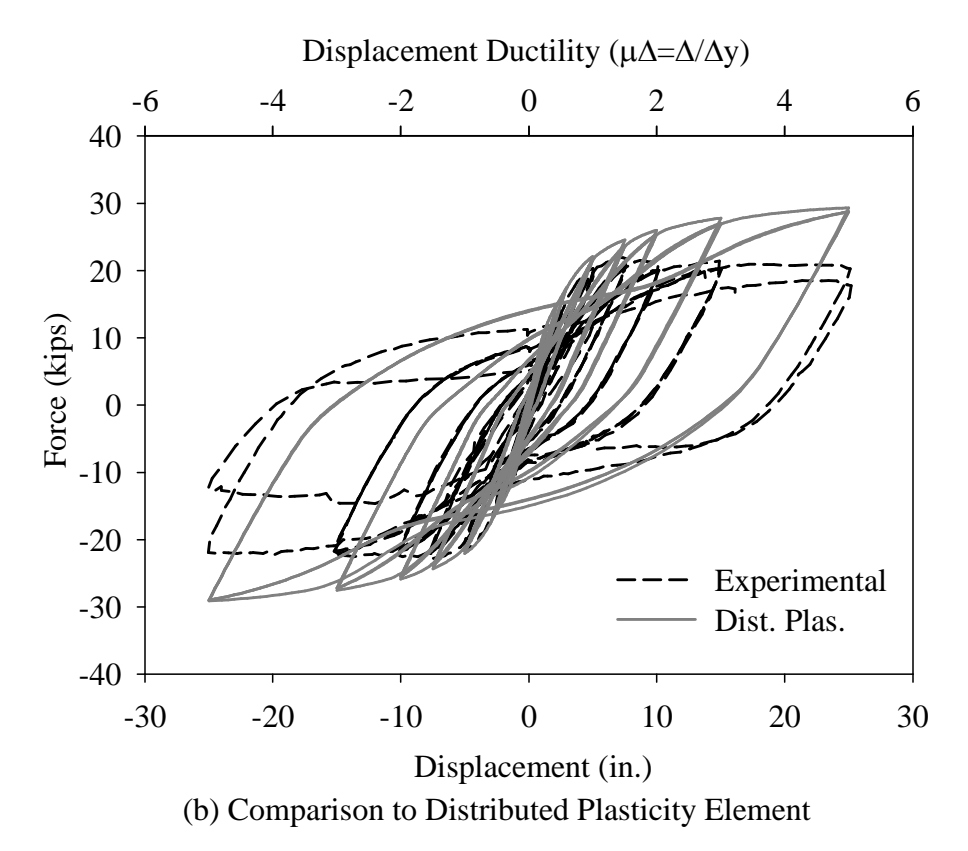
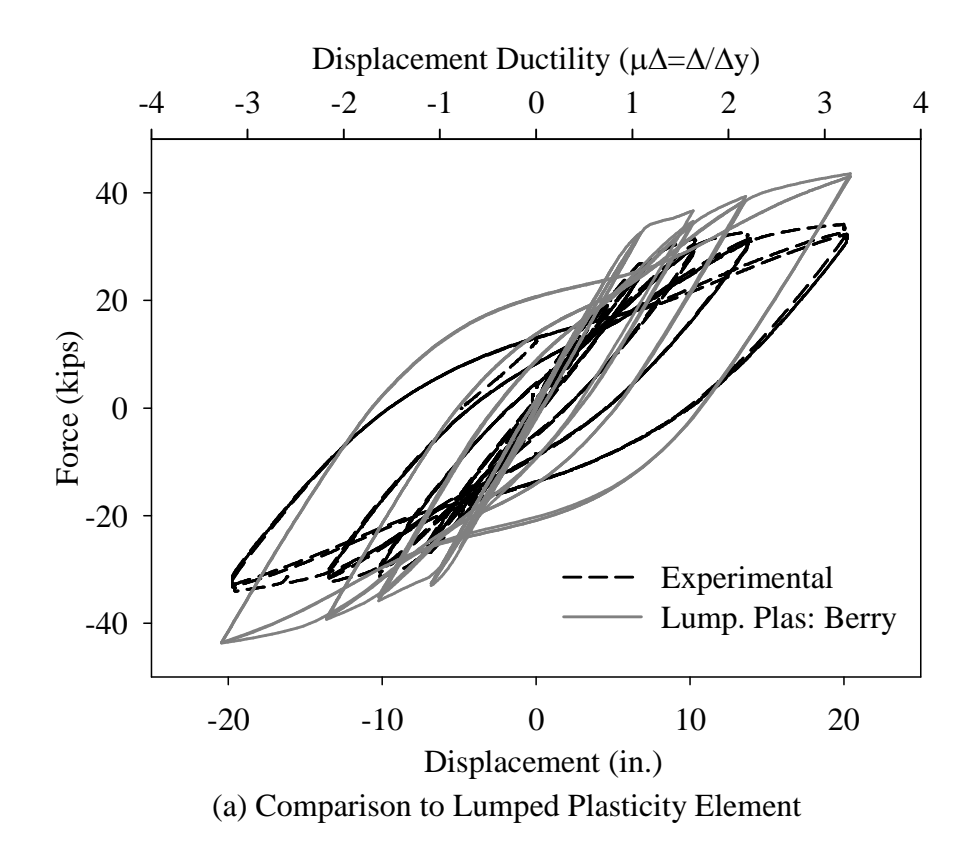


Figure 5-5: 1015 Experimental vs. Analytical Hysteretic Response



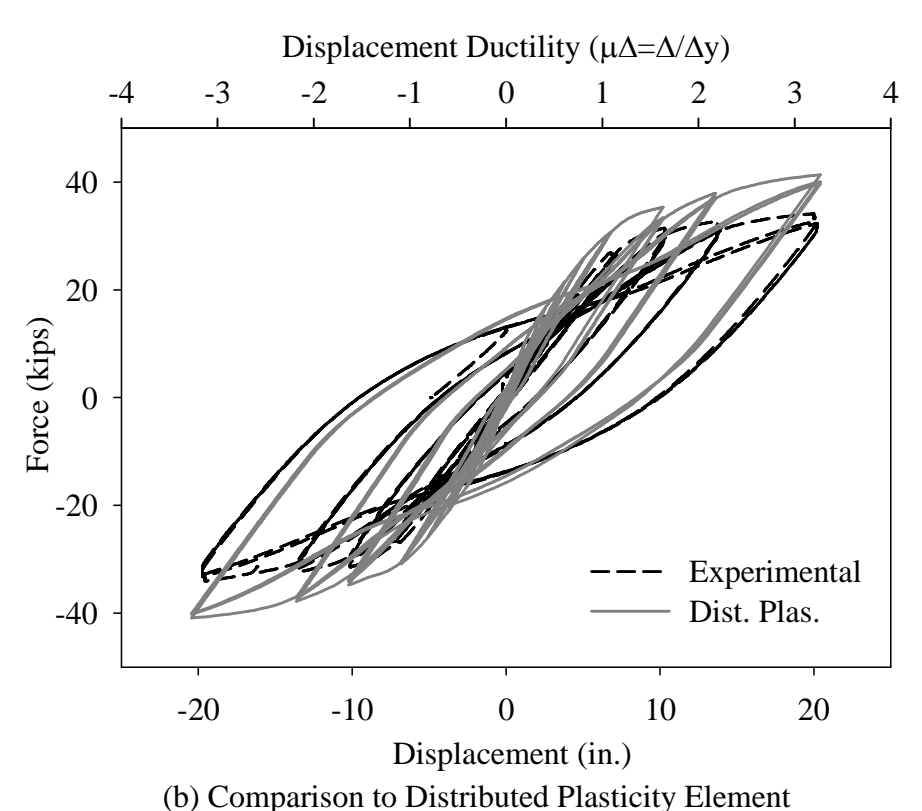


Figure 5-6: 123007 Experimental vs. Analytical Hysteretic Response

#### **5.3.1** Second Order Effects

# **5.3.1.1** Effect of Column Test Setup

In an experimental setup, axial load is typically applied by means of external hardware (see Section 3.2.5 for more information). In most cases, the axial force does not remain vertical as the column is displaced, but rather follows the trajectory of external rods used to compress the column. Because of this, there is a horizontal component to the axial force that is being resisted by the actuator applying the lateral load, leading to "incorrect" measured horizontal shear forces resisted by the column. The SPD User's Manual addresses this issue and outlines how the force data reported by the researchers should be corrected to obtain a net horizontal force, FH (Berry et al. 2004). According to the SPD User's Manual, there are four common methods by which axial load is applied to cantilever test columns, each requiring different formulations to correct for the net horizontal force. The two cases representative of the five case study columns are shown in Figure 5-7, where P is the applied axial load, F<sub>Rep</sub> is the reported lateral force from the actuator and  $L_{Top}$  is the distance from the effective height to the point where axial load is applied (other terms are visually explained). Of the five columns studied herein, four were reported in the PEER SPD as being tested according to axial load 'Case IV'. The fifth, SRPH1, was reported as being tested according to 'Case I'. In order to obtain the "corrected force" the following set of equations should be used for Case IV:

$$\alpha = tan^{-1} \left[ \frac{\Delta \left( \frac{L + L_{top}}{L} \right)}{L + L_{bot} + L_{top}} \right]$$
 5-1

$$P_H = P * sin\alpha$$
 5-2

$$F_H = F_{Rep} - P_H ag{5-3}$$

And Equation 5-4 should be used for Case I:

$$F_H = F_{Rep} - \frac{P\Delta}{L}$$
 5-4

The majority of researchers do not correct test data when reporting information and comparing analytical results. For low aspect ratio columns (i.e., L/D = 4), the horizontal component of the axial load setup is insignificant and correction is not typically necessary. However, as aspect ratio increases, this component becomes increasingly large and drastically changes the global response of the column. The global hysteretic response of the five columns has been corrected according using the appropriate equations and the results are shown in comparison to the reported data in Figure 5-8 through Figure 5-12.

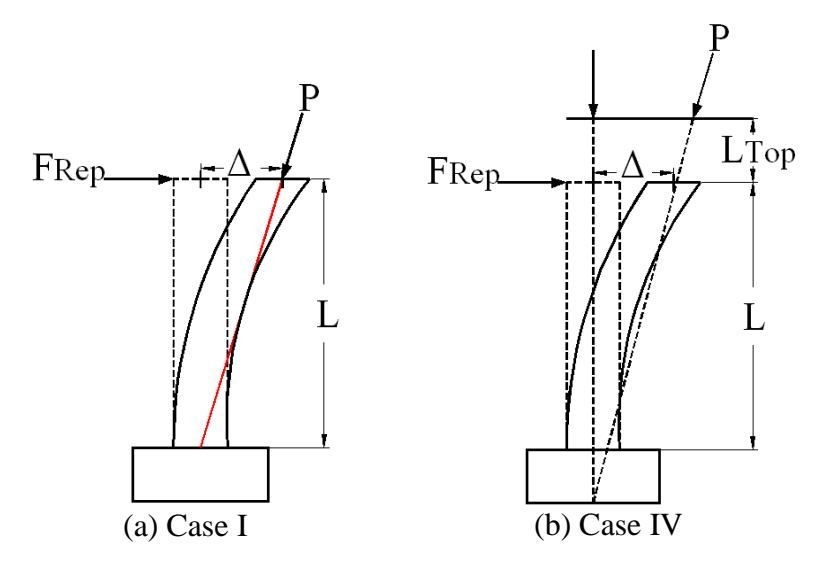


Figure 5-7: Axial Load Correction Cases for Experimental Columns (Berry et al. 2004)

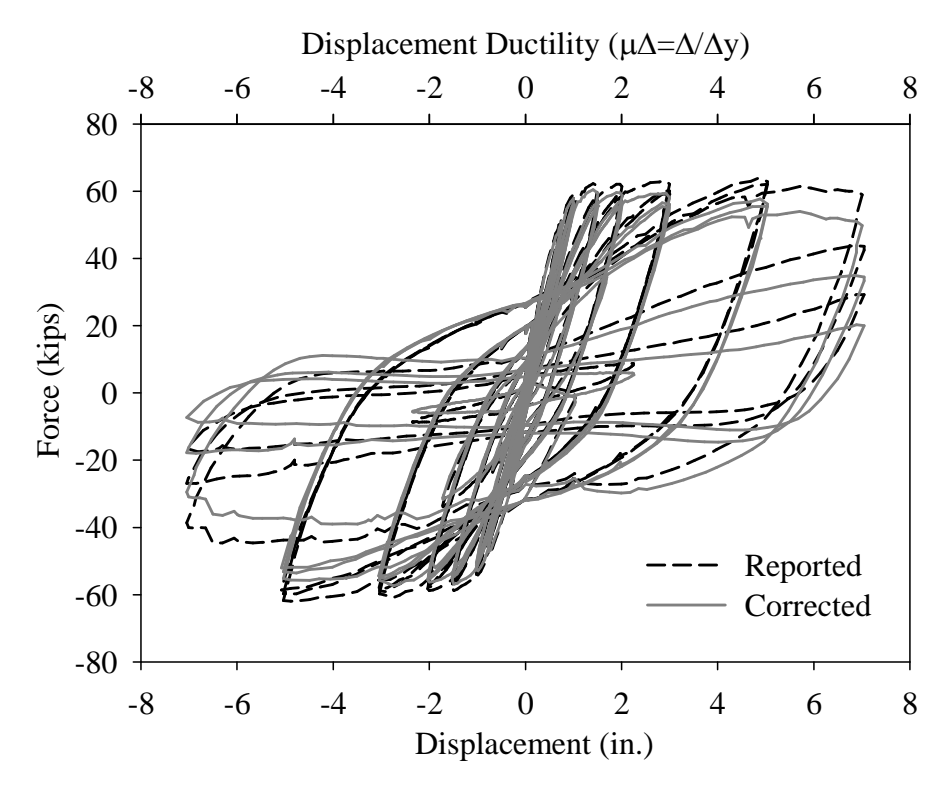
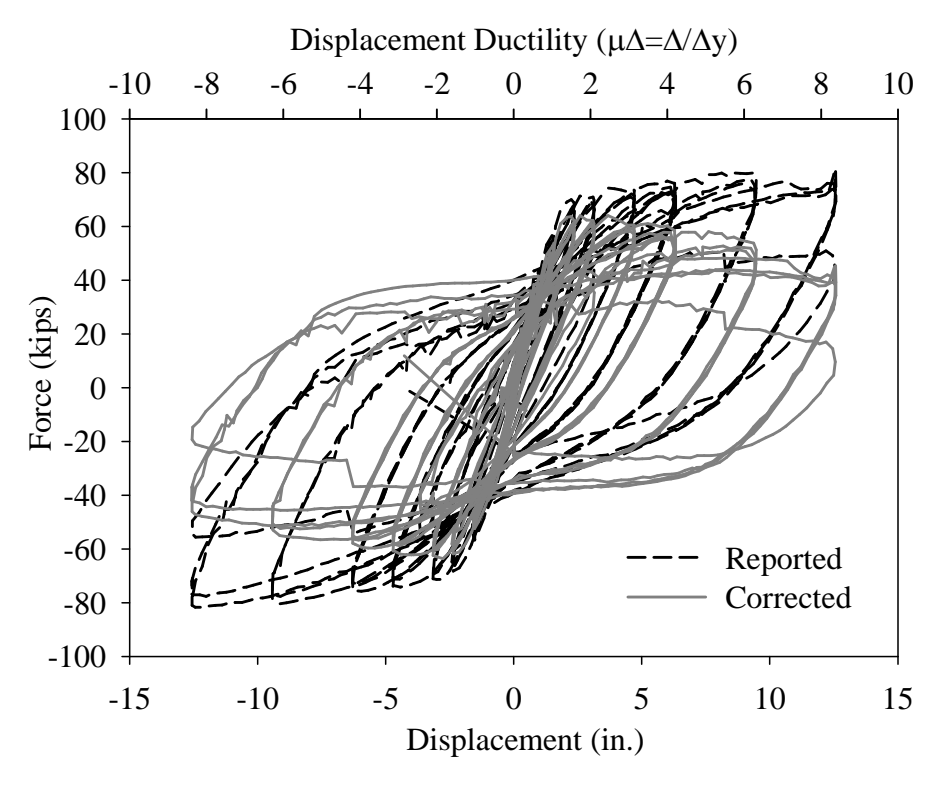


Figure 5-8: 415 Corrected Force Data



**Figure 5-9: SRPH1 Corrected Force Data** 

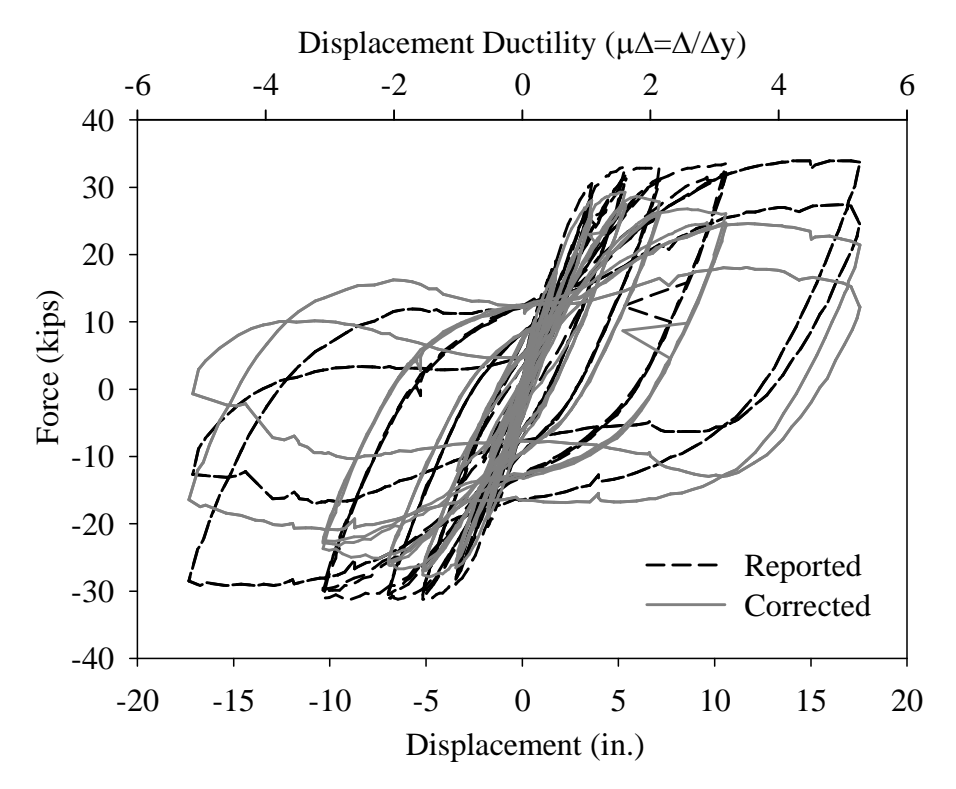


Figure 5-10: 815 Corrected Force Data

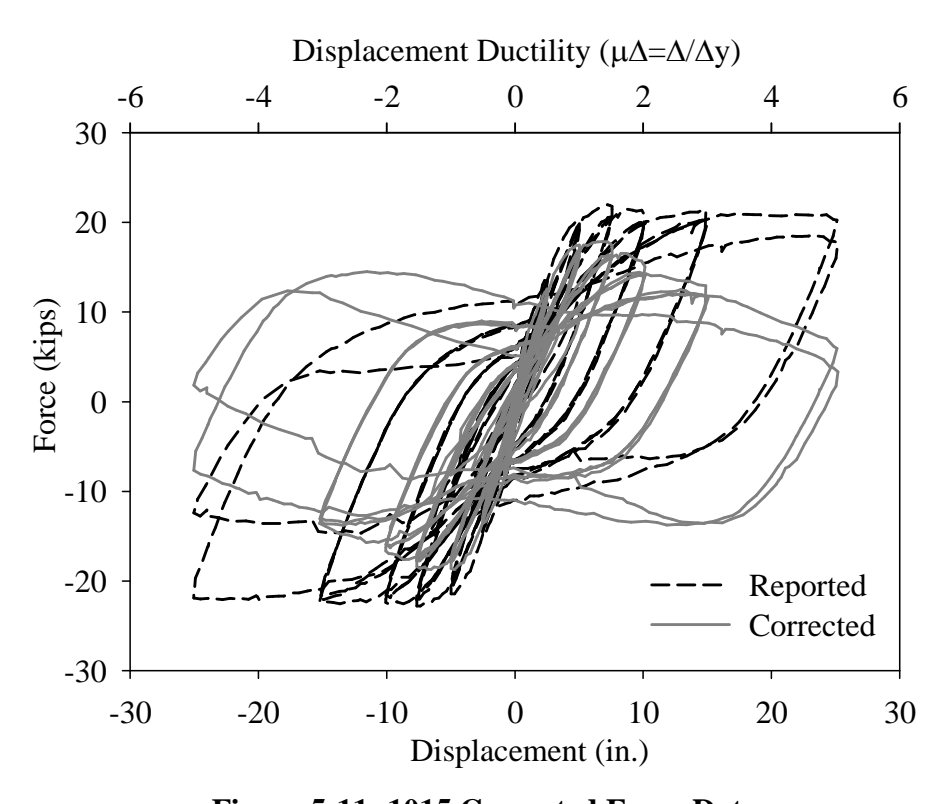


Figure 5-11: 1015 Corrected Force Data

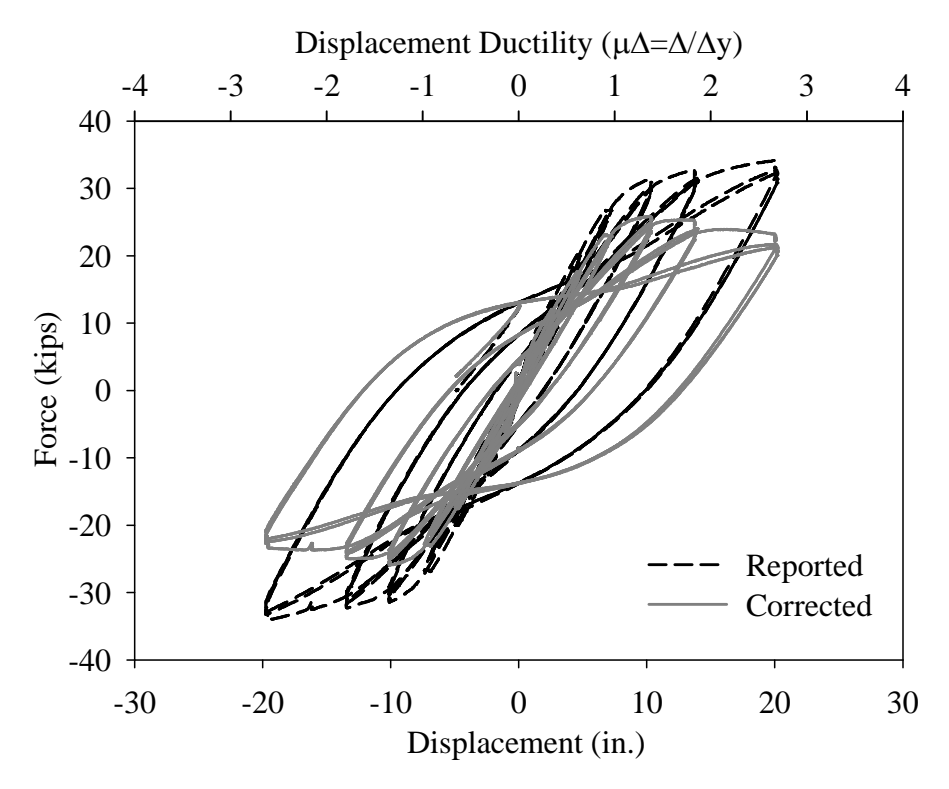


Figure 5-12: 123007 Corrected Force Data

# **5.3.1.2** P-Delta Effects

The test columns likely experienced geometric (P- $\delta$ ) effects at large displacements since the axial load does not directly follow the centerline of the column, as it does in the analyses. This may explain the increasing error between the experimental and analytical hysteretic responses for high aspect ratios. When the force data is corrected, the P- $\Delta$  effects are also being accounted for. It is therefore reasonable to compare the corrected hysteretic response of the columns to an analysis that considers P-delta effects. Such comparisons are shown in Figure 5-13 through Figure 5-17. The analyses were completed using a distributed plasticity element with the integration scheme discussed previously. A distributed plasticity model was chosen for this comparison over a lumped plasticity one since it can be defined with multiple sub-elements and integration points allows the analysis to more accurately capture geometric (P- $\delta$ ) effects, which

is not possible with a single element. P-delta effects are considered in OpenSees by modifying the geometric transformation input to the element from "Linear" to "PDelta" (OpenSees 2011). As shown in Figure 5-13 through Figure 5-17, while the analyses with P-delta effects softens in a way similar to the corrected experimental data, the error in analysis is identical to the error observed in Figure 5-2 through Figure 5-6. For the high aspect ratio columns (L/D = 10, 12), these results indicate that there are additional effects in the column response that are not captured by the analysis, even with P-delta effects considered.

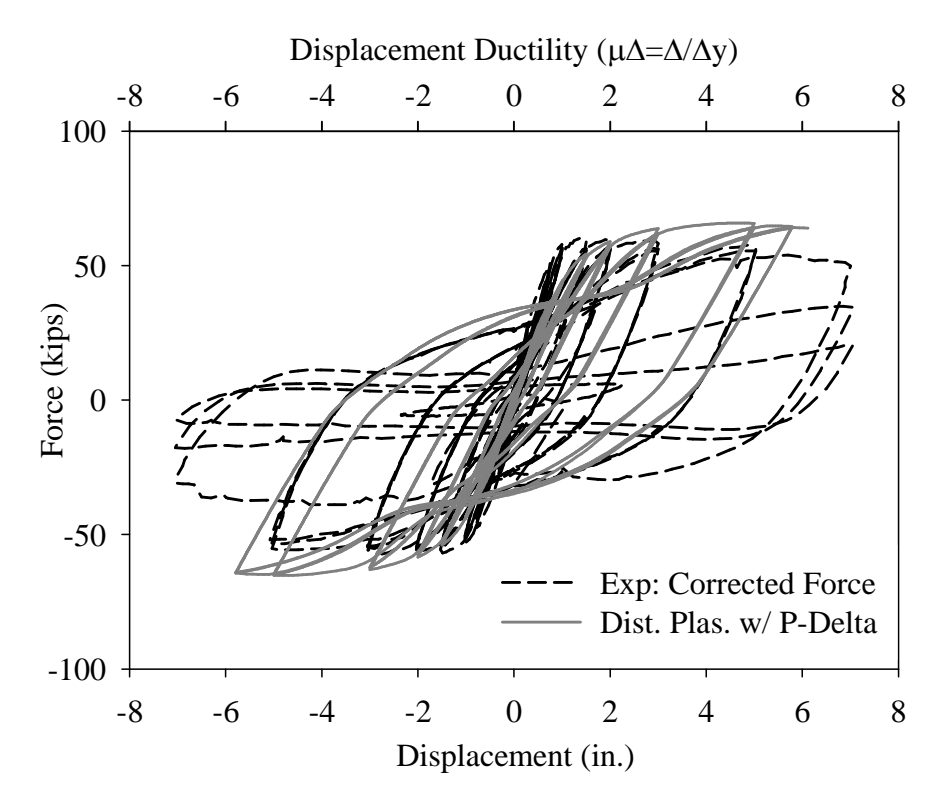


Figure 5-13: 415 Corrected Hysteresis vs. P-Delta Analysis

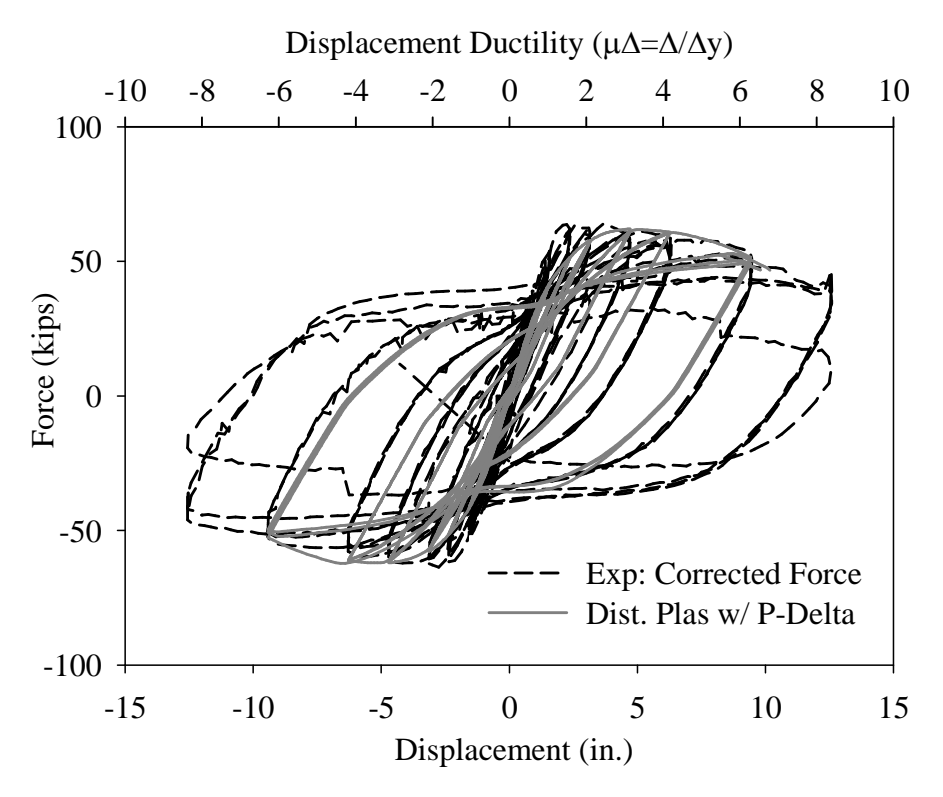


Figure 5-14: SRPH1 Corrected Hysteresis vs. P-Delta Analysis

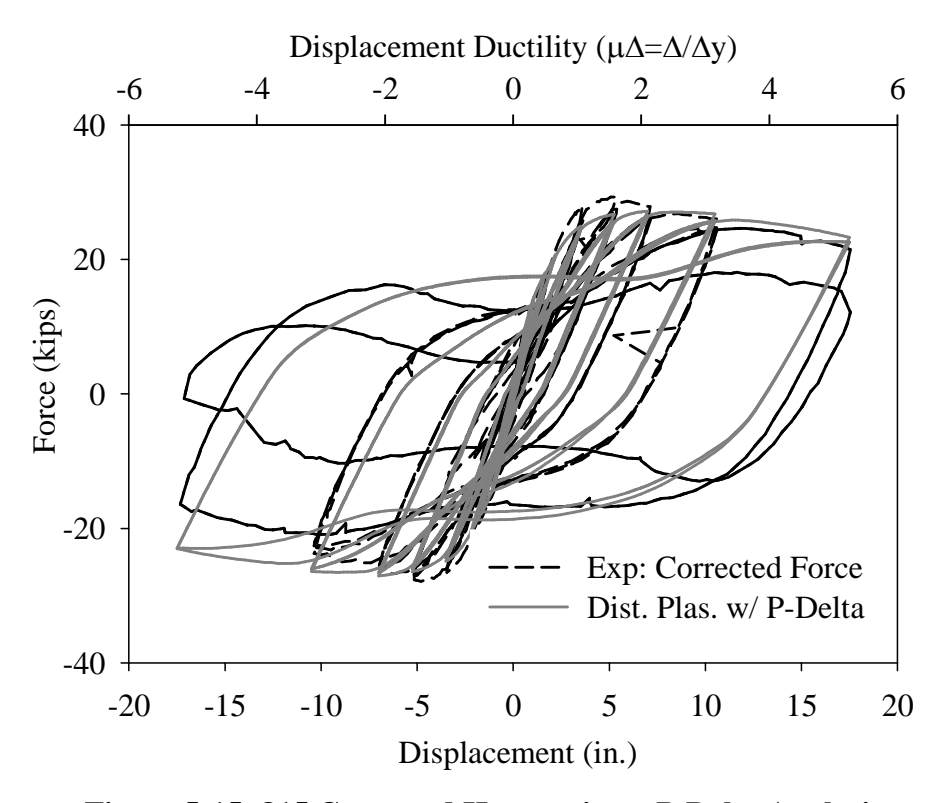


Figure 5-15: 815 Corrected Hysteresis vs. P-Delta Analysis

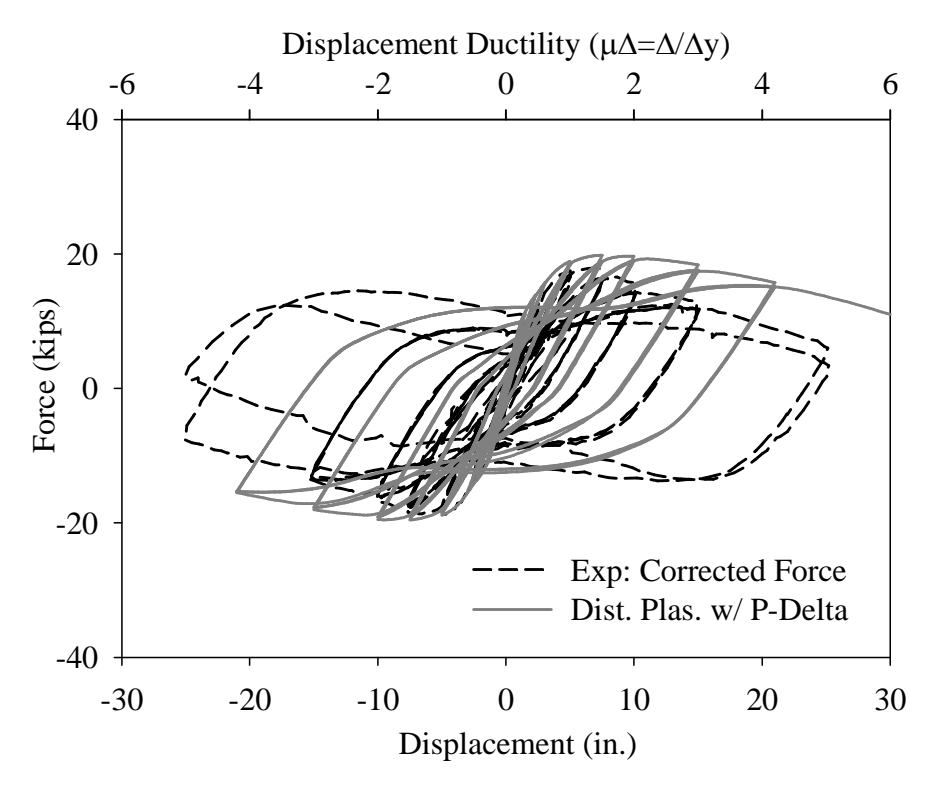


Figure 5-16: 1015 Corrected Hysteresis vs. P-Delta Analysis

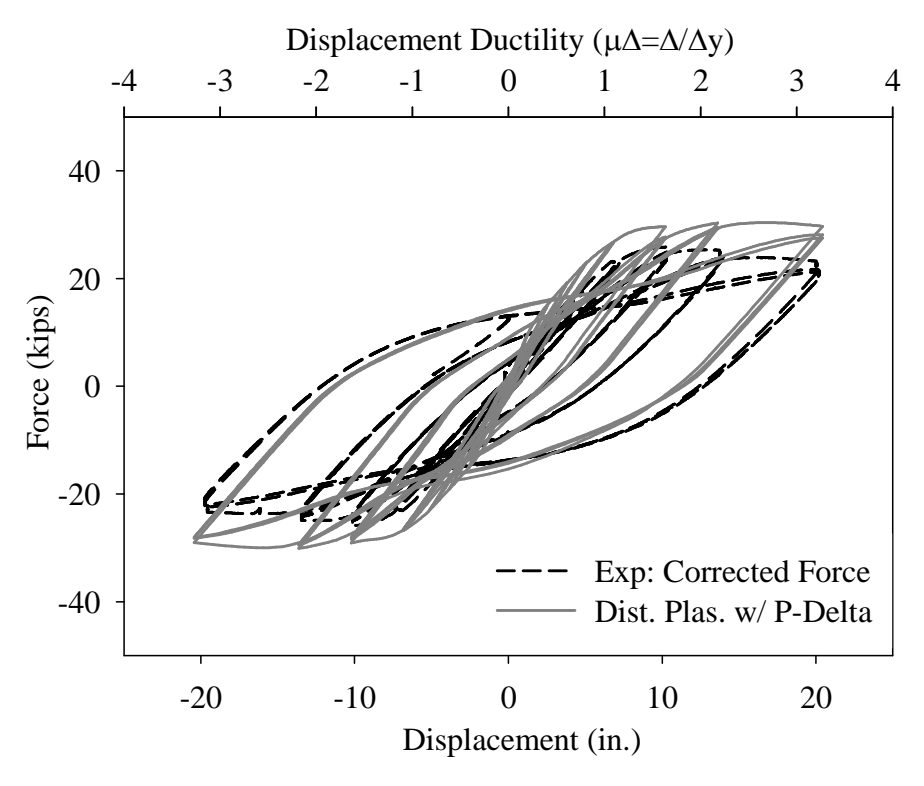


Figure 5-17: 123007 Corrected Hysteresis vs. P-Delta Analysis

To justify the adequacy of the distributed plasticity integration scheme utilized, an additional analysis was considered. Since  $P-\delta$  effects are only captured when decomposing an element into sub-elements, a distributed plasticity element was analyzed with a higher resolution integration scheme. An element with four sub-elements and four integration points per element was analyzed with P-delta effects for column 123007, since P-delta effects would have the largest consequence on this column. The difference in integration resolution between this analysis and the previous one using three sub-elements and three integration points is shown in Figure 5-18. The two analysis results are compared to each other in Figure 5-19. It can be seen that the higher resolution does not make a significant difference in the results; therefore the resolution of the previous analyses was determined to be adequate.

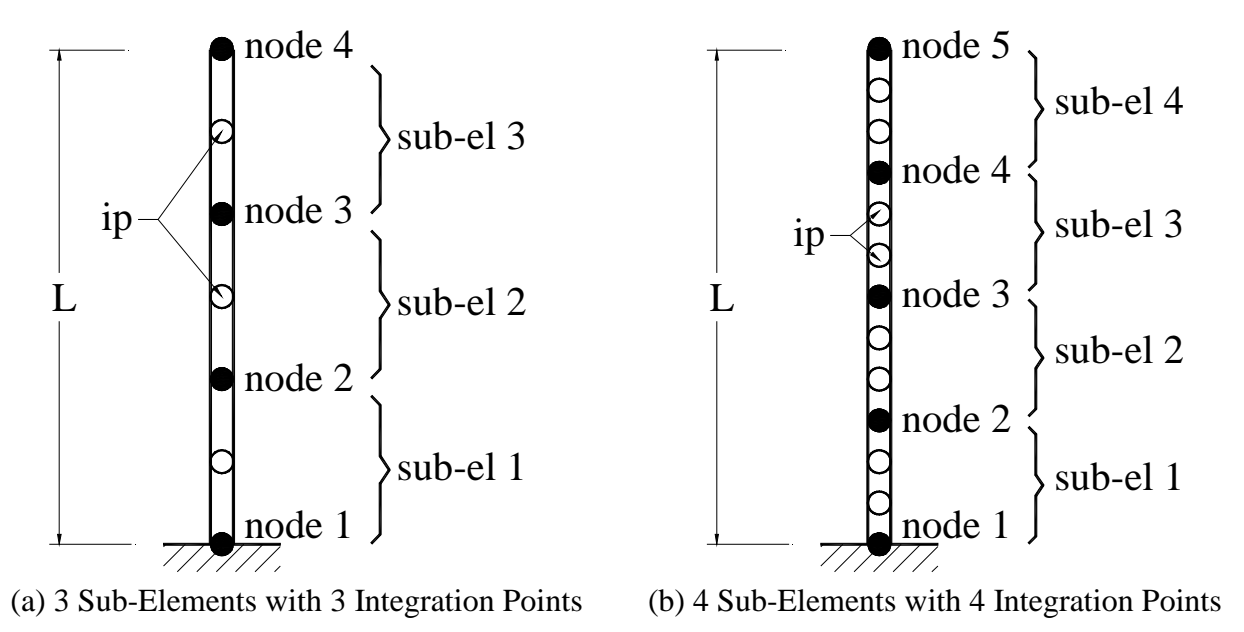


Figure 5-18: Distributed Plasticity Integration Schemes

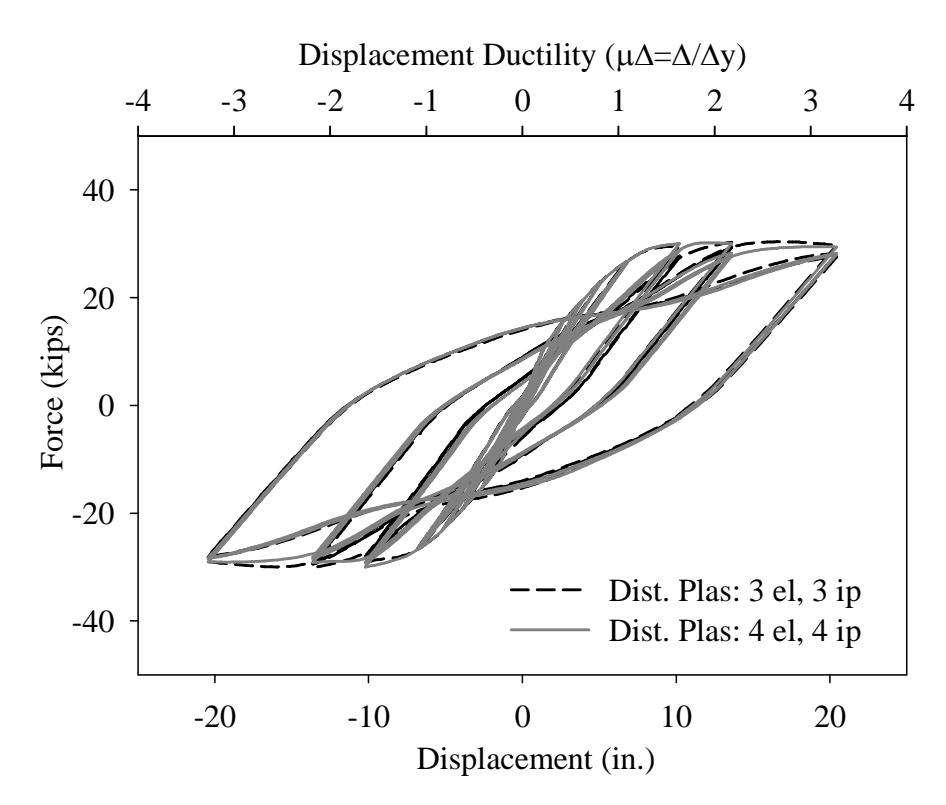


Figure 5-19: 123007 Distributed Plasticity Integration Schemes with P-Delta

In summary, using the corrected force data from each test and comparing it to analysis results considering P-delta effects is the most accurate and appropriate approach for predicting these column's responses. However, due to the evidence shown in this section, using the "corrected" approach does not offer any improvement in the predicted global response. Therefore the uncorrected (no P-delta effects) results will be used for further discussion in this thesis, which also offers more consistency to work completed by other researchers. It is however noted that P-delta effects have a noticeable effect on flexural columns, particularly with very high aspect ratios. It is thus recommended that these effects be considered carefully in the design and analysis of slender columns.

## **5.4** Local Response

While global responses give an indication of overall element performance, local responses, which better relate to damage, offer further insight into the suitability of an element for PBD. Numerical models are typically calibrated for global response, yet local responses are necessary for predicting the onset of intermediate limit states. This section presents analysis results from the simulations using the distributed plasticity element and compares them to each of the five column's curvature and displacement profiles at various ductility levels. Since the distributed plasticity element allows the user to extract data at each node and integration point along the length, it is the most appropriate numerical model available for obtaining inelastic local response profiles. Lumped plasticity elements utilize internal integration points (see Section 2.4.1) to monitor element behavior, however these points are not user-defined as individual fiber sections and output data is not available in the OpenSees platform. This limitation is a notable disadvantage of the lumped plasticity element for extracting information needed for PBD. Therefore, the distributed plasticity element is currently the most accurate tool available for extracting intermediate local behaviors and was thus chosen to compare against the experimental data in the following discussion.

#### **5.4.1** Curvature

Curvature profiles were created by averaging the experimental values from the peak push and pull directions at each ductility level. Since base curvature values are typically not included in experimental data due to unreliable measurements, base curvatures were estimated from the average profiles. A least-square linear fit of the data in the plastic curvature region was used to extrapolate the curvature at the base of the column. This data was then compared to the positive peak values determined from an OpenSees analysis.

The resulting profiles are shown in Figure 5-20 through Figure 5-24. Profiles are shown in graph (a) for the first two or three ductility levels past first yield, while profiles in graph (b) show the higher ductility levels. The resulting trends in curvature profiles are different for various aspect ratios. For aspect ratios 4 and 6, base curvatures are underestimated by the OpenSees analysis for lower ductility levels; however, they are overestimated for higher ductility levels. In the case of column 415, a jump in the experimental base curvature appears between  $\mu\Delta=2$  and  $\mu\Delta=3$ . For column SRPH1, this jump in curvature distribution occurs between  $\mu\Delta=4$  and  $\mu\Delta=6$ . The analysis also fails to capture intermediate curvature values for column SRPH1; as the predicted curvatures are very low above the base, indicating less spread of plasticity than the experimental data indicates. The performance of curvature profile prediction for remainder of the columns was random. The predicted curvatures for column 815 have the best comparison to the experimental data, slightly overestimating curvatures between  $\mu\Delta=1$  and 2 and with very close prediction at  $\mu\Delta$ =3 and 5. The prediction of Column 1015 was good for plastic curvatures at  $\mu\Delta$ =1 and 1.5; however, the analysis values begin to deviate after this point. At  $\mu\Delta=2$  through  $\mu\Delta=5$ , the base curvatures are underestimated by the analysis, but the spread of plasticity is overestimated, since the intermediate values are much higher than indicated by the experimental data. Results for column 123007 are in good correlation with intermediate curvatures; however, the base curvatures were overestimated by the OpenSees analysis. Overall, these results indicate difficulty in predicting inelastic curvature distributions, especially at higher ductility levels, with random trends between aspect ratios.

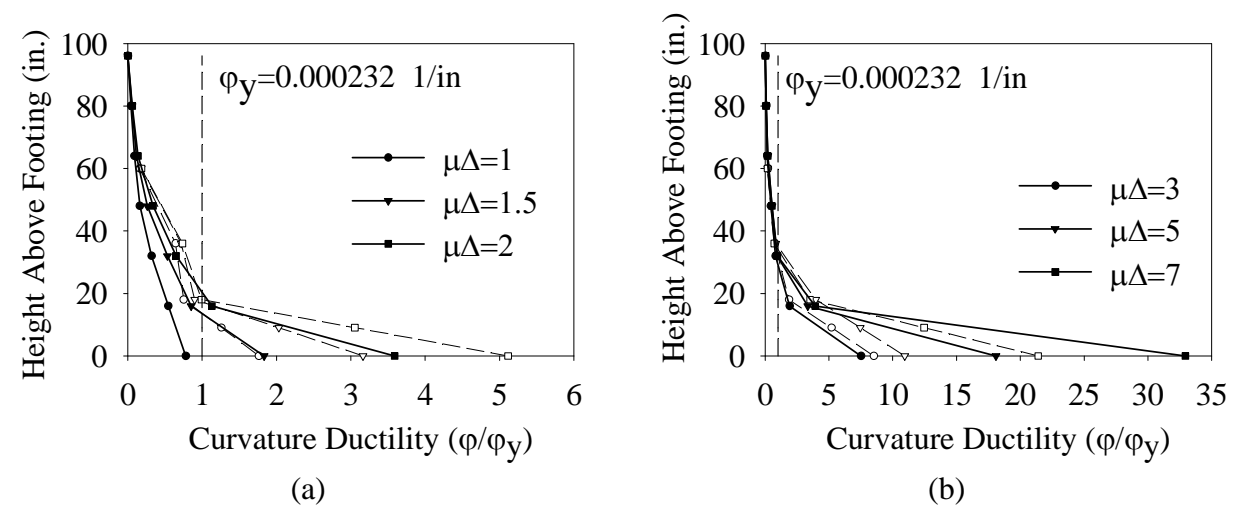


Figure 5-20: 415 Curvature Profiles (Dashed=Exp.; Solid=Dist. Plas.)

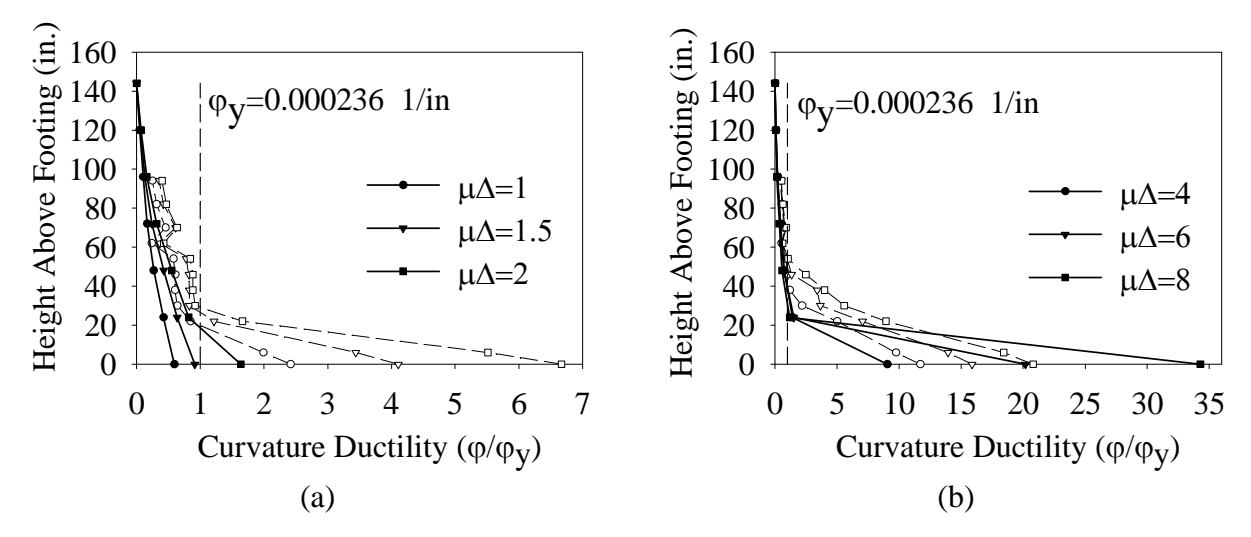


Figure 5-21: SRPH1 Curvature Profiles (Dashed=Exp.; Solid=Dist. Plas.)

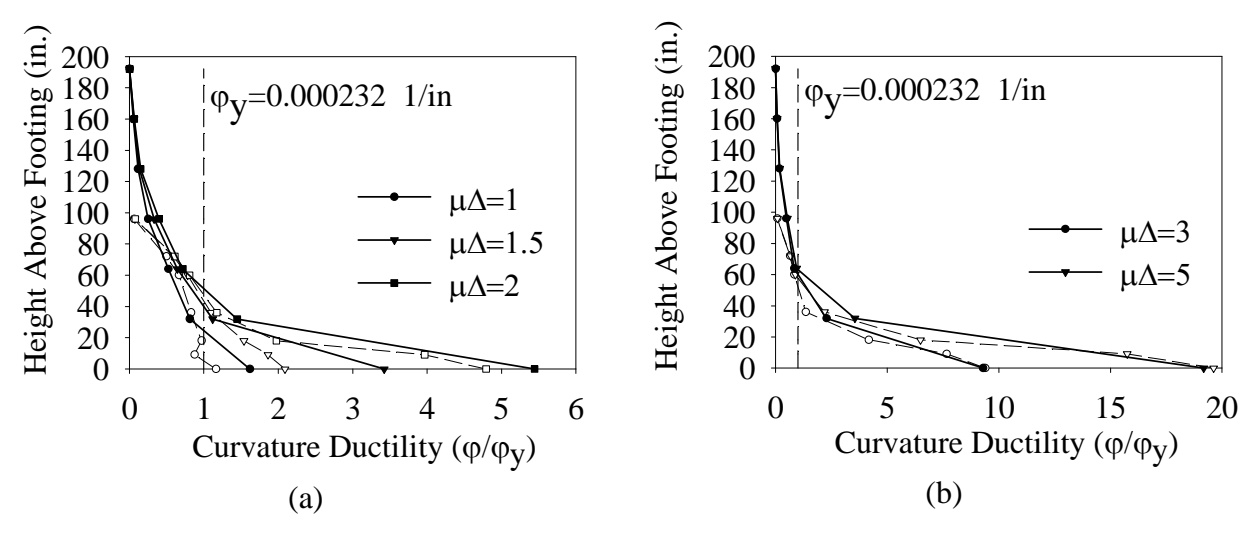


Figure 5-22: 815 Curvature Profiles (Dashed=Exp.; Solid=Dist. Plas.)

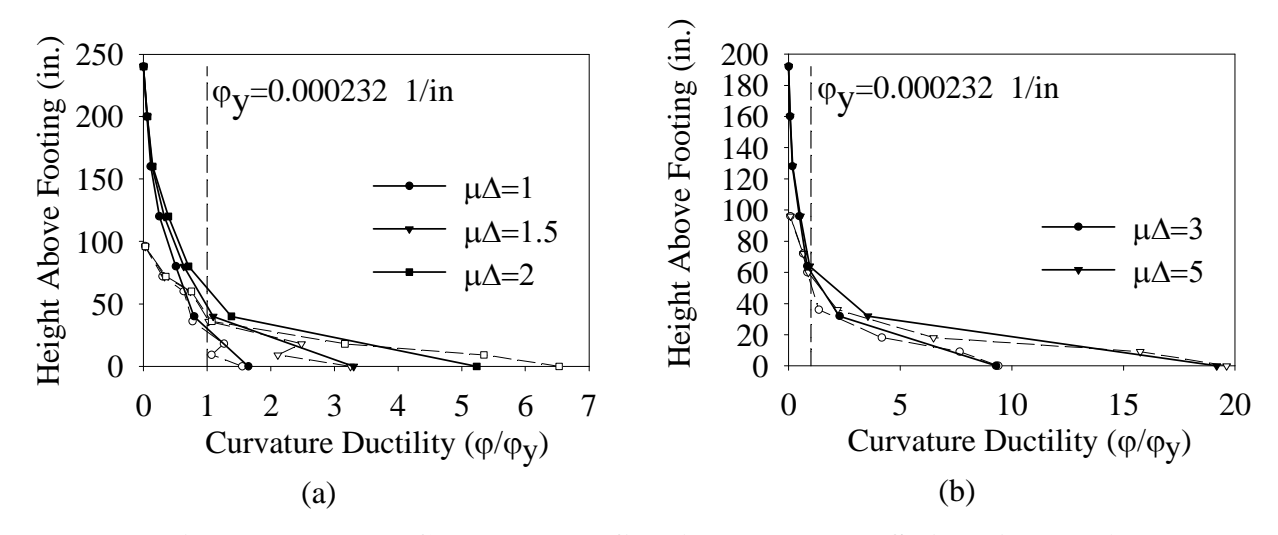


Figure 5-23: 1015 Curvature Profiles (Dashed=Exp.; Solid=Dist. Plas.)

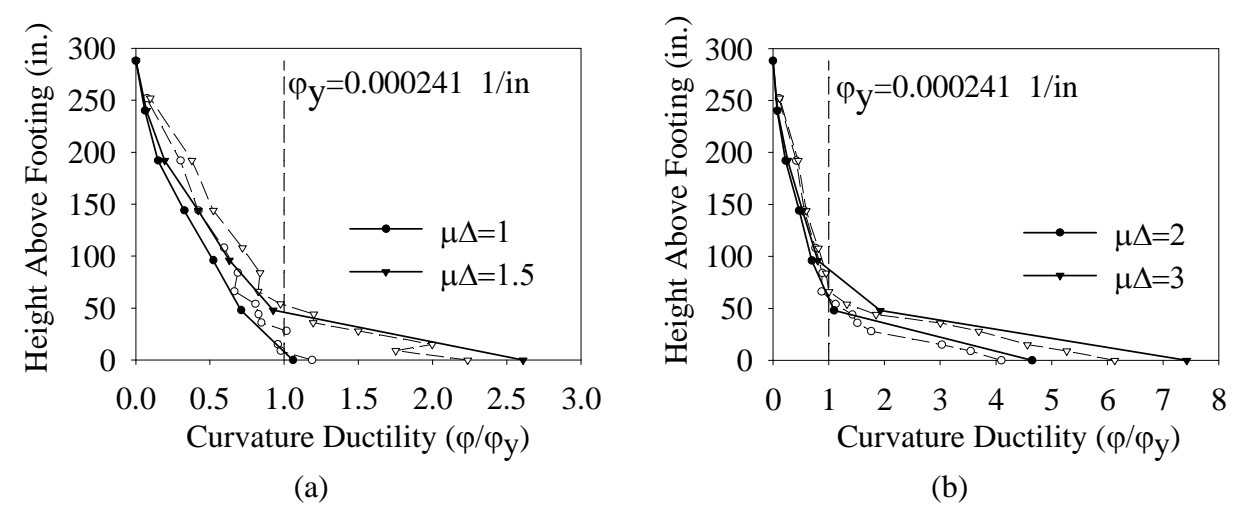


Figure 5-24: 123007 Curvature Profiles (Dashed=Exp.; Solid=Dist. Plas.)

# **5.4.2** Lateral Displacement

Lateral displacement profiles were also extracted from the finite element analyses to compare the displacement shape of each column at various ductility levels. Experimental lateral displacement profiles, like curvature, were created by averaging the displacement in the push and pull directions at each peak level. As previously noted, cyclic analyses were completed by using the target tip displacements reported in the PEER SDP experimental data. The experiment and analysis top displacements were thus equal for each loading level. However, it is the intermediate lateral displacements that were of interest to verify whether the analysis is able to capture the bending within the element, which is related to the spread of plasticity captured by the numerical model. The distributed plasticity element in this case is able to only capture global structural deformation response at element nodes, rather than at all integration points.

The resulting displacement profiles for each column are shown in Figure 5-25 through Figure 5-29 for each ductility level after first yield. For column 415, it can be observed that there is less obvious bending than in the more slender columns; however, the majority of this bending occurs

within approximately 24-inches of the column height. The analysis is this case slightly underestimates the intermediate lateral displacements. The experimental displacement profile for column SRPH1 indicates large bending at a height of about 30-inches, where a kink in the data is observed. This is clearly the transition between the plastic and elastic portions in the column. The analysis, however, does not capture this kink and slightly overestimates the intermediate lateral displacements. The higher aspect ratio columns, (L/D = 8, 10, 12) are better predicted by the analyses, by better capturing the onset of the effect of plastic deformations (i.e., the kink in the displacement profile.) There is some discrepancy at lower heights, most likely due to the lack of nodal output in this region. This lack of data may also be the reason for discrepancy in the lower aspect ratio columns. Since the plastic region in short columns occurs at lesser heights, the discretization for the 415 and SRPH1 columns was unable to capture such behavior. A model with more elements (distributed plasticity) may improve results in this circumstance. In general, the analysis models were able to capture transverse displacements more accurately curvature, which proved difficult to estimate as it depends on localized strains within a fiber section.

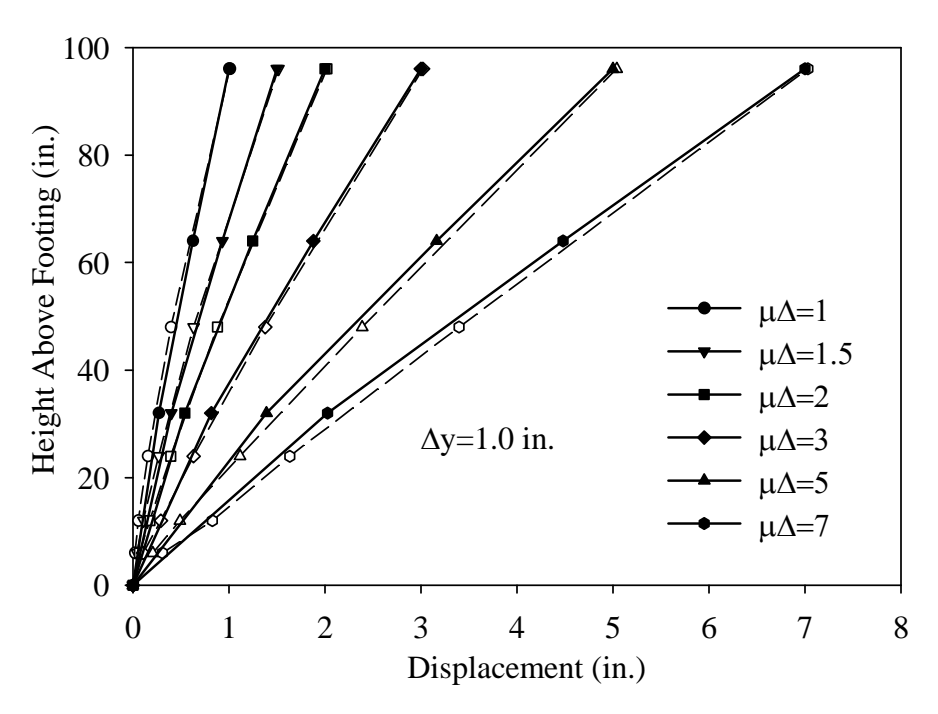


Figure 5-25: 415 Displacement Profiles (Dashed=Exp.; Solid=Dist. Plas.)

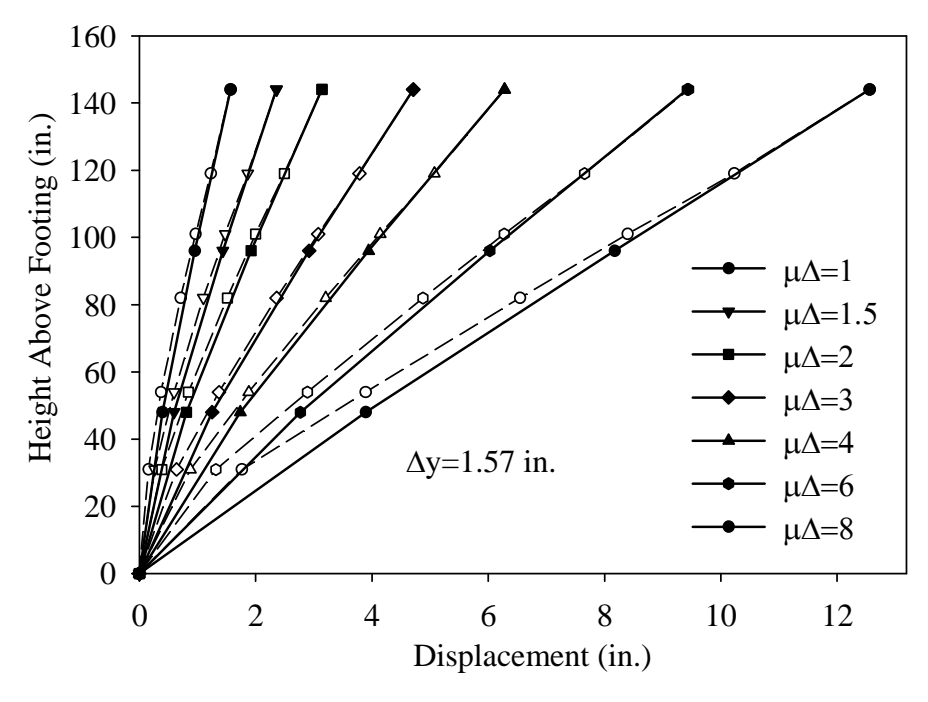


Figure 5-26: SRPH1 Displacement Profiles (Dashed=Exp.; Solid=Dist. Plas.)

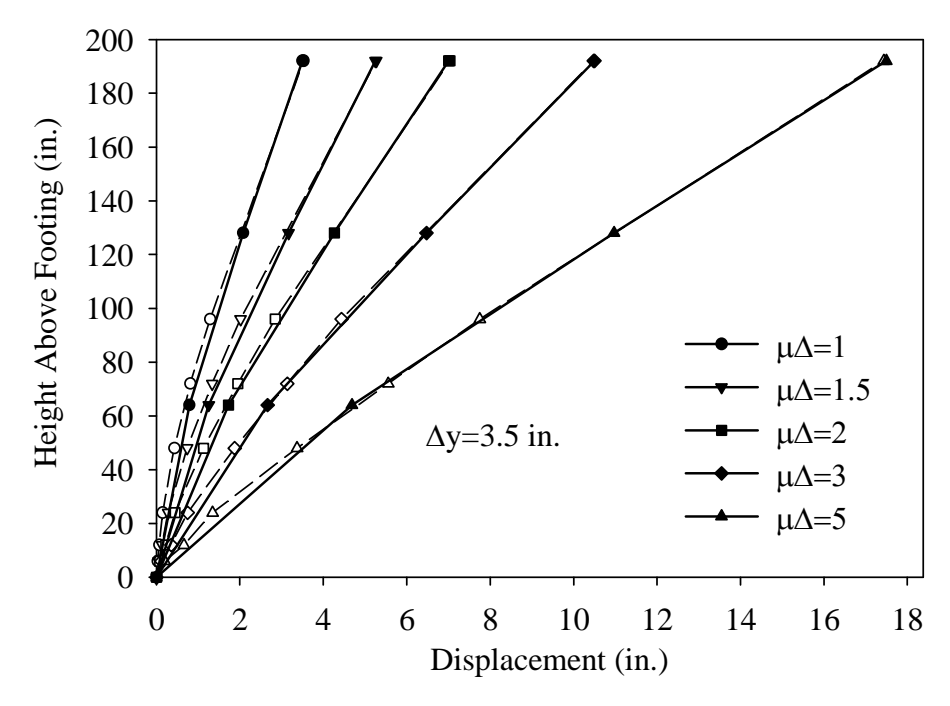


Figure 5-27: 815 Displacement Profiles (Dashed=Exp.; Solid=Dist. Plas.)

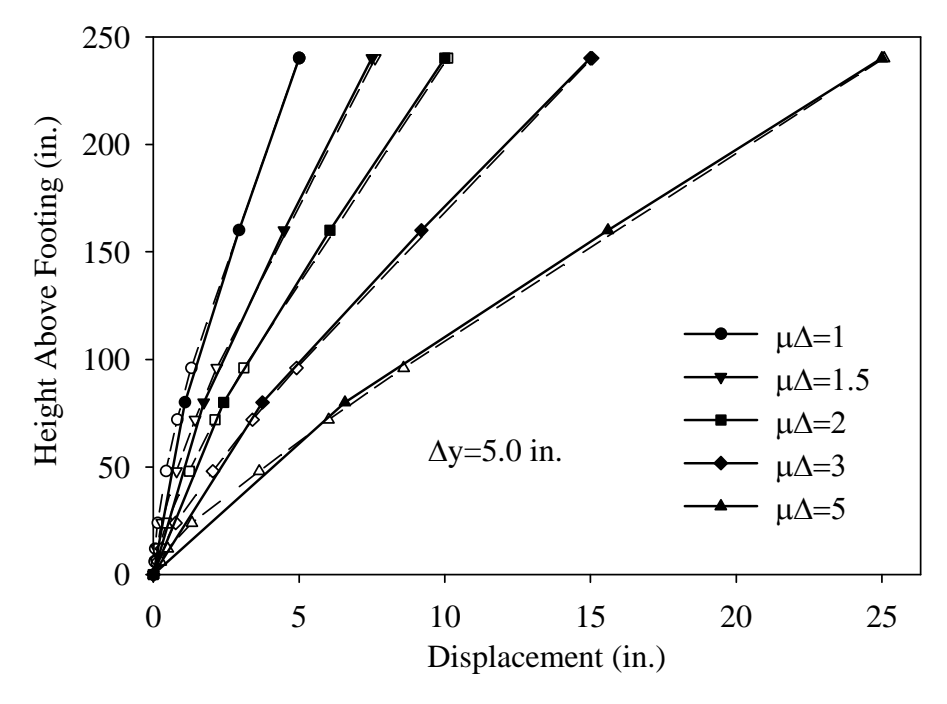


Figure 5-28: 1015 Displacement Profiles (Dashed=Exp.; Solid=Dist. Plas.)

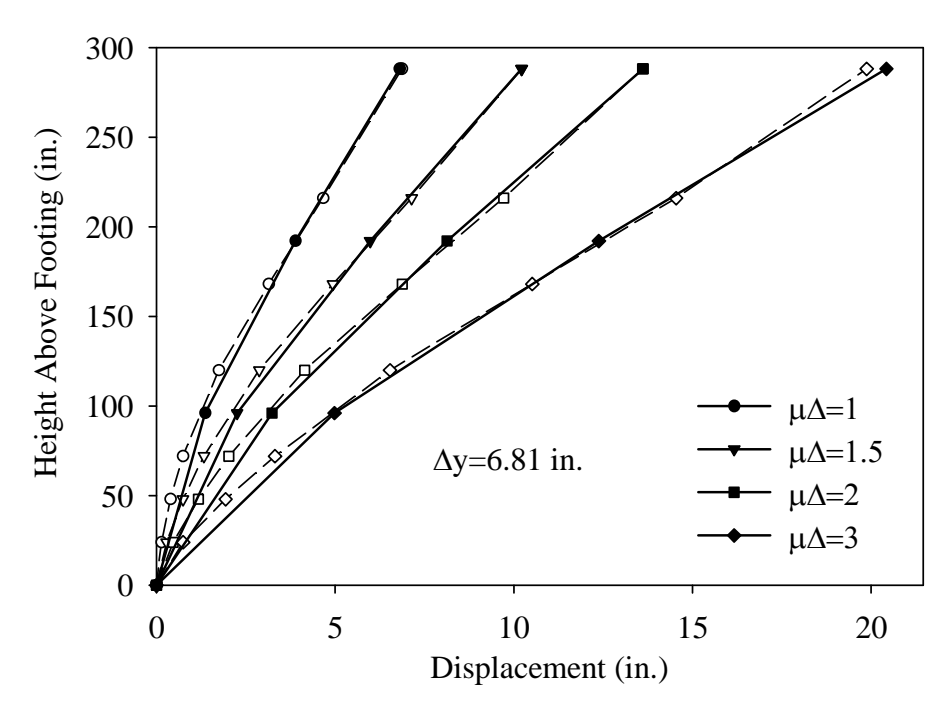


Figure 5-29: 123007 Displacement Profiles (Dashed=Exp.; Solid=Dist. Plas.)

# 5.5 Spread of Plasticity

To assess the spread of plasticity in each column, experimental data was compared to the simulation results by utilizing the shear crack model proposed by Hines et al. (2004), see Section 2.3.1. The predicted spread of plasticity was found by plotting the plastic hinge region length, L<sub>pr</sub> found by Equation 2-13 against the curvature ductility. The experimental spread of plasticity was determined from the average curvature profiles given in the previous section. L<sub>pr</sub> was taken as the height at which the curvature profile of each ductility level crossed the yield curvature limit. Curvature ductility was then taken as the ratio of the estimated base curvature (see Section 5.4.1) at each level to yield. The resulting comparisons of the experimental data to prediction by the Hines shear crack model are shown in Figure 5-30 through Figure 5-34, alongside the experimental curvature profiles. Columns of aspect ratio 4 and 6 show some random scatter;

however the overall trend in spread of plasticity is similar to the prediction, with the extent of plasticity growing steadily for increasing curvature ductility. Conversely, the experimental data of columns 815, 1015 and 123007 shows a large increase in the extent of plasticity just after yield, but the data indicates a less rapid increase of the plastic region at higher ductility levels. The decreasing rate of  $L_{pr}$  increase seems to occur more quickly as aspect ratio increases, which is not captured by the analytical model. The cause for the noted effects for slender columns is attributed to P-delta effects. It is thought that a very slender column will experience large inelastic curvatures very quickly, however once displacements become large, it takes less energy for the column to displace by the overturning P-delta effects, rather than increase the extent of yielding along the length. Similarly, P-delta effects may likely be the reason for the experimentally observed higher rate of growth of  $L_{pr}$  at low ductility levels, which also cannot be captured by the analytical model. This indicates that the spread of plasticity in slender columns increase rapidly at low ductility levels but will not spread much at high ductility demands.

The Hines et al. (2004) model for spread of plasticity is found to be very promising for use in PBD since it captures the growth of the plastic region quite well. The link of this model with a simplified elasto-plastic, i.e., lumped-plasticity, model with a variable plastic hinge length could be a valuable tool for PBD. However, refinements of the Hines et al. spread of plasticity model seem to be needed to properly capture the effects of column aspect ratio.

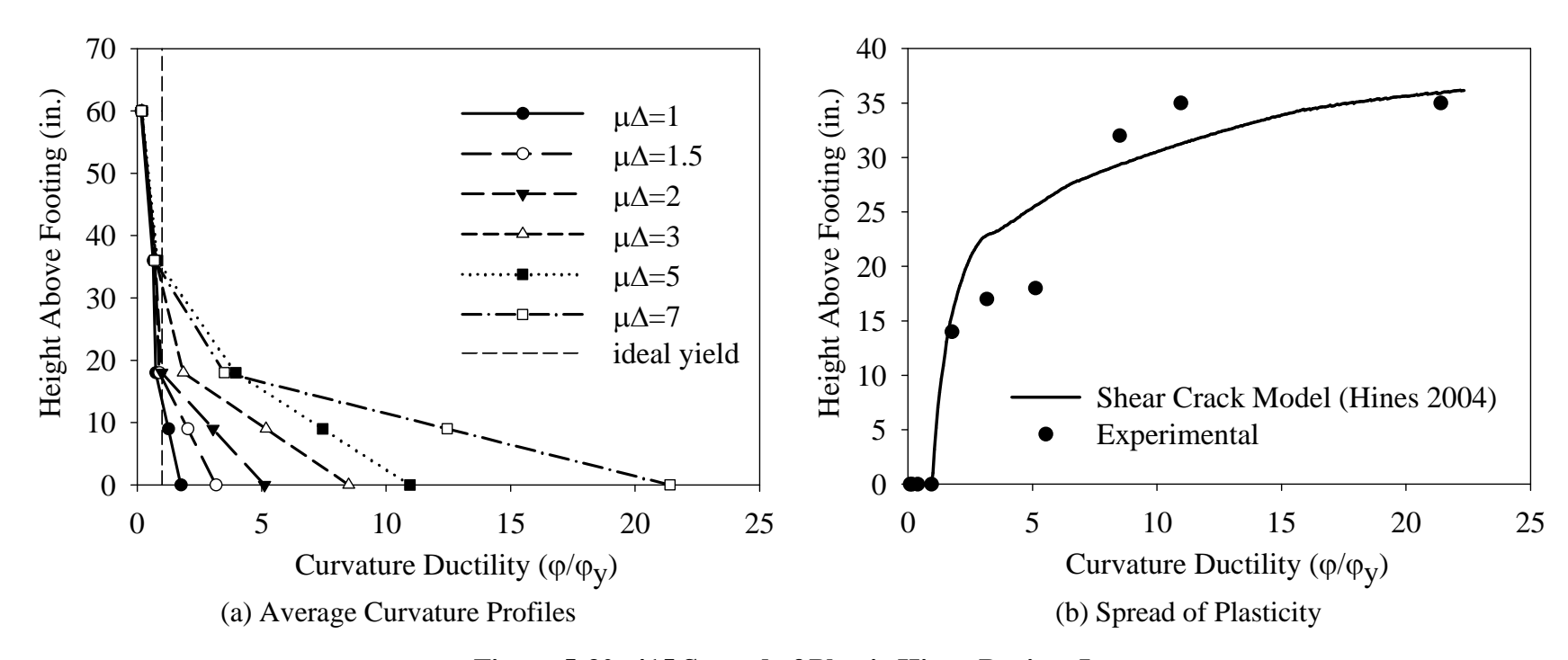


Figure 5-30: 415 Spread of Plastic Hinge Region,  $L_{pr}$ 

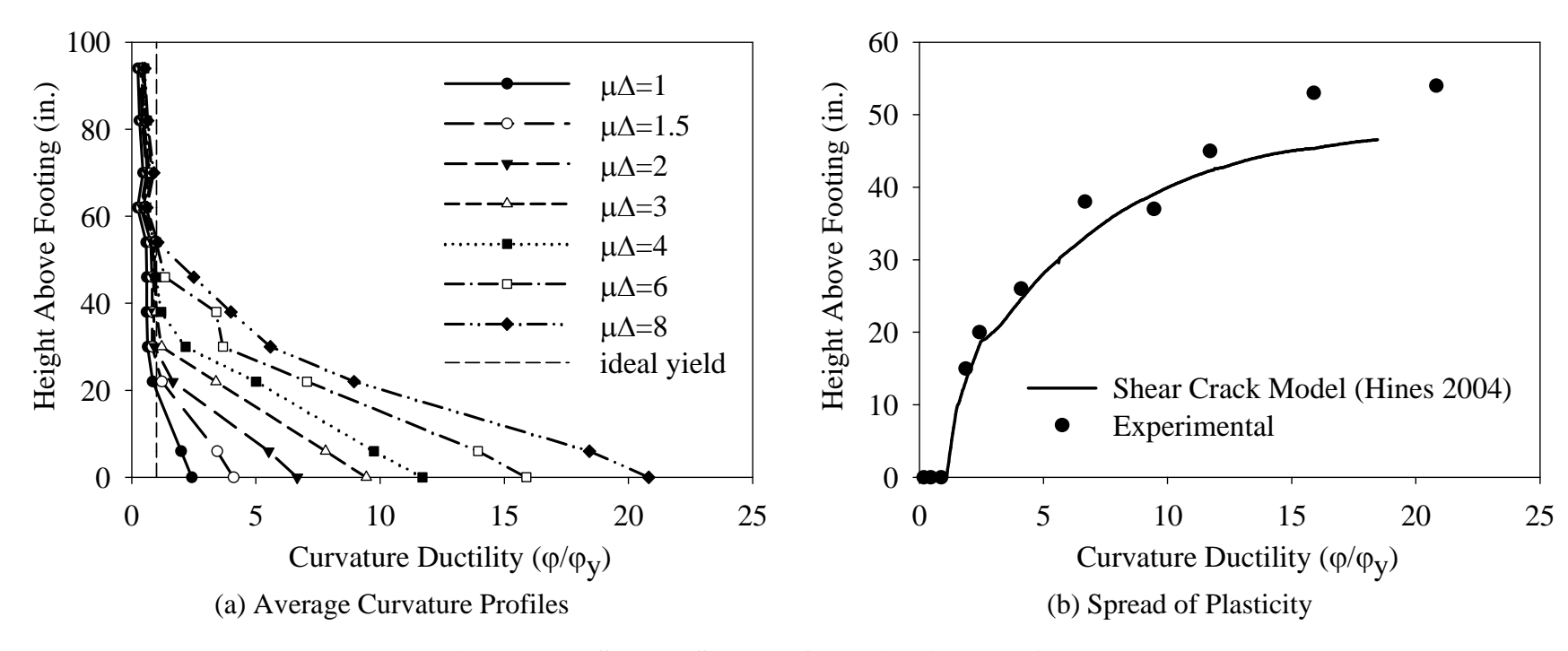


Figure 5-31: SRPH1 Spread of Plastic Hinge Region,  $L_{pr}$ 

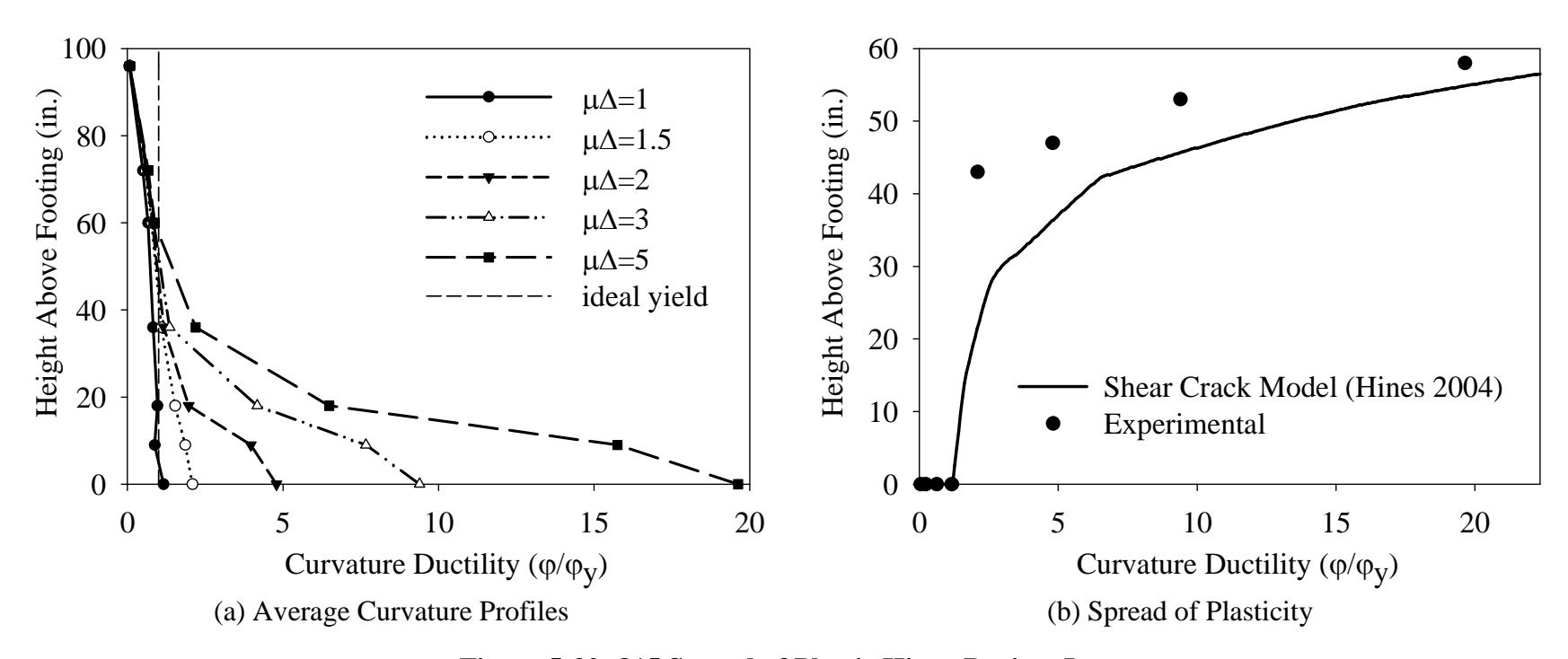


Figure 5-32: 815 Spread of Plastic Hinge Region,  $L_{pr}$ 

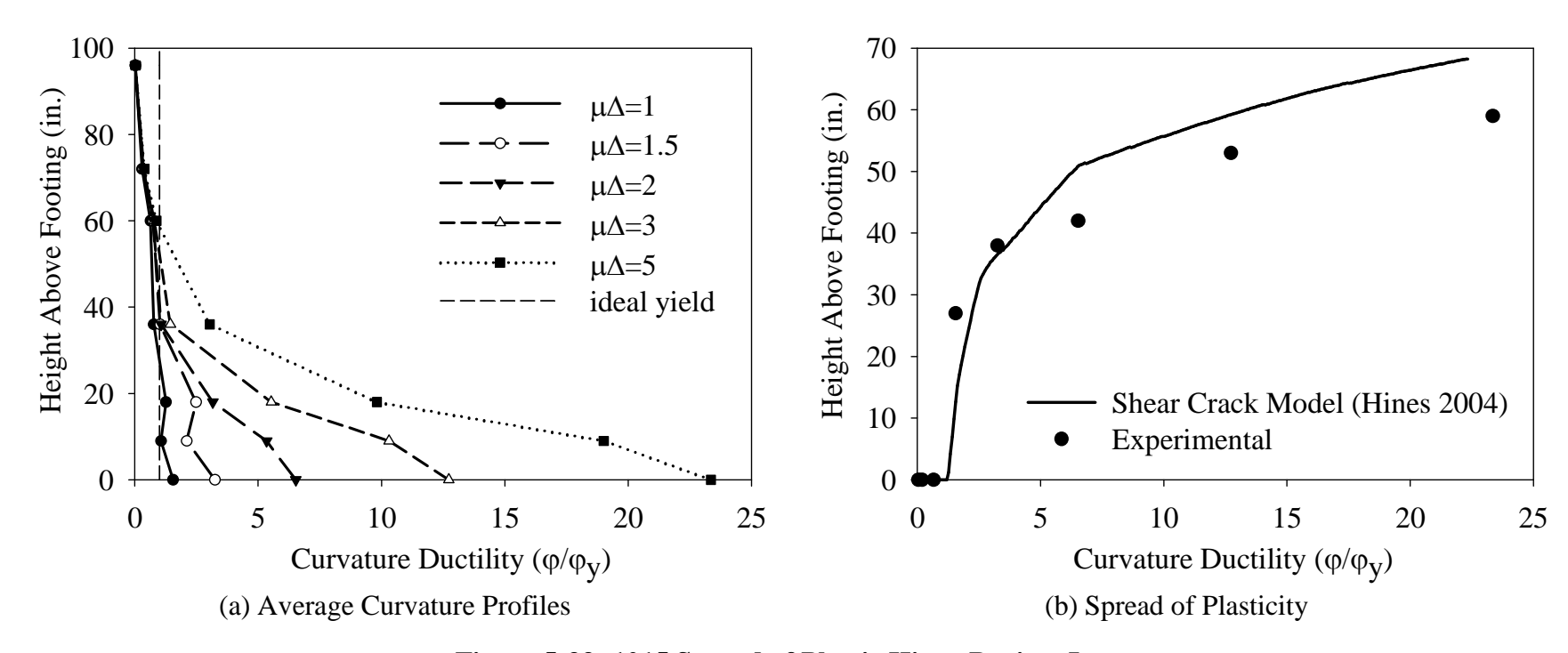


Figure 5-33: 1015 Spread of Plastic Hinge Region,  $L_{pr}$ 

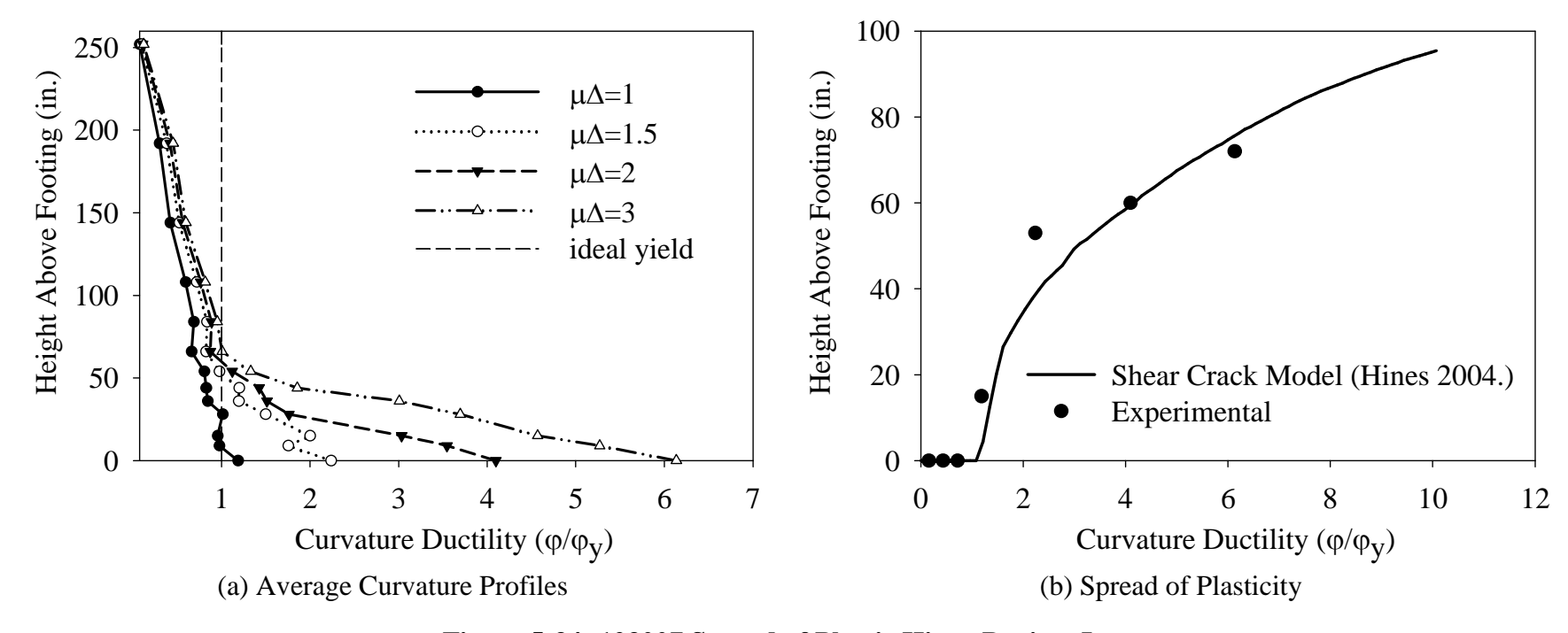


Figure 5-34: 123007 Spread of Plastic Hinge Region,  $L_{pr}$ 

The value of  $L_{pr}$  in the Hines model may be related to the plastic hinge length,  $L_p$  used for lumped plasticity models. According to Hines et al. (2004) the relation is as follows:

$$L_p = \frac{L_{pr}}{2} + L_{sp}$$
 5-5

where  $L_{sp}$  in this case is the strain penetration component given by Priestley et al. (1996), see Equation 2-8. In this manner, the trend of the plastic hinge by Hines may be compared to other models. In order to show the difference in assumptions, the plastic hinge length from the Hines et al. (2004) model is compared to that proposed by Berry et al. (2008) in Figure 5-35. The comparison is shown for column 815; however, it was found to be similar for all five columns discussed in this chapter. Since the assumptions behind the two L<sub>p</sub> models are quite different (i.e., constant vs. linear curvatures and constant vs. varying L<sub>p</sub>), they cannot be directly compared. To compare the use of the plastic hinge length for all columns the calculated ultimate displacements as proposed by Priestley, Berry and Hines are shown in Table 5-3. Two values are given for the Priestley and Berry models to show the difference between the ultimate displacement predicted by the OpenSees monotonic force-displacement analyses using the lumped plasticity element and that using an elasto-plastic analysis (according to Equation 2-2 where  $\Delta_p$  is according to Equation 2-7). It is seen in Figure 5-30 through Figure 5-34 that although the Hines model more accurately predicts the spread of plasticity and assumes a more realistic plastic hinge (see Figure 5-35), the Berry model still best predicts ultimate displacement, as shown in Table 5-3. The reason for this is that the Berry model contains two independent variables  $(L_p \text{ and } \phi_p)$  that may be incorrect separately but are calibrated together to obtain a correct  $\Theta_p$ , which leads to the correct displacement values.

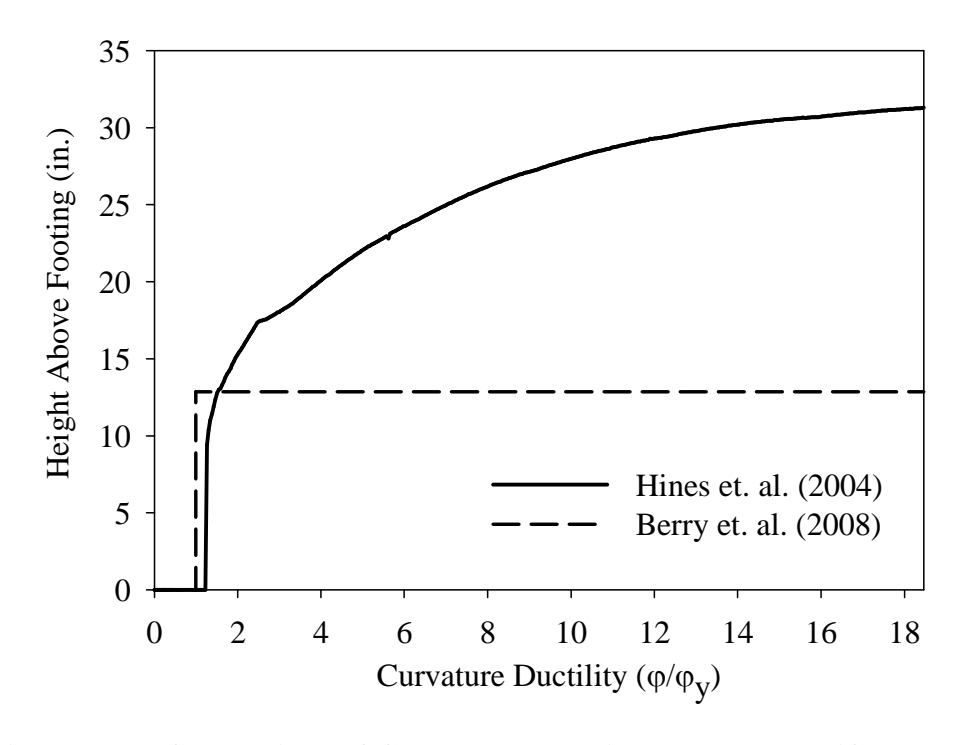


Figure 5-35: Comparison of Constant vs. Variable  $L_p$  Models (Column 815)

**Table 5-3: Comparison of Predicted Ultimate Displacement (in.)** 

L/D	Exp.	Berry			Priestley			Hines	
		FEM*	EP <sup>#</sup>	% Error	FEM*	EP <sup>#</sup>	% Error	SCM <sup>+</sup>	% Error
4	5.3	6.2	6.6	25.4	8.5	8.6	62.7	10.5	98.3
6	12.6	12.3	13.4	6.3	18.2	18.7	48.2	9.6	24.2
8	17.5	17.9	20.0	14.1	27.0	28.1	60.7	31.0	77.0
10	25.0	25.8	29.1	16.3	39.8	41.9	67.7	45.7	82.7
12	N/A	42.7	46.1	N/A	65.0	68.5	N/A	N/A	N/A

\*FEM: Lumped plasticity element model

<sup>&</sup>lt;sup>#</sup>EP: Elasto-plastic analysis (Eqns. 2-2, 2-3 and 2-5 to 2-7); used for error calculations

<sup>\*</sup>SCM: Shear crack model (Eqn. 2-13)

#### **5.6** Performance of Predicted Limit States

Prediction of the limit states discussed in Chapter 4 is revisited in this section in further detail for the five selected columns. Limit states are defined according to the previous criteria (see Section 4.4.1), and are explored for various plastic hinge models, numerical methods and load conditions.

First explored are graphical representations of the plastic hinge model evaluations completed in Chapter 4. The monotonic envelope for each plastic hinge model is plotted against the experimental response of columns with L/D = 4, 6, 8 and 10. Column 123007 is not shown since it is not part of the PEER SPD. Figure 5-36 shows the comparison of each model in addition to the predicted limit state displacements. It is shown with greater distinction that the Berry et al. plastic hinge model best represents not only the global behavior of each column, but the intermediate limit states as well. The Priestley plastic hinge model overestimates the ultimate displacement in each case, which in turn tends to overestimate limit states such as bar buckling or bar fracture. While the Corley model shows ultimate displacement prediction similar to the Berry model, it tends to predict intermediate limit states more similarly to the Bayrak plastic hinge model, which shows relatively poor performance in comparison to the other models. The Berry and Priestley plastic hinge models are compared numerically in terms of percent error in Table 5-4, where the model with the least error is shaded. Based on these results, the Berry plastic hinge model was determined to be the most suitable for limit state prediction and was used for the lumped plasticity element models in other evaluations presented later in this chapter.

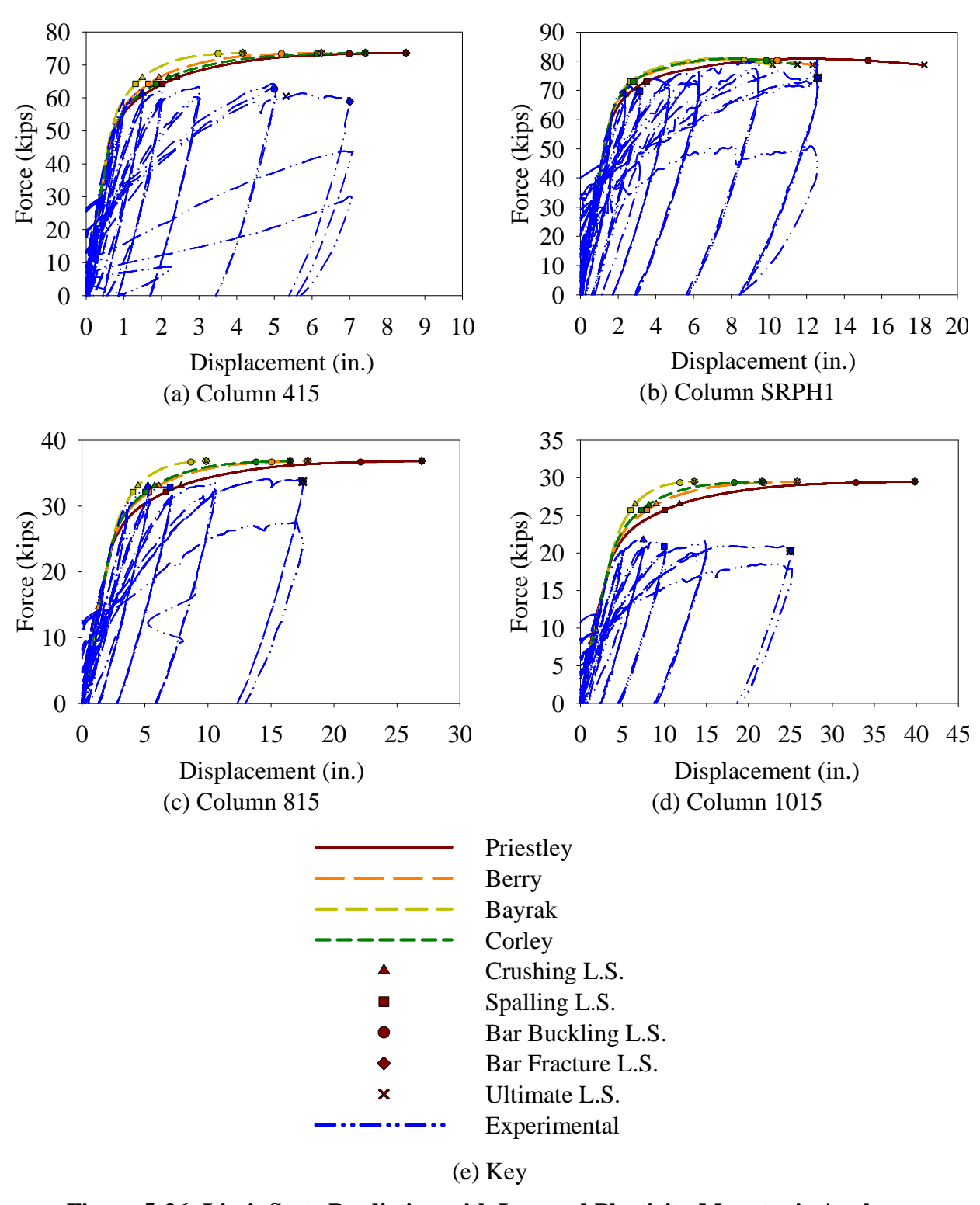


Figure 5-36: Limit State Prediction with Lumped Plasticity Monotonic Analyses

**Table 5-4: Mean Percent Limit State Error for Case Study Columns** 

L/D	4		6		8		10		Average	
	Priestley	Berry								
Crushing	61	40	44	19	51	16	57	20	53	24
Spalling	N/A	N/A	12	8	5	24	0	21	6	18
Buckling	40	1	21	17	26	14	31	13	30	11
Fracture	21	13	N/A	N/A	54	2	59	3	45	6
Ultimate	60	15	45	2	54	2	59	3	54	6
Total							38	13		

Limit state predictions in cyclic analyses were performed next for each column and the results are presented in Figure 5-37 through Figure 5-41. Three cases are presented for each column: graph (a) shows the limit state predictions using a lumped plasticity element that utilized the Berry plastic hinge model; graph (b) shows the limit state predictions using a distributed plasticity element; and graph (c) shows the limit state predictions using a distributed plasticity element in an analysis that takes P-delta effects into account. When comparing the lumped plasticity results to those in the monotonic plots (Figure 5-36), it is seen that results are slightly different, however there is no apparent trend in these differences nor does the cyclic analysis indicate better or worse results in overall limit state prediction. By comparing graphs (b) and (c) of Figure 5-37 through Figure 5-41, it is seen that displacement at which each limit state is predicted is nearly identical. This indicates that although P-delta effects have a significant effect on a column's global response, intermediate displacement limit states are not significantly affected. Interest therefore lies in comparing the lumped plasticity and distributed plasticity results in graphs (a) and (b), respectively. Both elements give similar results, yet the lumped plasticity model shows slightly more accuracy across limit states. This observation is verified numerically by comparing the error for each model. Table 5-5 gives the error produced by each model at the different limit states. It is seen that the concrete crushing limit state has the highest error in prediction by both models, however the distributed plasticity error is almost double that of the lumped plasticity model for this damage state. Intermediate limit states, i.e., spalling and buckling, show less error and are very similar between the two numerical models. Fracture and ultimate displacement, on the other hand are predicted very well by the lumped plasticity model, with about 15% less error than the distributed plasticity model. This is likely due to the fact that the plastic hinge model by Berry was specifically calibrated to reduce error in bar buckling and

ultimate displacement. The overall average error for each element is given in Table 5-6, showing 14% total error for the lumped plasticity model and 17% error for the distributed plasticity model. The total average error in prediction for varying aspect ratio is also given in Table 5-6. It is shown that columns 415 and 815 have the smallest percent error while the error in columns SRPH1, 1015 and 123007 are highest.

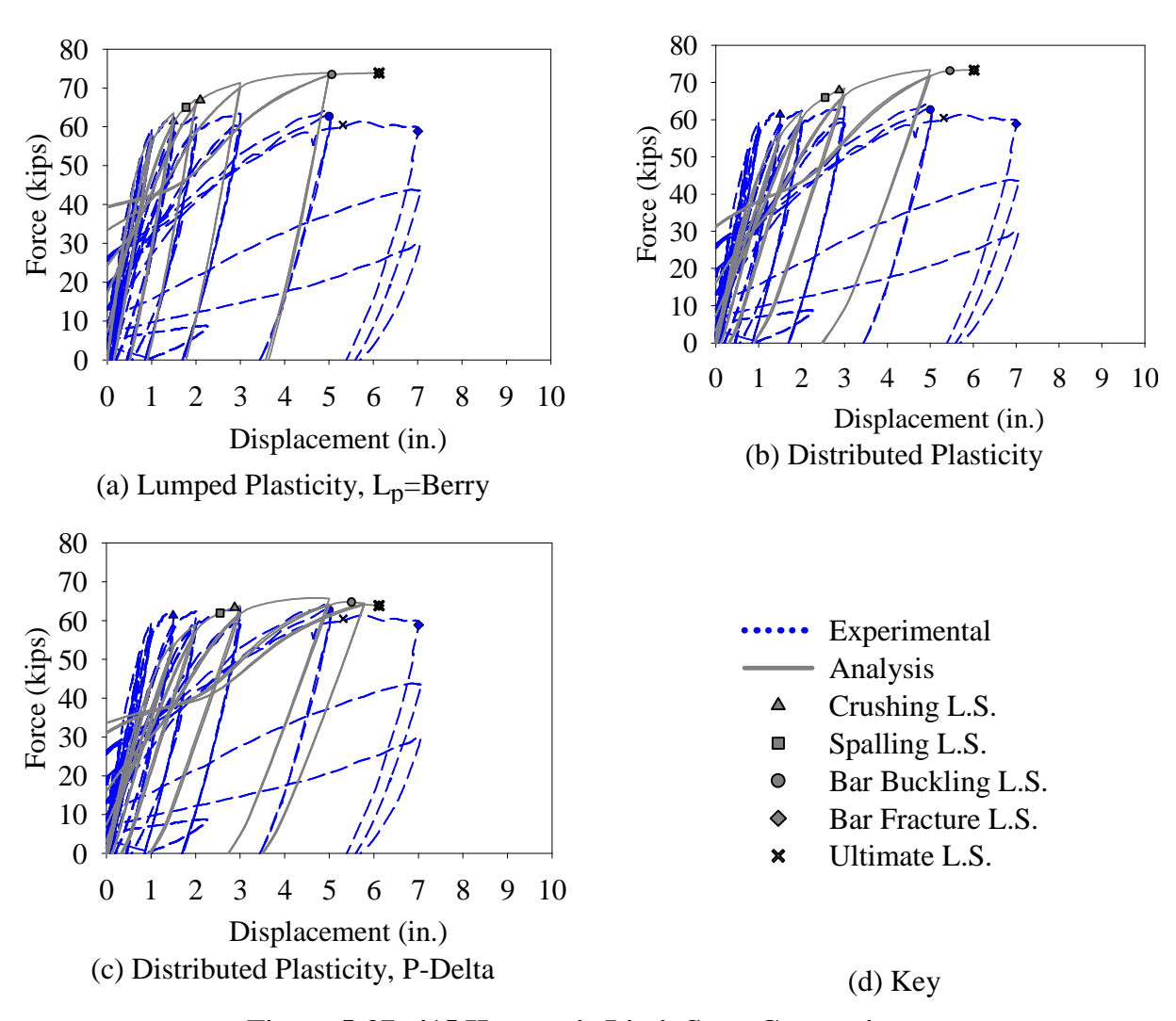


Figure 5-37: 415 Hysteretic Limit State Comparisons

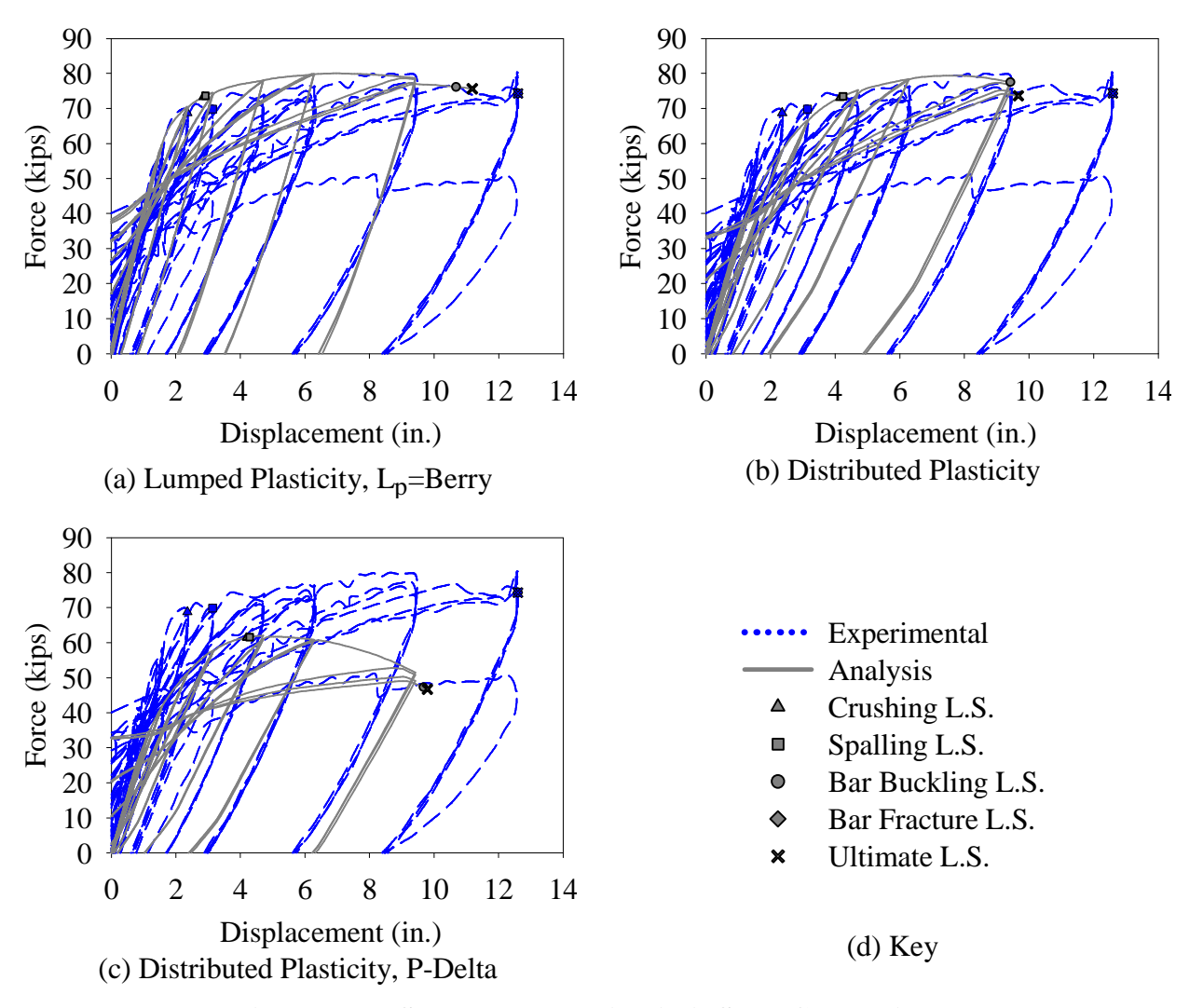


Figure 5-38: SRPH1 Hysteretic Limit State Comparisons

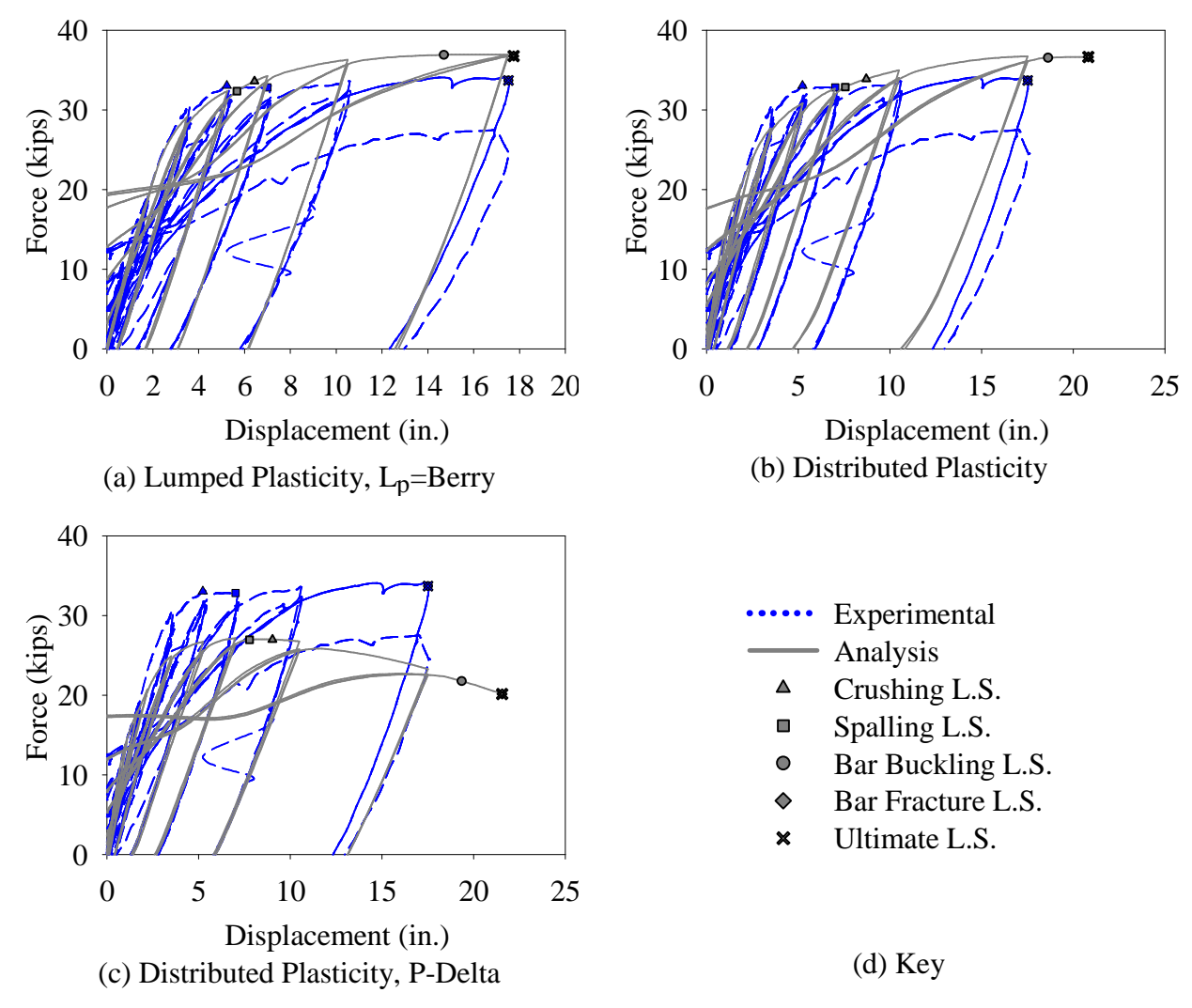


Figure 5-39: 815 Hysteretic Limit State Comparisons

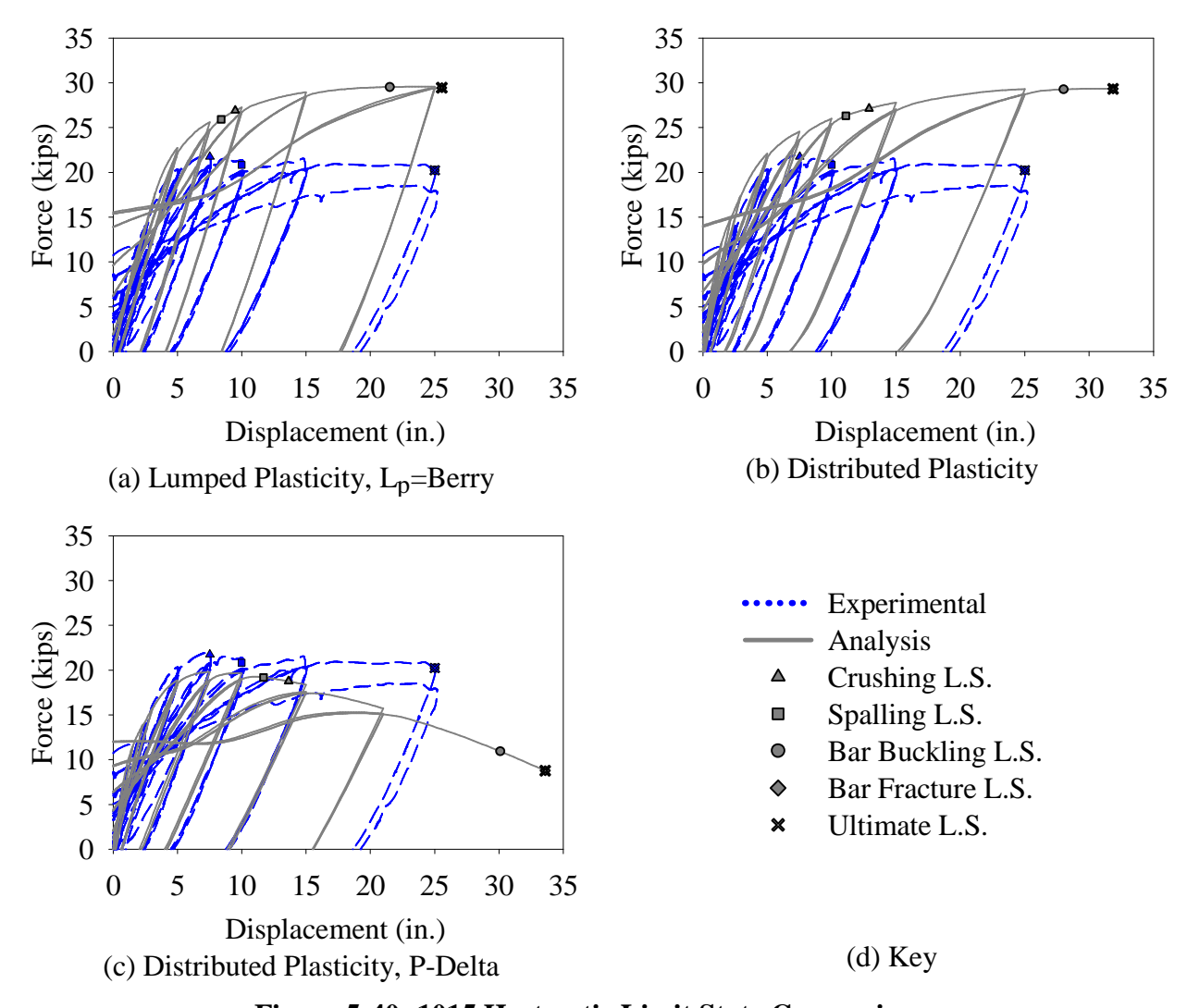


Figure 5-40: 1015 Hysteretic Limit State Comparisons

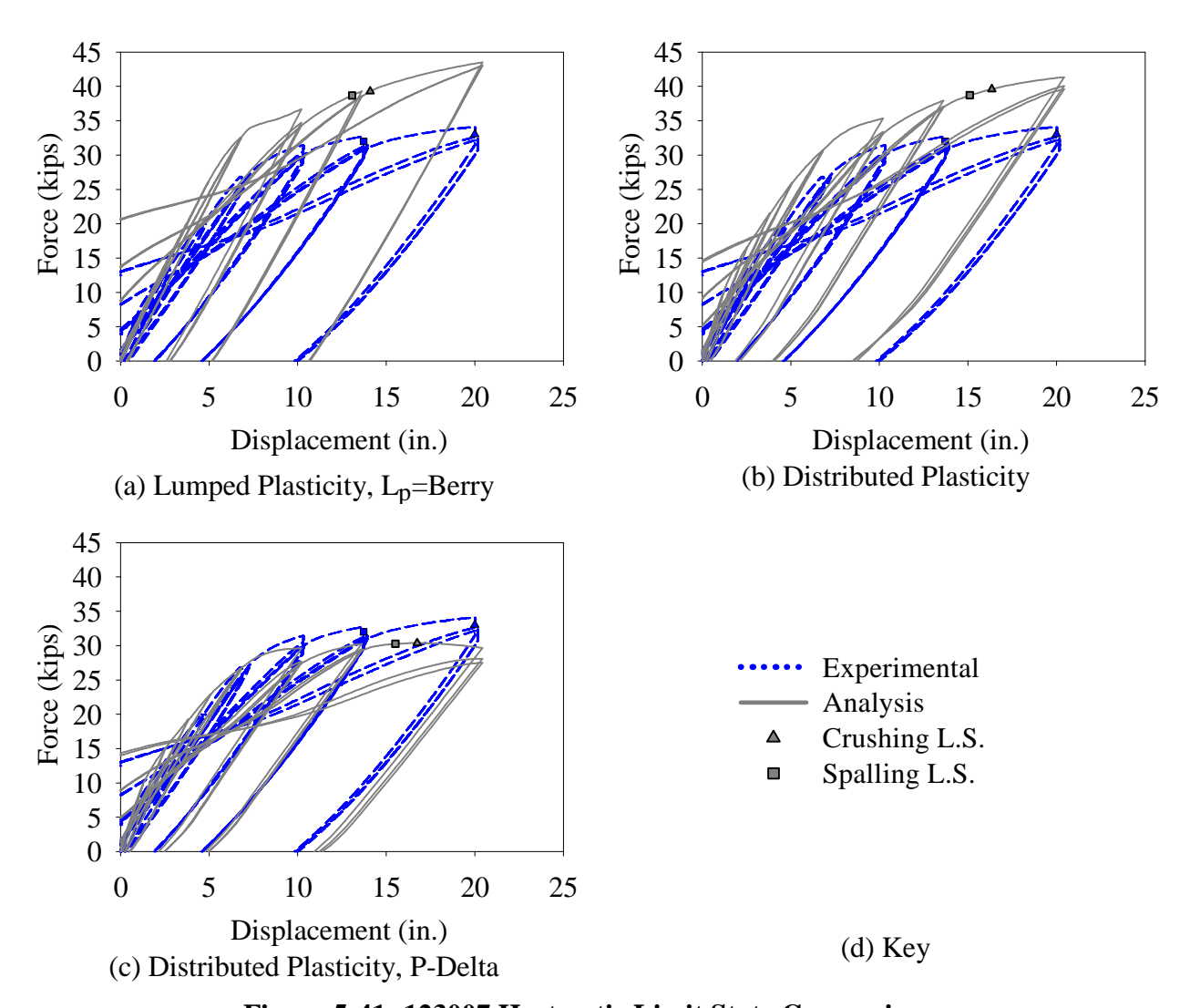


Figure 5-41: 123007 Hysteretic Limit State Comparisons

**Table 5-5: Error in Limit State Prediction for Cyclic Analyses** 

CRUSHING L.S.								
L/D	Lump. Plas	Dist. Plas.						
4	0.40	0.92						
6	0.21	0.75						
8	0.23	0.66						
10	0.26	0.72						
12	0.53	0.18						
Average	0.33	0.65						
SPALLING L.S.								
4	N/A	N/A						
6	0.07	0.35						
8	0.19	0.08						
10	0.16	0.11						
12	0.39	0.10						
Average	0.20	0.16						
BA	BAR BUCKLING L.S.							
4	0.01	0.09						
6	0.15	0.25						
8	0.16	0.06						
10	0.14	0.12						
12	N/A	N/A						
Average	0.12	0.13						
BA	R FRACTURE	L.S.						
4	0.13	0.14						
6	N/A	N/A						
8	0.01	0.19						
10	0.02	0.27						
12	N/A	N/A						
Average	0.05	0.20						
ULTIMATE L.S.								
4	0.15	0.13						
6	0.11	0.23						
8	0.01	0.19						
10	0.02	0.27						
12	N/A	N/A						
Average	0.08	0.21						

Table 5-6: Total Mean Error per Element Type and Aspect Ratio

L/D	Lump. Plas.	Dist. Plas.	Total
4	0.09	0.18	0.13
6	0.15	0.19	0.17
8	0.09	0.14	0.11
10	0.14	0.19	0.17
12	0.20	0.16	0.18
Average	0.14	0.17	0.15

#### **5.7** Relevant Conclusions

Several aspects of column behavior may be observed from the analytical and experimental data presented within this chapter. By exploring several numerical methods, conclusions on the effectiveness of different techniques can be made. Comparisons to several types of output data also allow for conclusions on the effect of slenderness on column behavior and on the abilities of the numerical models. These issues are discussed separately in the following sections.

## **5.7.1** Effect of Element Type

The effect of using different element types to predict column behavior shows significance at both the global and local levels. Global behavior is predicted quite similarly by both the lumped plasticity and distributed plasticity models. The lumped plasticity model tends to show more accurate comparison to the experimental hysteretic behavior at early stages of damage, while the distributed plasticity model tends to be more accurate at later stages of inelastic response. The lumped plasticity model however does not offer the ability to capture local behavior along an element length, making the distributed plasticity model more appropriate for such predictions. The distributed plasticity model showed high accuracy in predicting lateral displacement profiles for all columns; however curvatures distributions proved much more difficult to predict. While

the general shape and trend of the curvature profiles were captured, specific values predicted with the analysis were not found to be consistently reliable. This is due to the fact that localized behavior in a column is controlled by many factors including crack location and localized buckling, making it difficult to predict. Predicting limit states for the benefit of PBD is sporadic for both element types; however the lumped plasticity element using the Berry plastic hinge model shows slightly better results than the distributed plasticity model. Concrete limit states are generally difficult to predict since such damage depends more heavily on material-level characteristics (i.e., concrete mix design and the resulting microstructure) however, spalling proved to be better predicted by the models than crushing. Bar buckling was predicted fairly well by both models, showing similar error. Ultimate conditions however were predicted very well by the lumped plasticity model, and only moderately by the distributed plasticity model. The plastic hinge expression by Berry et al. was calibrated to reduced error in ultimate displacement in modern columns which explains its high performance level. It may therefore be concluded that both the lumped plasticity and distributed plasticity models offer advantages and disadvantages in predicting column behavior.

## 5.7.2 Effect of Aspect Ratio

Identical analyses were performed on five columns of varying aspect ratio. The aspect ratios included represent a wide range, with L/D =4 being the least slender of columns appropriate for flexural response, and L/D =12 being the most slender column tested in an experimental setting (using the data in the PEER PDB as reference.) The effect of slenderness in a column has the greatest consequence in predicting global behavior. It was observed that for very slender columns (L/D =10, 12) P-delta effects control the hysteretic response. While P-delta effects may be taken into account in the analysis, the effect does not seem to be fully captured. There appears

to be additional geometric effects that cause softening in the column and that were not captured by the finite element models evaluated in this study. This trend was also observed by assessing the spread of plasticity in each column, as the  $L_{pr}$  in higher aspect ratio columns tends to increase more rapidly at low ductility levels and decrease its rate of growth at larger levels of ductility demand. This behavior is not captured by the OpenSees distributed plasticity finite element analyses or the Hines shear crack model.

While aspect ratio has a large effect on predicting column force capacity, its effect was not as apparent in predicting local behavior and intermediate limit states. It was shown that P-delta effects did not significantly change the displacement at which limit strains were reached. While error in limit state prediction was slightly higher for columns with aspect ratio 10 and 12, it was smallest for aspect ratio 8; therefore, no obvious conclusion can be made on this trend. Based on the data, it seems limit states are best predicted for intermediate aspect ratios, and error increases for aspect ratios that are very low or very high. Very low aspect ratios likely have shear effects that are not being taken into account, while very high aspect ratios are controlled by P-delta effects that are not well accounted for in the appropriate analyses.

#### 6 CONCLUSIONS AND RECOMMENDATIONS

Column behavior and limit state prediction was evaluated by analyzing reinforced concrete columns with fiber-based nonlinear finite element elements with lumped plasticity and distributed plasticity formulations. Several trends and conclusions were made by comparing a large data set of previously tested columns to the predicted response from lumped plasticity elements with commonly used plastic hinge length, as well as comparing a smaller set of columns with varying aspect ratio to detailed numerical models. The following conclusions are therefore made in terms of the previously proposed hypotheses:

- I. Current plastic hinge length models do not offer the accuracy in predicting intermediate limit states required for the implementation of performance-based design. This was tested by analyzing 34 columns from the PEER Structural Performance Database with four common plastic hinge models. The most accurate expressions are those that include a component for moment gradient as well as strain penetration, such as those proposed by Priestley et al. (1996) and Berry et al. (2008). Of these two, the Berry model is recommended for limit state analysis. While the Priestley model is currently the most commonly used by researchers, it tends to overestimate limit states that occur at high displacement levels, such as bar buckling and failure. The Berry model was calibrated for this type of error and had better prediction for these limit states. However, it did not show enough accuracy, especially for concrete limit states, such as spalling and crushing and improvement is necessary before performance-based design can be utilized based on this model.
- II. Neither the lumped plasticity nor the distributed plasticity nonlinear beam-element formulations show significant evidence as a more appropriate analysis tool for prediction

of inelastic behavior. Both models contain advantages and disadvantages for modeling inelastic behavior. Lumped plasticity elements capture initial stiffness and yield behavior quite accurately; yet tend to overestimate the column capacity at large ductility levels. When using the plastic hinge model by Berry et al., the lumped plasticity model predicts limit state displacements with slightly more accuracy than a distributed plasticity finite element analysis. However, lumped plasticity modeling does not have the capability of capturing local behavior along the element length, which offers important insight into column behavior. Modeling with distributed plasticity elements predicted a softer initial global response for the studied columns, yet it more accurately predicted force capacity at large ductility levels. While the distributed plasticity element allows the extraction of intermediate local behavior, it does have limitations. Intermediate damage states are very difficult to predict and the model showed a random trend in predicting them for varying column aspect ratios. Limit state prediction was similar between the lumped plasticity and distributed plasticity element models; however, failure conditions using the distributed plasticity element were generally overestimated.

III. Slenderness in reinforced concrete columns greatly affects their global response and challenges the analysis methods for its prediction. Analyses with both lumped plasticity and distributed plasticity elements failed to reliably capture to the softening hysteretic response caused by P-delta effects in slender columns. Analyses with P-delta effects taken into account captured the softening trend of the response; however, the models still largely overestimates the column's force capacity. Evaluation of the spread of plasticity in slender columns showed that P-delta effects appear to increase the rate of growth of the plastic region at ductility levels close to yield, while the plastic region growth reduces

and seems to plateau at higher levels of ductility demand, which was not well captured by any of the evaluated numerical models. However, this trend did not have a large effect on limit state prediction. Error in overall limit state prediction ranged between 11% and 18%. The smallest of which was for intermediate aspect ratios (L/D=8) and the largest for high aspect ratios (L/D=12).

Based on these conclusions, the following recommendations for future research are made: First, a more unified definition of limit states is necessary before performance-based design can be implemented into common practice. This is especially true for limit states pertaining to concrete damage, which show large and random error across all numerical models. Higher accuracy in numerical methods is also recommended for the implementation of PBD. Error in limit state prediction by both lumped plasticity and distributed plasticity elements should be reduced while maintaining the efficiency of these formulations. Lastly, the behavior of slender columns should be analyzed carefully by evaluating their behavior due to P-delta effects. The destabilizing effects experienced is very slender columns is not well captured by current models and must be accounted for to ensure controlled seismic performance of bridge columns with high aspect ratios.

# **REFERENCES**

### **REFERENCES**

AASHTO. (2010). "AASHTO LRFD Bridge Design Specifications (5th Edition)." American Association of State Highway and Transportation Officials.

Abell, M. (2012). "Geometric nonlinearity." *Computers and Structures, Inc. Knowledge Base*, <a href="https://wiki.csiberkeley.com/display/kb/Geometric+nonlinearity">https://wiki.csiberkeley.com/display/kb/Geometric+nonlinearity</a> (June 18, 2012).

Bae, S., Bayrak, O. (2008). "Plastic Hinge Length of Reinforced Concrete Columns." *ACI Structural Journal*, 105(3), 290-300.

Berry, M., Lehman, D., Lowes, L. (2008). "Lumped-Plasticity Models for Performance Simulation of Bridge Columns." *ACI Structural Journal*, 105(3), 270-279.

Berry, M., Parrish, M., Eberhard, M. (2004). "PEER Structural Performance Database User's Manual." *PEER User's Manual*, 2004(01).

Caltech. (2011). "Significant Earthquakes and Faults." *Southern California Earthquake Data Center*, <a href="http://www.data.scec.org/significant/northridge1994.html">http://www.data.scec.org/significant/northridge1994.html</a> (June 17, 2012).

Caltrans. (2010). "Seismic Design Criteria." November 2010(1.6).

Chang, G., Mander, J. (1994). "Seismic Energy Based Fatigue Damage Analysis of Bridge Columns: Part I- Evaluation of Seismic Capacity." *NCEER Technical Report*, 94-0006.

Corley, G. (1966). "Rotational Capacity of Reinforced Concrete Beams." ASCE Journal of the Structural Division, 92(ST5), 121-146.

Ghobarah, A. (2001). "Performance-based design in earthquake engineering: state of development." *Engineering Structures*, 23(2001). 878-884.

Gomes, A., Appleton, J. (1997). "Nonlinear Cyclic Stress-Strain Relationship of Reinforcing Bars Including Buckling." *Engineering Structures*, 121(3). 433-445.

Hines, E. (2002). "Seismic Performance of Hollow Rectangular Reinforced Concrete Bridge Piers with Confined Concrete Elements." doctoral dissertation, Univ. of California San Diego, San Diego, CA.

Hines, E., Restrepo, J., Seible, F. (2004). "Force-Displacement Characterization of Well-Confined Bridge Piers." *ACI Structural Journal*, 101(4), 537-548.

Hose, Y., Seible, F., Priestley, M. (1997). "Strategic Relocation of Plastic Hinges in Bridge Columns." *Structural Systems Research Project*, (97/05).

Lee, C., Filippou, F. (2009). "Efficient Beam-Column Element with Variable Inelastic End Zones." *Journal of Structural Engineering*, 135(11). 1310-1319.

Lehman, D., Moehle, J. (2000). "Seismic Performance of Well-Confined Concrete Bridge Columns." *PEER Report*, 1998(01).

Lehman, D., Moehle, J., Mahin, S., Calderone, A., Henry, L. (2004). "Experimental Evaluation of the Seismic Performance of Reinforced Concrete Bridge Columns." *Journal of Structural Engineering*. 130(6). 869-879.

Neuenhofer, A., Filippou, F. (1997). "Evaluation of Nonlinear Frame Finite-Element Models." *Journal of Structural Engineering*, 123(7). 958-966.

OpenSees. (2011). "OpenSees User Documentation." <a href="http://opensees.berkeley.edu/wiki/index.php/OpenSees\_User>(May 2011).">http://opensees.berkeley.edu/wiki/index.php/OpenSees\_User>(May 2011).</a>

Park, R., Paulay, T. (1975). "Reinforced Concrete Structures." Wiley. New York, NY.

Paulay, T., Priestley, M. (1992). "Seismic Design of Reinforced Concrete and Masonry Buildings." John Wiley & Sons, Inc., New York, NY.

PEER. (2011). "PEER Structural Performance Database." <a href="http://nisee.berkeley.edu/spd/">http://nisee.berkeley.edu/spd/</a>>(May 2011).

Priestley, M., Calvi, G., Kowalsky, M. (2007). "Displacement-Based Seismic Design of Structures." IUSS Press. Pavia, Italy.

Priestley, M., Park, R. (1984). "Strength and Ductility of Bridge Substructures." *RRU Bulletin*, 71. Road Research Unit. National Roads Board, Wellington, New Zealand.

Priestley, M., Park, R. (1987). "Strength and Ductility of Concrete Bridge Columns Under Seismic Loading." *ACI Structural Journal*, 84(1). 61-76.

Priestley, M., Seible, F. (1991). "Seismic Assessment and Retrofit of Bridges." Structural Systems Research Project, 91/09. University of California, San Diego, California.

Priestley, M., Seible, F., Calvi, G. (1996). "Seismic Design and Retrofit of Bridges." John Wiley & Sons. New York, NY.

Schellenberg, A., Yang, T., Mahin, A., Stojadinovic, B. (2008). "Hybrid Simulation of Structural Collapse." *The 14<sup>th</sup> World Conference on Earthquake Engineering*, Beijing, China.

Scott, M., Fenves, G. (2006). "Plastic Hinge Integration Methods for Force-Based Beam-Column Elements." *Journal of Structural Engineering*, 132(2). 244-252.

Silva, P., Sangtarashha, and Burgueño, R. (2012). P-Delta Effects in Limit State Design of Slender RC Bridge Columns," *15th World Conference on Earthquake Engineering*, Lisbon, Portugal.

Spacone, E., El-Tawil, S. (2004), "Nonlinear Analysis of Steel-Concrete Composite Structures: State of the Art." *Journal of Structural Engineering*, 130(2). 159-168.

Zhao, J., Sritharan, S. (2007). "Modeling of Strain Penetration Effects in Fiber-Based Analysis of Reinforced Concrete Structures." *ACI Structural Journal*, 104(2). 133-141.